

Numerical Simulation of the Lightning Swept Stroke for the Zoning of Unconventional Aircraft

by

Nathanael A. Jenkins

Submitted to the Department of Aeronautics
in partial fulfillment of the requirements for the degree of

MASTER OF ENGINEERING IN AERONAUTICAL ENGINEERING

at

IMPERIAL COLLEGE LONDON

while studying abroad at the

MASSACHUSETTS INSTITUTE OF TECHNOLOGY

June 2024

© 2024 Nathanael A. Jenkins. All rights reserved.

Authored by: Nathanael A. Jenkins
Department of Aeronautics and Astronautics
May 10, 2024

Certified by: Carmen Guerra-Garcia
Draper Career Development Assistant Professor of Aeronautics and Astronautics
Thesis Supervisor

Accepted by: Maria Ribera Vincent
Senior Strategic Teaching Fellow
Imperial College London, Department of Aeronautics



IMPERIAL

Numerical Simulation of the Lightning Swept Stroke for the Zoning of Unconventional Aircraft

by

Nathanael A. Jenkins

Submitted to the Department of Aeronautics

on May 10, 2024 in partial fulfillment of the requirements for the degree of

MASTER OF ENGINEERING IN AERONAUTICAL ENGINEERING

ABSTRACT

Lightning is a powerful, yet poorly-understood, natural phenomenon which poses a significant hazard to the thousands of aircraft that fly each day. In the past, lightning strikes have caused several fatal aircraft accidents, so the design of lightning protection systems is critical to maintaining safety standards in the aviation industry.

As aircraft manufacturers work towards a sustainable future, they are increasingly exploring and adopting novel and unconventional aircraft designs. A lack of in-service experience makes it difficult to design appropriate lightning protection systems for new aircraft using current best practices. Understanding of the physical mechanisms behind aircraft lightning strikes is limited, although several flight and testing campaigns have worked to improve this.

The first aspect of protecting novel aircraft from lightning strikes is the definition of ‘zones’ which dictate the degree of protection in each region on the aircraft surface. This is known as lightning zoning. Existing, largely empirical, methods are not appropriate for unconventional aircraft, so physics-based models for lightning zoning have recently been investigated as an improved approach. This work builds on a physics-based model for lightning attachment and works towards a tool which can completely evaluate the lightning zoning requirements of new aircraft concepts.

A physics-based model for the second lightning zone is proposed, validated, and applied to several unconventional test cases. The second zone corresponds to the ‘lightning swept stroke’, or the reattachment of the lightning arc to new regions as it is swept along the aircraft surface by the aircraft motion. The effects of changing fluid models and simulation parameters are evaluated and an inviscid fluid model is found to be adequate for aircraft zoning. Validation is conducted by comparing results to data from the NASA Storm Hazards Program, a series of flight campaigns conducted in the 1980s, as well as zoning diagrams for existing, certified commercial aircraft. The tool is then applied to a ‘blended wing body’, and an aircraft with a ‘truss-braced wing’.

The model successfully generates zoning results in agreement with current best practices when applied to a conventional aircraft. It identifies zoning results for unconventional geometries which could not have been found using recommended practices. The proposed model could be combined with existing models for the first lightning zone to create a fully automated aircraft zoning tool for engineering or certification.

Thesis supervisor: Carmen Guerra-Garcia

Title: Draper Career Development Assistant Professor of Aeronautics and Astronautics

Acknowledgments

I owe a great deal of thanks to Carmen Guerra-Garcia for her excellent supervision, mentorship and support, and look forward to our continued work together over the coming years. Thanks also to Sam Austin, Jaime Peraire, Ngoc Cuong Nguyen, and Qiqi Wang for their expert advice, and Maria Ribera-Vincent for providing supervision from the UK.

This work was partially funded by The Boeing Company. I would like to thank the Boeing Research and Technology team for their advice and support, specifically Louisa Michael, Thomas Mitchum, and Ben Westin.

CFD codes used in this work were kindly provided by Emilio Baglietto (MIT), QiQi Wang (MIT/ FlexCompute), and Chris Cantwell (ICL). This project was significantly accelerated by access to high-performance computing facilities at the Imperial College London Department of Aeronautics and the MIT Supercloud and Lincoln Laboratory Supercomputing Center.

Contents

Title page	1
Abstract	3
Acknowledgments	5
List of Figures	11
List of Tables	13
1 Introduction	15
1.1 Lightning Phenomena	16
1.2 Aircraft-Lightning Interactions	17
1.2.1 Aircraft-Lightning Physics	17
1.2.2 Lightning Damage on Aircraft	18
1.3 Aircraft Lightning Zones	20
1.3.1 Zone Definitions	20
1.3.2 Current Zoning Methods	21
1.3.3 Physics-Based Methods	22
2 Physical Model	24
2.1 Arc Representation	24
2.1.1 Reattachment and Reconnection	25
2.1.2 Arc Parameters	27
2.2 Surface Effects	31
2.2.1 Materials and Coatings	31
2.2.2 Geometric Electric Field Enhancement	31
2.3 Fluid Models	31
2.3.1 Transient Effects	32
2.3.2 Viscous Effects	32
3 Numerical Implementation	34
3.1 Arc Model	35
3.1.1 Spatial Discretization	35
3.1.2 Reattachment and Reconnection	36
3.1.3 Electrical Current Waveform	38

3.2	Initialization	40
3.2.1	Attachment Point Generation	40
3.2.2	Field Direction Generation	41
3.3	Model Outputs	41
3.3.1	Attachment Probability	42
3.3.2	Additional Metrics	42
3.4	Computational Fluid Dynamics	44
3.4.1	Viscous Simulations	44
3.4.2	Inviscid Simulations	45
3.5	Verification of the Swept Stroke Model	46
3.5.1	Temporal Refinement	46
3.5.2	Spatial Refinement	47
3.5.3	Number of Arcs	48
4	Simulation of Aircraft Test Cases	50
4.1	Military Aircraft: Comparison to Results from the NASA Storm Hazards Program	50
4.1.1	The NASA Storm Hazards Program	50
4.1.2	Simulation of the F-106B Aircraft	50
4.1.3	Strike 8 from the 1981 Campaign	51
4.1.4	Strike 4 from the 1980 Campaign	54
4.1.5	Aggregate Strike Distribution	55
4.1.6	Sensitivity Analysis	56
4.2	Commercial Aircraft: Mapping Model Results to Lightning Zones	59
4.2.1	Simulation of a Commercial Aircraft	59
4.2.2	Zoning Mapping	60
4.3	Unconventional Aircraft: Comparison to State-of-the-Art Zoning Methods	63
4.3.1	Zoning of a ‘Blended-Wing-Body’	63
4.3.2	Zoning of a ‘Truss-Braced Wing’	66
5	Conclusions	68
5.1	Future Work	69
A	2D Gaussian Distribution	70
A.1	The Multivariate Gaussian Distribution	70
A.2	Mapping to an Arbitrary Surface	71
B	Normalization of Swept Stroke Surface Data	72
B.1	Probability Distribution	72
B.2	Time Integrals	73
C	Computational Fluid Dynamics Parameters	74
C.1	Viscous Simulations: Flow360	74
C.2	Inviscid Simulations: SU2	75
C.2.1	Mesh Generation: Gmsh	75

C.3	Inviscid Simulations: StarCCM+	76
C.3.1	Mesh Generation: StarCCM+	76
References		79

List of Figures

1.1	Global electric circuit (reproduced from Austin [40]).	16
1.2	Aircraft-triggered lightning growth.	18
1.3	Idealized swept stroke reattachment.	19
1.4	Examples of lightning damage on aircraft due to direct effects.	20
1.5	Lightning zones for a commercial aircraft [60].	21
2.1	Physical model of the lightning arc.	25
2.2	Reattachment and reconnection processes.	26
2.3	Criteria for triggering reattachment and reconnection.	26
2.4	The stretched arc and lengths for predicting the dominant reattachment mechanism.	27
2.5	Measurements of the electron number density across the core of an electrical arc in an argon-hydrogen mixture at different electrical currents [77], [78]. . .	29
2.6	Proposed models for the internal electric field of a lightning arc [37], [79], [80].	29
2.7	Lightning current waveforms.	30
3.1	Zoning simulation workflow.	34
3.2	Numerical model of the lightning arc.	35
3.3	Numerical issues caused by arc elongation and contraction.	36
3.4	Numerical implementation of reattachment and reconnection.	37
3.5	Flowchart of tasks during each arc time step.	38
3.6	Model current profile.	39
3.7	Random seed generation of 1200 arcs (D8 aircraft [101], [102]).	40
3.8	Attachment point propagation technique.	41
3.9	Field direction seed generation.	42
3.10	Cells touched by the lightning arc.	43
3.11	CFD residual plots for simulations of the F-106B aircraft.	44
3.12	CFD mesh configurations for the F-106B aircraft.	45
3.13	Results of the swept stroke model refinement study.	47
3.14	Results of arc count refinement study.	49
4.1	F-106B aircraft geometry.	51
4.2	Initialization of 1200 strikes on the F-106B aircraft.	51
4.3	Swept stroke simulations for strike 8 of the 1981 campaign using different fluid models.	53

4.4	Behavior of the simulated lightning arc near the engine inlet using different fluid models.	53
4.5	Strike 4 from the 1980 campaign over the F-106B tailplane.	54
4.6	Swept stroke distributions on the F-106B aircraft using different fluid models.	55
4.7	Inviscid swept stroke distribution on the F-106B aircraft, bottom view.	55
4.8	Radius parameter exploration; 2000 strikes on the F-106B aircraft.	57
4.9	Altitude and attitude parameter exploration; 2000 strikes on the F-106B aircraft.	58
4.10	Distribution of 2000 strikes at 5° yaw.	58
4.11	Distribution of 2000 strikes at high pitch angles.	59
4.12	Initial conditions of first 500 simulated lightning arcs on a commercial aircraft.	60
4.13	Commercial aircraft zoning simulation; 6000 lightning arcs, 0° pitch.	60
4.14	Commercial aircraft zoning results (fuselage only, excludes zone 1).	62
4.15	Computational mesh used for blended wing body CFD simulations.	63
4.16	Blended wing body zoning simulation; 6000 lightning arcs, 0° pitch.	64
4.17	Blended wing body simulated zoning result, considering only attachment at the nose.	65
4.18	Blended wing body zoning result using aerospace recommended practices [26], considering only attachment at the nose.	65
4.19	Truss-braced wing simulated zoning result, considering only attachment at the nose.	67
4.20	Truss-braced wing zoning result using aerospace recommended practices [26], considering only attachment at the nose.	67
A.1	Uniform bivariate Gaussian distribution and univariate distribution scaled by $\frac{1}{\sqrt{2\pi}}$	71
B.1	Sweeping of arcs past lines of equipotential.	73
B.2	Probability distribution normalization methods.	73
B.3	Normalization methods for time-integrated metrics.	73
C.1	Gmsh mesh generation domain and refinement region.	77

List of Tables

1.1	Aircraft lightning zones [26]	21
2.1	Arc model physical parameters at sea level	28
2.2	Birds-eye-view of mathematical models for resolving viscous effects	32
3.1	Idealized current waveform parameters	39
3.2	Stochastic current waveform parameters [25]	40
3.3	Simulation parameters: time step refinement	47
3.4	Simulation parameters: spatial refinement	48
3.5	Simulation parameters: Monte-Carlo sampling refinement	49
4.1	F-106B simulation parameters	52
4.2	Flight conditions for strike 8 from the 1981 campaign [41]	52
4.3	Sensitivity analysis for F-106B simulations	56
4.4	Commercial aircraft simulation parameters	59
4.5	Blended wing body simulation parameters	64
4.6	Truss-braced wing simulation parameters	66
C.1	Flow360 CFD parameters	75
C.2	SU2 CFD parameters	76
C.3	Gmsh mesh generation parameters	76
C.4	StarCCM+ CFD parameters	77
C.5	StarCCM+ mesh generation parameters (blended wing body)	78

Chapter 1

Introduction

Every day, an average of more than 77 commercial aircraft are struck by lightning¹, equivalent to about one strike per aircraft per year [1]. The energy dissipated during a lightning strike (up to 100 GJ [2], [4]) is equivalent to 2.4 tonnes of TNT² [5]. Yet, despite the immense power and high frequency of aircraft-lightning interactions, the aviation industry is safer than ever [6] and modern aircraft are well-protected from the dangers of lightning [7], [8].

Innovation is rife in the aviation industry as designers explore novel, fuel-efficient concepts in the commercial space and as a new class of ‘urban air mobility’ [9]–[13] vehicles begin to take flight. New concepts include ‘blended wing bodies’ [14]–[18], ‘truss-braced wings’ [19], [20], and fully-electric propulsion systems [21]–[24], all working to reduce the environmental (and financial) cost of air transport. These innovations are driving significant changes to aircraft geometries, propulsion systems, and materials.

Such radical changes to aircraft designs bring into question current methods for designing and certifying lightning protection systems [8]. Existing standards for protection systems rely on historical information and in-flight experience [25]–[27], which is nonexistent for these new designs. This shift away from conventional tube-and-wing configurations creates the need to re-assess the physical problem so that more effective, generalized tools for designing and certifying protection systems can be developed.

Physics-based models have been proposed as a solution to this challenge [8], [28]–[31]. A key stage in the design of a lightning protection system is the classification of ‘zones’, which define the level of protection required at different regions on the fuselage. Physics-based approaches to zoning rely on reduced-order models of gas discharge physics, first proposed by Gallimberti [32]. In the 1970s, Les Renardières conducted laboratory experiments on long arcs (to the order of meters) which contributed to the derivation of arc simulation methods [33]–[35]. In the 1990s, ONERA and the University of Padua brought together physical models for the small-scale discharge physics and the large-scale aircraft geometry to develop numerical methods for zoning [30], [31], [36], [37]. These are now being revisited due to the recent upsurge in innovative aircraft designs [38], [39].

¹Fisher et al. [1] and Rakov and Uman [2] find that the average commercial aircraft is struck by lightning about once per year. Prentice et al. [3] estimate that there are 28,400 active commercial aircraft in the global fleet. Therefore, an average of $28400/365 = 77$ commercial aircraft are struck by lightning each day.

²Karlos et al. [5] state that the heat of detonation of TNT is at least 4.1 MJ/kg . $10^{10}/4.1 \times 10^6 = 2439 \text{ kg}$ of TNT.

In 2020, Austin [40] developed a model for the ‘first attachment point’ of lightning strikes on aircraft, which can be used to identify the first of three lightning zones. After the initial attachment (corresponding to zone 1), the arc is ‘swept’ along the fuselage while the aircraft moves forwards. Over the duration of a lightning strike, the arc can be swept the entire length of the aircraft. The swept stroke region, which is reflected in the second lightning zone, is addressed in this thesis.

A physics-based model is proposed which builds on the work conducted by ONERA and the University of Padua [36], [37]. The model is validated using real lightning strike data from the NASA Storm Hazards Program [41], [42], as well as existing zoning data for a commercial aircraft. Applications of the model to unconventional ‘blended wing body’ and ‘truss-braced wing’ aircraft demonstrate the value of the tool and provide insights into how lightning protection systems may need to adapt for the next generation of aircraft.

1.1 Lightning Phenomena

A ‘classical’ approach to atmospheric electricity helps with understanding the fundamentals of lightning. Broadly, the ‘global electric circuit’ can be modeled as shown in figure 1.1. The earth is negatively charged relative to the electrosphere, discharging through fair-weather currents of about 1.8kA [43]. The ‘generators’ which keep this circuit charged are the thousands of thunderstorms which take place every day [44]. Thunderstorms can occur above the cruise altitude of commercial aircraft, so can impact any stage of flight [2], [45].

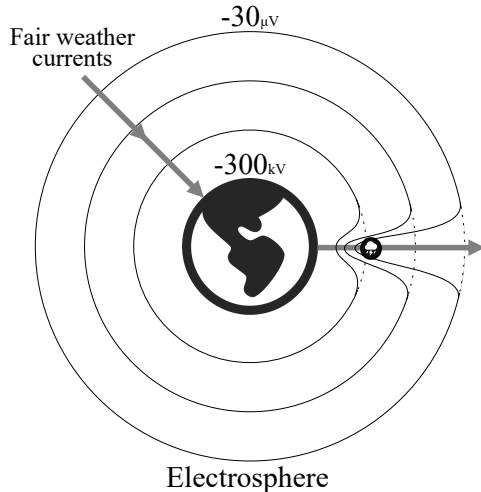


Figure 1.1: Global electric circuit (reproduced from Austin [40]).

The exact process by which clouds are electrified remains an ‘unsolved problem in atmospheric physics’ [46]. Regardless of the charging mechanism, clouds require a sufficiently high charge before they can generate lightning. There are four broad processes by which a lightning strike may occur; positive or negative growth downward from the cloud, and positive or negative growth upward from the ground [2]. ‘Intra-cloud’ lightning flashes also occur and make up more than 50% of lightning events, although exchange less charge (and therefore expend less energy) than cloud-to-ground strikes [25], [47].

One lightning flash is actually a complex series of discharges, largely grouped into streamers, leaders, and return strokes [2]. The return stroke is the component most commonly associated with lightning, during which the discharge current peaks at a value so high it causes a bright flash and sudden heating of the air (generating the pressure waves which create the sound of thunder). The return stroke phase is active while the arc is swept along an aircraft surface, so return stroke physics will be most closely examined in this project. Leaders and streamers are pivotal in the formation of the lightning arc, but occur over much smaller timescales and don't damage aircraft. Their effects are considered in detail by Austin [40] and are relevant for the modeling of zone 1.

1.2 Aircraft-Lightning Interactions

It is well documented that, on average, a commercial aircraft is struck by lightning about once per year [1], [2] Around 90% of these events are ‘aircraft triggered’ [30], [48], meaning the lightning flash would not have occurred if the aircraft was not present. These events provide the foundation for the analysis in this project. The remaining 10% of aircraft lightning strikes involve interactions with naturally occurring lightning flashes and are referred to as ‘intercepted’ strikes. While aircraft-triggered lightning will be the focus of this thesis, a review of the lightning interception mechanism can be found in Rakov and Uman [2]. Aircraft-triggered strikes form the ‘*basis of [lightning] protection design*’ [25] although the lightning swept stroke (corresponding to zone 2) is agnostic to the inception mechanism.

1.2.1 Aircraft-Lightning Physics

The process by which aircraft trigger lightning strikes has been determined experimentally by Mazur [49] and is summarized by the following key stages, illustrated in figure 1.2;

1. The aircraft experiences a change in charge distribution in the presence of an atmospheric electric field.
2. A positive leader propagates from some positively charged point on the aircraft, in the direction of the ambient field.
3. As the leader propagates, the charge on the aircraft becomes increasingly negative.
4. A few milliseconds after the initiation of the positive leader, a negative leader forms from some other point on the aircraft.
5. The positive leader grows along with the negative leader (which propagates in a stepped fashion). Both leaders accelerate and begin ‘branching’.
6. In less than 1 ms the leaders will connect to cloud(s) and/ or the ground, at which point a return stroke occurs. This generates a powerful current pulse.

This sequence of events describes the majority of aircraft triggered lightning events although it has been shown that, under certain conditions, the first leader can be negative rather than positive [50].

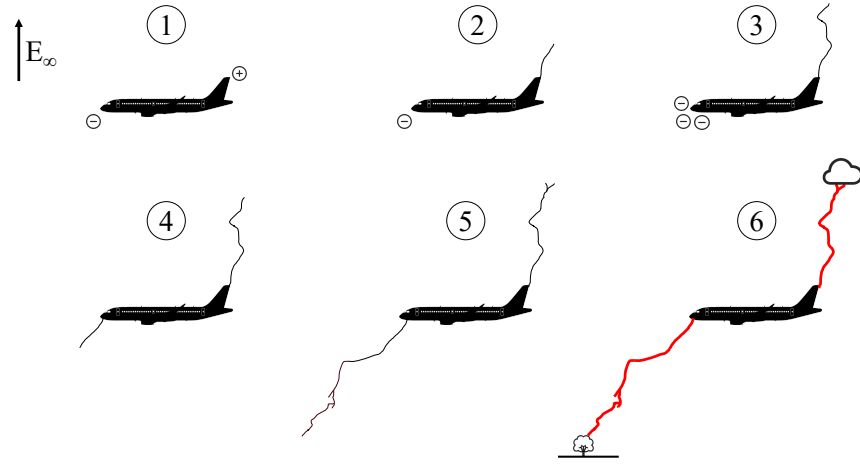


Figure 1.2: Aircraft-triggered lightning growth.

Once a lightning return stroke occurs, the lightning arc (a channel of ionized air, broken down by high voltages) does not immediately disappear. Instead, it is swept along the surface of the aircraft while more current flows through the arc, occasionally ‘pulsing’ at very high currents, to the order of 15 kA [2]. The first return stroke is usually the most powerful, but experimental results suggest that subsequent strokes (current pulses during the swept stroke) can experience higher currents than the first return stroke in around 33% of lightning flashes [51], [52]. The swept stroke phase can last hundreds of milliseconds [37]. In that time, the lightning arc can be swept along the entire length of most aircraft³.

The lightning arc will experience stretching and distortion as it moves with the flow field. Depending on a number of factors, the arc may be fixed in place on the surface or it may be swept smoothly [37]. As it is swept, the region near the surface will contort and this can cause the arc to jump, or ‘reattach’, to new points on the aircraft surface, as illustrated in figure 1.3 at time t_3 . When the arc jumps to a new position, the old section between the reattachment point and the surface (the dotted line in figure 1.3) no longer conducts current and quickly fades away. Reattachment is driven by the coupling between the flow around the aircraft, the magnetohydrodynamics of the arc, and the aircraft material(s) [55]. The importance of small-scale, often transient, effects make reattachment an extremely difficult physical problem to solve, especially at the scale of an entire aircraft.

1.2.2 Lightning Damage on Aircraft

Lightning has the potential to cause serious damage to air vehicles and has caused several historic accidents. Some of the most pivotal changes in lightning protection standards have been precipitated by fatal incidents, including Pan-Am Flight 214 [56], Imperial Iranian Air Force Flight 48 [57], and Nürnberg Flugdienst Flight 108 [58]. Broadly, lightning damage on aircraft can be categorized into ‘direct’ and ‘indirect’ effects: direct effects describe

³For example, a Boeing 787-8 is 57 m long [53] and flies at a cruise speed of 291 m/s [54]. A lightning arc swept at this speed will move the entire length of the fuselage in 0.196 seconds, which is a shorter duration than most lightning strikes [2].

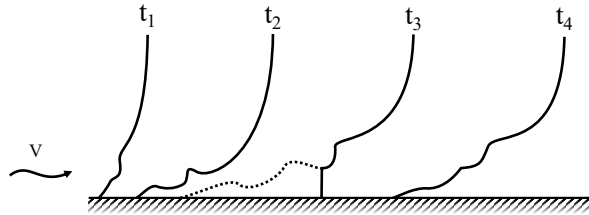


Figure 1.3: Idealized swept stroke reattachment.

physical damage to the aircraft structure or its components, while indirect effects relate to the electromagnetic disruption to electrical systems onboard the aircraft. Both direct and indirect effects have caused fatal incidents in the past [56], [58] and both are important considerations when designing a lightning protection system [27].

The current standards for designing and certifying lightning protection systems are described in a series of ‘Aerospace Recommended Practice’ (ARP) documents [25]–[27]. These documents dictate how both direct and indirect lightning effects can be evaluated and mitigated through robust design.

Direct Effects

ARP 5416 [27] lists four major examples of direct effects;

1. **Dielectric puncture.** Lightning can create holes in an aircraft skin where a dielectric (non-conducting) material covers a conducting one.
2. **Thermal damage and heating effects.** By several mechanisms, lightning can quickly increase the temperature at spots on the aircraft surface, leading to the burning of holes, explosive vaporization, or sparking. This can ignite fuel or other materials, and affects carbon fibre structures more severely than metal ones. Thermal damage is believed to be the cause of both examples shown in figure 1.4
3. **Acoustic shock wave damage.** The shock wave generated by sudden heating of the air in a lightning strike can dent metal skins and crack or rupture composite structures.
4. **Magnetic force.** The forces induced by current flowing through the arc and various aircraft components can be sufficiently strong to cause mechanical failure.

Many design measures are implemented to protect aircraft from these effects [59], which are evaluated using a myriad of tests outlined in ARP 5416 [27]. The extent to which different components need protecting is dictated by the zoning methodology discussed in section 1.3.

Indirect Effects

Through four different mechanisms [27], lightning can induce voltages and currents in the electrical wiring of aircraft which can damage or destroy aircraft electronics. While most of these effects are caused by strong electromagnetic fields, lightning can also attach to



(a) Swept stroke damage [60].

(b) Damage to an aircraft winglet [61].

Figure 1.4: Examples of lightning damage on aircraft due to direct effects.

exposed conductors on the aircraft exterior (antennas, lights, or heaters) which can conduct significant currents inside the aircraft and through sensitive electronics. Indirect effects are particularly important to ‘fly-by-wire’ aircraft and future uncrewed vehicles [12] for which electrical systems drive the flight controls without any mechanical backup [62]. As with direct effects, the required level of protection from indirect effects is influenced by the lightning zones [27].

1.3 Aircraft Lightning Zones

Lightning protection measures are tested to varying extents based on three lightning ‘zones’. The need for zoning is driven by the fact that some regions of the aircraft will be more prone to experiencing lightning attachment or sweeping than others. Zoning allows engineers to create appropriate protection systems without over-protecting low-risk regions. It is also critical in defining appropriate tests to demonstrate the efficacy of lightning protection systems during certification. The current standard for lightning zoning is defined in ARP 5414 [26].

1.3.1 Zone Definitions

The three lightning zones are summarized in ARP 5414 as;

- **Zone 1:** Regions likely to experience initial lightning attachment and first return strokes.
- **Zone 2:** Regions unlikely to experience first return strokes, but likely to experience subsequent return strokes (swept stroke regions).
- **Zone 3:** Regions unlikely to experience lightning attachment, but which may have to conduct lightning current between attachment points.

Zones are split into several sub-zones with more specific definitions depending on the probability of an extended ‘hang-on’. These are described in table 1.1 and illustrated for a commercial aircraft in figure 1.5.

Table 1.1: Aircraft lightning zones [26]

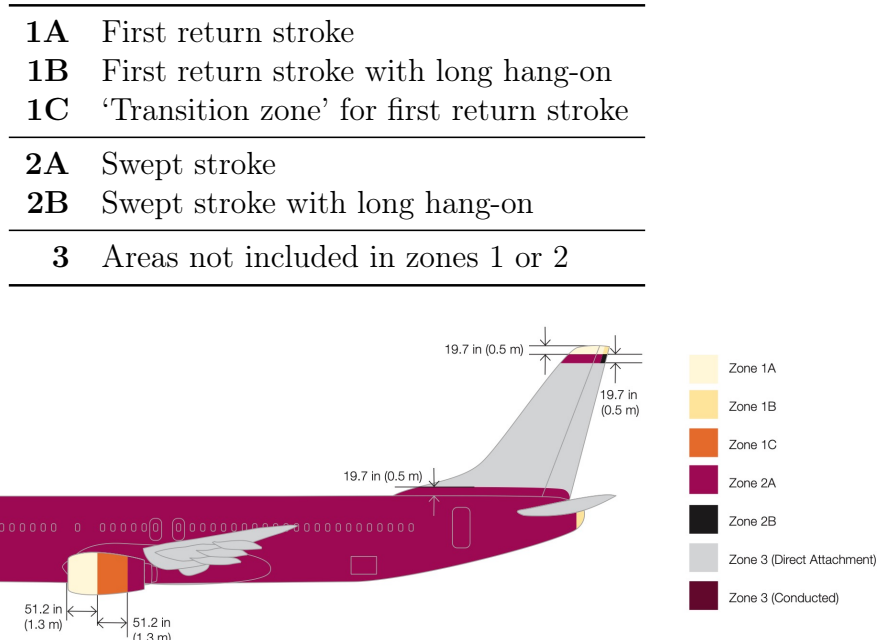


Figure 1.5: Lightning zones for a commercial aircraft [60].

1.3.2 Current Zoning Methods

The methods used to determine the locations of each lightning zone for a conventional aircraft are prescribed in ARP 5414 [26]. It is these methods which, although valuable for conventional 'tube and wing' aircraft, may not perform as desired for unconventional aircraft [8]. Most transport aircraft employ a 'zoning by similarity' approach, leveraging past data from similar aircraft to certify a new design.

The first stage in zoning is identification of initial attachment points. ARP 5414 approves three methods (usually, several of these are combined to generate a robust result) for determining these; service experience, testing, and analysis. Service experience relies on data from existing similar aircraft so cannot be used for novel designs. Experimental test requirements are prescribed in ARP 5416 [27], though ARP 5414 recognizes that such experiments can be limited in relevance. Experiments may also be expensive and are impractical during early stages of the design process. The industry standard for identifying attachment points by 'analysis' is the rolling sphere method, in which a sphere of a certain radius is rolled over the aircraft surface and any points touched by the sphere are treated as being at risk of lightning attachment. Physics-based models have been proposed as a superior approach to testing and rolling-sphere analysis [31], [63] and are discussed in section 1.3.3.

The first lightning zone is identified based on proximity to the initial attachment point(s). Zone 1B describes any initial attachment points at trailing edge surfaces where the swept stroke remains attached to its starting point. Zones 1A and 1C are prescribed using a simple empirical formula which considers an aircraft's altitude, air speed, and lightning leader velocity [26]. Using typical aircraft parameters, this formula yields an extension from

the initial attachment point of 1.3m for zone 1A and 2.6m for zone 1C. This is a conservative estimate which does not account for the direction of the flowfield local to the attachment point or any geometric peculiarities of the aircraft.

Zone 2A, which encompasses the swept stroke region, is required to include all surfaces aft of zone 1C, with trailing edge surfaces in this region being classified as zone 2B due to the expectation of long hang-on. Zones 1 and 2 are further extended laterally by 0.5m at various prescribed points on the airframe to account for small lateral movements of the lightning arc. Once zones 1 and 2 are defined, zone 3 is easy to identify.

Ultimately, existing approaches do provide safe and conservative methods for zoning conventional aircraft. However, these methods are rooted in experiential observations and ‘similarity’ arguments which may not apply to novel aircraft. Further, Lalande [31] states that even conventional aircraft have been known to experience relatively severe lightning strikes in regions identified as zone 3, which may have been described differently if a physics-based zoning approach were employed instead.

1.3.3 Physics-Based Methods

Lightning encompasses an enormous spectrum of length and time scales. Streamer inception occurs over millimeters and nanoseconds, leader propagation takes place over meters and milliseconds, and the arc phase is kilometers long and can last almost one second [2], [45]. Resolving all of these scales in a single simulation is practically infeasible, so each phase is approached separately and under different assumptions. The initial attachment point is usually modeled separate to the swept stroke, since the two phases are driven by different physical mechanisms.

Models for the initial attachment point proposed by Lalande and Delannoy [31], were recently revisited by Austin [40] to create a tool capable of identifying the initial attachment points for an arbitrary aircraft geometry. This provides a valuable starting point for a swept-stroke model.

Engineering models for the swept stroke were investigated by ONERA and the University of Padua in the 1990s [30], [31], [36], [37]. The team simplified the lightning arc as a filament in 3D space, which was linearly advected in a flowfield obtained using computational fluid dynamics. The resulting model provides a foundation for the work in this thesis.

Recently, Guerra-Garcia et al. [39] tested a variation of the ONERA model using a high-fidelity simulation of a turbulent boundary layer. By analysing the arc model at these smaller scales, instantaneous turbulent velocity fluctuations were found to drive arc reattachment. These fluctuations are essentially impossible to model efficiently at the scale of an entire aircraft [64], creating a challenge for physics-based swept stroke models. While the importance of small-scale turbulence is recognized, engineering models for the swept stroke remain poorly developed, and yet are vital to protecting future aircraft from lightning.

Verification and Validation

Verification and Validation (V&V) are crucial to gaining confidence in a computational model [65], which is especially important if this model is to be used for certification. The AIAA defines verification and validation as [66];

Verification: The process of determining that a model implementation accurately represents the developer's conceptual description of the model and the solution to the model.

Validation: The process of determining the degree to which a model is an accurate representation of the real world from the perspective of the intended uses of the model.

Validation is conducted by in-depth analysis of the physical model in chapter 2 and by comparing simulation results to real-world data in chapter 4. Verification is evidenced by thorough analysis of the numerical model in chapter 3 and the model refinement study in section 3.5.

Chapter 2

Physical Model

A model of the lightning swept stroke must consider three domains, each made from a different state of matter: the lightning core is a plasma, the aircraft surface is solid, and the air around it is a gas. These are each addressed in the following three sections, using approaches which build on the model presented by Larsson et al. [37].

Clear model goals were outlined to direct assumptions and modeling decisions. The purpose of this model is not to perfectly resolve every physical mechanism at play. Rather, it is to provide insights to designers and regulators about the zoning of an aircraft. The goal of the model can be summarised as: **a physics-based, engineering model for the zoning of unconventional aircraft**. This allows for three key considerations while designing the model:

- †1 **Physics-based**: wherever possible, physics should be modeled using analytical relationships and analytically or experimentally derived parameters. Empirical relations should be avoided.
- †2 **Engineering model**: non-dominant physical mechanisms may be neglected to reduce computational complexity, provided it can be demonstrated that they have a negligible impact on results.
- †3 **Aircraft zoning**: the accuracy of the zoning result takes priority over the accuracy of any individual strike.

Since lightning is a highly stochastic phenomenon, a simulation approach based on Monte Carlo methods [67] is most appropriate, especially considering goal †3. This involves sampling many swept stroke simulations, each with slightly different parameters, and aggregating their behavior to understand the distribution of the swept stroke region. While this can be computationally expensive, Monte Carlo methods are also highly parallelizable, meaning they can be made significantly faster by conducting many simulations at once [68].

2.1 Arc Representation

While magnetohydrodynamic methods can simulate the small-scale dynamics of the three-dimensional arc [55], such simulations are too complex and costly to apply to an entire

aircraft. Instead, the arc is modeled as a three-dimensional filament of a finite radius, as illustrated in figure 2.1.

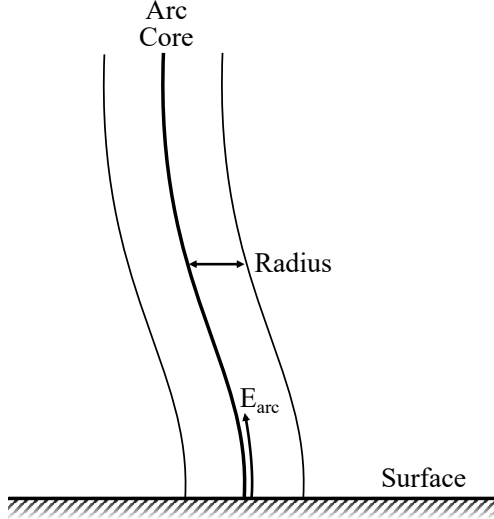


Figure 2.1: Physical model of the lightning arc.

Uman [69] demonstrated that the lightning arc can be assumed to be in local thermal equilibrium after the first return stroke. Larsson et al. [37] explain how this means that the arc can be treated like a Newtonian fluid with additional electromagnetic effects. Practically, this is modeled by perfect advection of the arc in the flow around the aircraft, with adjustments where electromagnetic effects would dominate (reattachment, for example). The arc also conducts an electrical current, discussed in section 2.1.2.

2.1.1 Reattachment and Reconnection

While this model treats the lightning arc as an axisymmetric tube, the real arc is a much less uniform shape, evidenced by Tholin et al. and Bourlet et al. [55], [70]. A combination of electromagnetic effects [70] and aerodynamic turbulence [39] cause the arc to become tortuous and move parts of the arc close to the aircraft surface. When a section of the arc comes sufficiently close to the surface, it can attach to the surface and begin conducting a current. The previous (longer) section of the arc experiences a reduction in current flow and fades away. This is called reattachment and is illustrated in figure 2.2a. Reconnection is a similar mechanism where a loop is formed in the arc. Instead of attaching to the surface, two parts of the arc connect to one another and the original loop between them fades away. This is illustrated in figure 2.2b.

Reconnection and reattachment are complex phenomena driven by the magnetohydrodynamics of the arc [55]. The conditions which trigger these processes can be simplified for an engineering model (goal †2) into two criteria:

1. Larsson et al. [36] propose that reattachment or reconnection occur when the breakdown electric field of air is exceeded, assuming all electric fields are uniform. Treating

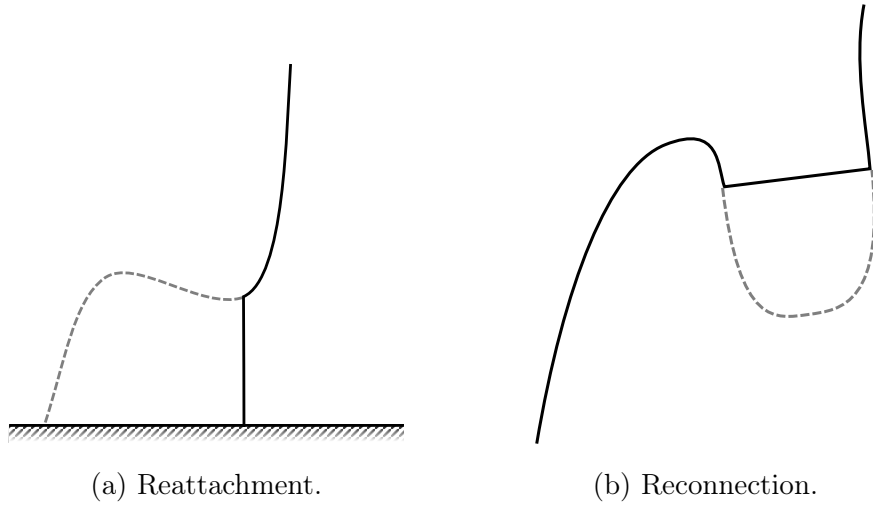


Figure 2.2: Reattachment and reconnection processes.

the internal electric field of the arc as a fixed value, E_{arc} , the potential at each arc point can be calculated by integrating along the length of the arc. Dividing the potential difference by the distance between two points gives an estimate for the electric field between them. If the electric field anywhere exceeds the breakdown field strength of air, discussed in section 2.1.2, then reattachment or reconnection is triggered. This is illustrated in figure 2.3a.

- Reattachment and reconnection are also triggered when the arc core is less than one arc radius from the surface, or another section of the core, as illustrated in figure 2.3b. This treats the arc as a three-dimensional rod, rather than an infinitely thin filament, and assumes that the arc attaches to any conducting object it comes into contact with. This criteria introduces a vertical arc segment at the root, which is continuously swept at a non-zero velocity.

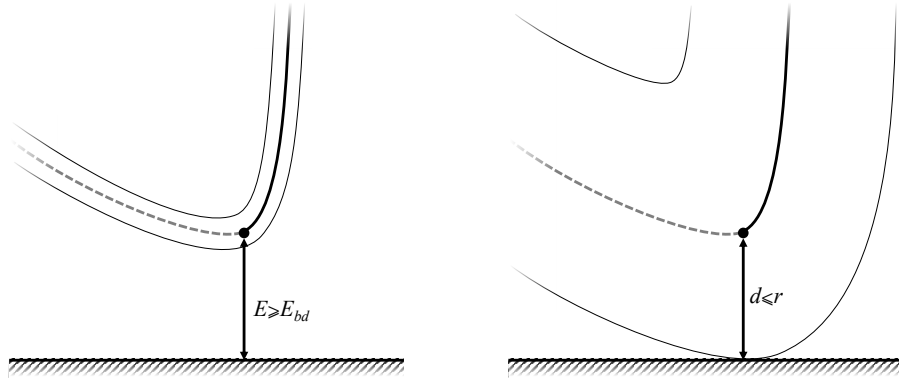


Figure 2.3: Criteria for triggering reattachment and reconnection.

Of these two criteria, the second, radius-based mechanism will dominate in this model. Section 2.1.2 explains how the arc's internal electric field E_{arc} , the breakdown field strength of air E_{bd} , and arc radius r are modeled as 1 kV/m, 3000 kV/m, and 5 mm respectively at sea-level. At a point s along the arc, the potential difference relative to the surface is $s \cdot E_{arc}$. If the shortest distance between point s and the aircraft surface is d , the electric field in the gap is approximately $s \cdot E_{arc}/d$. For this value to exceed the breakdown field strength and trigger reattachment, the condition in equation 2.1 must be met. This shows how the arc must be more than 3000 times longer than the distance to the surface for reattachment to be triggered by electrical breakdown. The distance to the surface must be greater than the radius, $d > r$, so that attachment isn't first triggered by the radius-based criteria. This means that, at a minimum, the arc must extend more than $3000 \times 0.005 = 15$ m in length (without passing within one radius of the surface) before reattachment by electrical breakdown can occur.

$$s = \left(\frac{E_{bd}}{E_{arc}} \right) \cdot d = \left(\frac{3 \times 10^3}{1} \right) \cdot d = 3000d \quad (2.1)$$

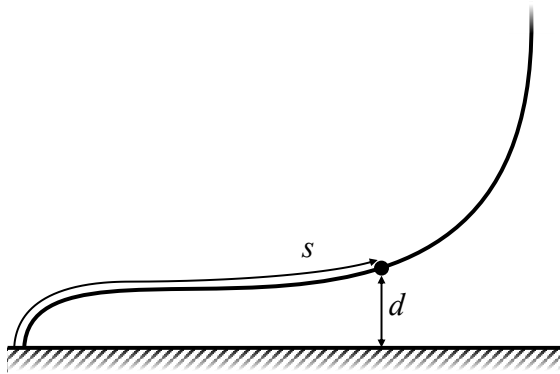


Figure 2.4: The stretched arc and lengths for predicting the dominant reattachment mechanism.

This finding agrees with the work of Guerra-Garcia et al. [39], which found that reconnection is extremely rare since the potential difference created over a loop in the arc is relatively small. Guerra-Garcia et al. also demonstrated that reattachment is heavily dependent on instantaneous velocity fluctuations which lengthen the arc and drive it closer to the surface. These cannot be efficiently resolved in an engineering model so were neglected on the basis of goal †2.

2.1.2 Arc Parameters

Bublievskii and Larsson et al. [37], [71] present formulae for the local radius and internal electric field of a lightning arc based on the assumption that all of the channel energy is dissipated by convective cooling due to airflow past the arc. This is incompatible with the advected arc model, which will experience no crossflow since the arc moves at the same speed as the air. The poor performance of the model can be seen in figure 2.6. The proposed

formulae break down at zero velocity, so more robust constant values are used for the arc radius and internal electric field. The parameters used in this model are outlined in table 2.1.

Table 2.1: Arc model physical parameters at sea level

Arc radius	r_0	5 mm
Internal electric field of arc	$E_{0_{arc}}$	1 kV/m
Breakdown electric field strength of air	$E_{0_{bd}}$	3000 kV/m

Scale factors are applied to the arc radius and internal electric field to account for the effects of reduced density at high altitudes. These are estimated based on the air number density ratio relative to sea-level, calculated using the 1976 International Standard Atmosphere [72]. Equations 2.2 and 2.3 show how the factors are applied. The results of these equations agree perfectly with the scaled values given by Rakov and Uman [73].

$$E_{arc} = \left(\frac{n}{n_0} \right) E_{0_{arc}} \quad (2.2)$$

$$r = \left(\frac{n_0}{n} \right) r_0 \quad (2.3)$$

Radius

The real lightning arc does not have a single, well-defined radius. Several efforts have been made to estimate values for the radius of a lightning arc, using predominantly optical methods. While these optical methods measure the luminous radius of the arc, a more appropriate metric for this model would be the conducting radius of the plasma core, through which the majority of the arc current is conducted.

An et al. [74] used optical methods to identify arc radii between 6.6-10.1 mm. Jones [75] estimated the radius based on the surface damage, which created ‘major discharge craters’ 1-3 mm in diameter. Jones also used analytical methods to estimate an arc diameter of 1.51 mm. Rakov and Uman [76] list many more attempts to characterize the arc radius, with results ranging from 3-30 mm. Granovskiy [77] plotted the electron number density distribution across an arc at sea-level pressure, as illustrated in figure 2.5. For large currents to the order of 100 A (section 2.1.2 shows how lightning current rarely falls below 400 A), it is clear that the plasma core radius is close to 5-6 mm when the arc is under equilibrium, so the sea-level radius $r_0 = 5$ mm was used for this model. Section 4.1.6 evaluates the sensitivity of the model to this parameter.

Although the model for arc radius proposed by Bublievskii and Larsson et al. [37], [71] performs poorly, there is a relationship between arc current and arc radius [78]. This means that the high-current pulses described in section 2.1.2 could alter the lightning radius and potentially trigger premature reattachment of the arc, a phenomenon which is ignored in the proposed model in favor of a simple, constant arc radius. While this simplification could impact the accuracy of an individual arc simulation, it is unlikely to drastically change the distribution of many thousands of strikes (goal †3) since current pulses make up such a small duration of the overall strike, as explained in section 2.1.2.

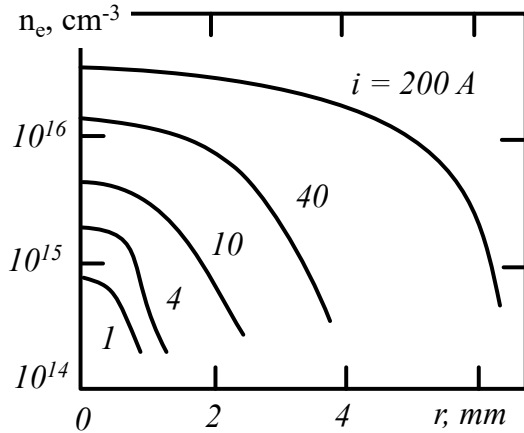


Figure 2.5: Measurements of the electron number density across the core of an electrical arc in an argon-hydrogen mixture at different electrical currents [77], [78].

Internal Electric Field

Figure 2.6 illustrates how the Bublievskii and Larsson et al. [37], [71] model for the internal electric field of the arc performs against a selection of data points from experimental work conducted by King [79]. It is clear that the model does not correlate to experimental results and is too dependent on the velocity and current. King's finding that the arc tends to experience a constant internal electric field of 10 V/cm (1000 V/m) for currents above 100A is taken to be a more verifiable estimate. This assumption holds since the swept stroke operates in a regime with a current above 100A as explained in section 2.1.2. King's estimate is further backed up by the findings of Dobbing and Hanson [80] and von Engel [81].

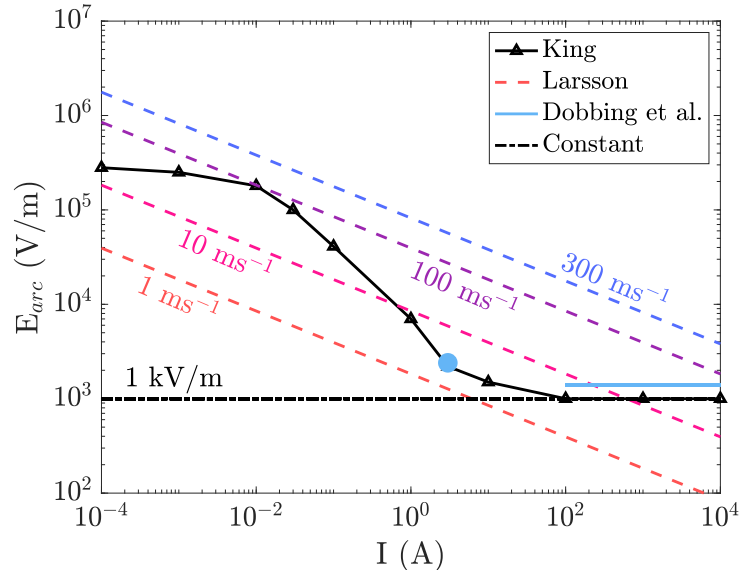


Figure 2.6: Proposed models for the internal electric field of a lightning arc [37], [79], [80].

Arc Current

A lightning arc will experience a highly random current waveform over the course of its lifetime of a few hundred milliseconds. An experimental measurement of the waveform is given in figure 2.7a. The complex current profile is simplified into a more simple profile in ARP5412 [25], illustrated in figure 2.7b. The profile outlined in the aerospace recommended practice is used to replicate a lightning strike in a repeatable manner and is sufficiently robust to use in this model. The current distribution has no impact on the zoning result (see section 4.2.2) and only provides supplementary engineering insights, so goal †3 dictates that it is not of critical importance.

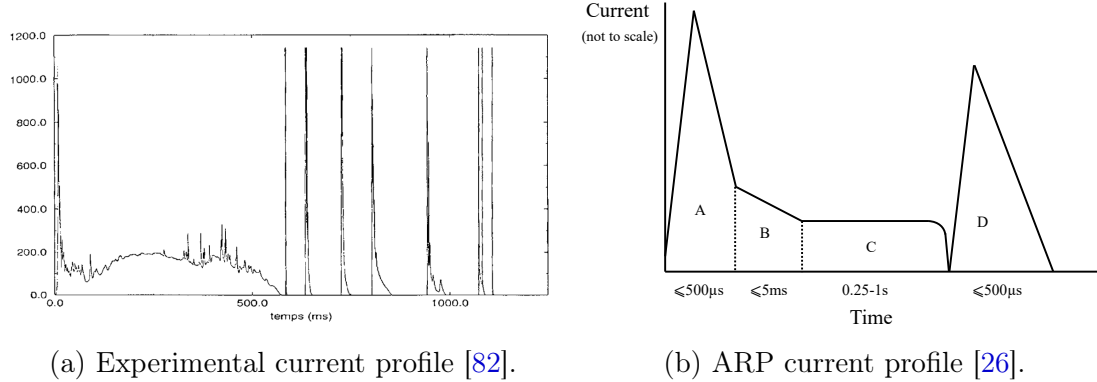


Figure 2.7: Lightning current waveforms.

While the simplified ARP current profile includes fixed values for the amplitude and duration of different current phases, the standard also lists experimental data which describes the random variations in the current parameters [2], [83]–[91]. Experimental results were used to inform the selection of random distributions for certain current parameters outlined in section 3.1.3. These also helped identify the worst-case current values, which are slightly larger than those used in the ARP waveform.

Breakdown Field Strength for a Large Air Gap

The breakdown field strength of air is widely accepted to be 30 kV/cm at sea-level [76], [78]. This is scaled at altitude by the factor given in equation 2.2. The presence of hydrometeors (water or ice particles in the atmosphere) can further reduce the breakdown field strength [76], but this is neglected in the proposed model to reduce complexity and because the breakdown field strength has been demonstrated to be of less importance than other parameters (goal †2).

The assumption that the breakdown field strength of air is constant is valid for large air gaps in uniform electric fields, but begins to fail over shorter distances [78]. As two electrodes (or the arc and the aircraft surface) move towards each other, changes in the small-scale physics which drive the breakdown mechanism mean that the breakdown field strength increases slightly. Again, this is ignored in the proposed model based on goal †2.

When an aircraft is struck by lightning, a negative leader will grow from one attachment point and a positive leader from another [2]. The breakdown field strength differs slightly

between positive and negative arcs [78], [92], but this is ignored in the proposed model based on goal †2. Since the locations at which a certain polarity will attach cannot be definitively determined [40], both polarities are considered equally likely when evaluating the swept stroke.

2.2 Surface Effects

2.2.1 Materials and Coatings

The aircraft material and surface coatings can have a significant impact on how the swept stroke behaves, as proven experimentally by Brick and Schneider [92]. Aircraft paint, which is usually dielectric [55], is often punctured during the first return stroke. This exposes the much more conductive sheet metal beneath, which the arc may have some tendency to adhere to. Modeling the breakdown of the paint layer and the intricate interactions of the arc with the surface is outside of the scope of an engineering model (goal †2), although MagnetoHydroDynamic (MHD) simulation tools can be used to explore such behaviour [55].

2.2.2 Geometric Electric Field Enhancement

Bouwers and Cath [93] demonstrate how different geometries can enhance the electric field between two objects experiencing a potential difference. In this arc model, reattachment and reconnection criteria are based on the assumption of a uniform electric field which behaves like the field between two infinitely large flat plates. The real arc will actually experience a slightly stronger electric field because of the geometry of the arc and the aircraft surface. Determining the actual electric field around the lightning arc would involve solving the Laplace equation, which is too complex for an engineering model. Instead, it is assumed that field enhancement has a relatively small impact on results, especially since reattachment and reconnection are dominated by the radius-based criteria.

This assumption is validated by the work of Brick and Schneider [92], who found that the small protrusions at rivets and bonded joints have little impact on the swept stroke. A protruding fin similarly experienced "no unusually long dwell times", though some increase in arc dwell time was noted at the edge of a large hole in the surface. Brick and Schneider conclude that '*swept strokes will reattach to metal surfaces that are closest to the path of the advancing discharge arc rather than to sharp edges further away.*'

2.3 Fluid Models

A key component of the proposed model is the ability to accurately predict the velocity flowfield around the aircraft. The Navier-Stokes equations accurately describe the flow of fluids, but are extremely costly to solve in all but the most simple of cases. To solve the fluid equations around more complex geometries, simplified mathematical models must be used.

For the particular case of flow over an aircraft, simplifying the fluid model can be challenging because of the high Mach number and high Reynolds number of the flow. Most commercial aircraft fly close to transonic Mach numbers, where the effects of compressibility

cannot be neglected, so an incompressible fluid model is not valid. The high Reynolds number means that the computational cost of solving the fluid equations is particularly high for aircraft [94].

While these challenges make it difficult to accurately predict the flowfield around an aircraft, some simplifications can still be applied without significantly impacting the swept stroke model. Section 4.1 will explore how relatively extreme simplifications to the physical model of the flow can still produce a useful zoning result, in line with goal †3. Aside from compressibility, two key mechanisms can be simplified in fluid models: (1) transience describes the time-dependence of a fluid simulation, and (2) viscosity is responsible for generating turbulence.

2.3.1 Transient Effects

Turbulent flows, like those experienced around an aircraft, are unsteady, meaning that the properties of the flow at any point in space will change with time. This unsteadiness is driven by a fluctuating component of the velocity field, which can be ignored by time-averaging so that only the bulk flow properties are observed. By solving for a time-independent solution, the computational cost of a fluid simulation can be significantly reduced.

For many aircraft fluid simulations, a steady-state fluid model can be used. While further research is necessary to fully evaluate whether steady-state simulations capture all of the flow physics around an aircraft, they are known to capture the most significant phenomena which will drive the behavior of the swept stroke [95]–[98].

2.3.2 Viscous Effects

Viscous effects generate the aerodynamic boundary layer and small-scale turbulent structures (linked to the fluctuating velocity component) which are critical to modeling many flows. Different approaches to modeling viscosity can resolve these features to different extents, outlined in table 2.2.

Table 2.2: Birds-eye-view of mathematical models for resolving viscous effects

	Boundary layer	Fluctuating component
Fully-resolved (transient)	Resolved	Resolved
Reynolds-averaged	Resolved	Modeled
Reynolds-averaged with wall functions	Modeled	Modeled
Inviscid	Ignored	Ignored

Small-scale, transient turbulence has been found to play a critical role in driving reattachment in the lightning arc [39]. However, resolving these features at the scale of a commercial aircraft is too costly with modern computing capabilities, especially since the proposed model is designed to serve as an engineering and certification tool which could involve running many tens, hundreds, or even thousands of different simulations.

While the aerodynamic boundary layer does impact the swept stroke [39], the distribution of many strikes over the aircraft surface could be independent of this near-wall behavior. If

this is the case, an inviscid fluid model may be sufficient. Otherwise, Reynolds-Averaged Navier Stokes (RANS) models may perform better. Fully resolved models are not simulated in this work since they are too complex for an entire aircraft (conflicting with goal [†2](#)) and previous work has already documented the effect of using such models [39]. Section [4.1](#) will compare the performance inviscid and RANS models in the context of swept stroke simulation.

Chapter 3

Numerical Implementation

The physical model described in section 2 was implemented computationally in C++, using the Visualization Toolkit (VTK) [99] to process geometry and the Message Passing Interface (MPI) [100] for parallel simulation. The model takes Computational Fluid Dynamics (CFD) flowfields as an input, formatted as a VTK unstructured grid (*.vtu), a common file type which can be generated by most CFD programs. The complete simulation workflow, from CAD model to zoning diagram, is illustrated in figure 3.1. The tool developed in this work has been named ‘Simulation Workflow for Electromagnetic Effects: Physics-based Zoning’ (SWEEPZ).

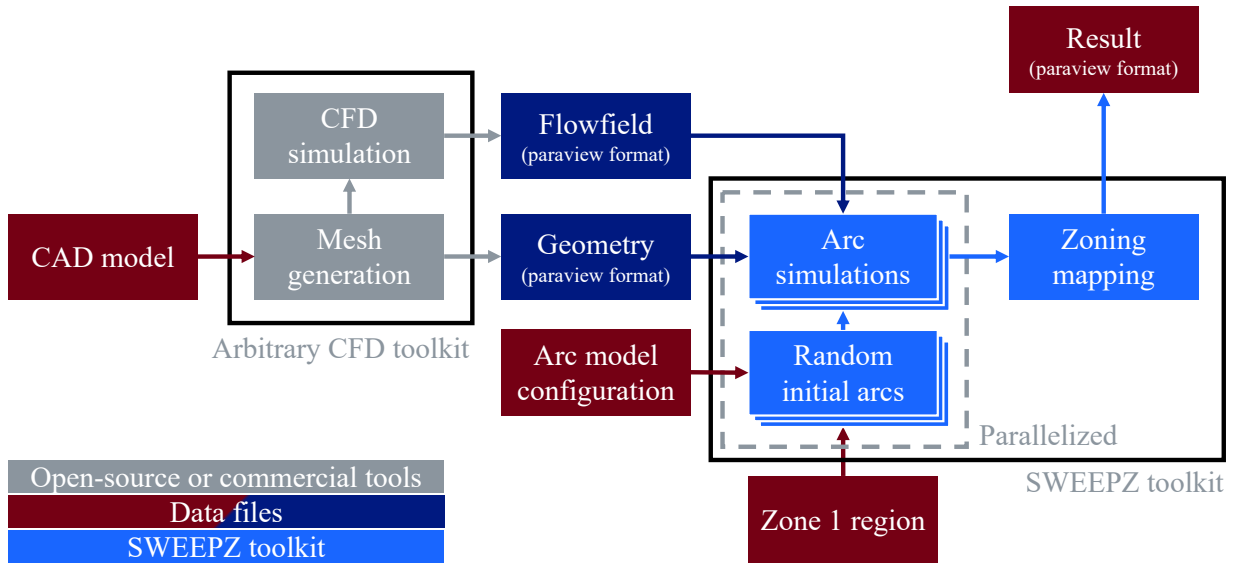


Figure 3.1: Zoning simulation workflow.

3.1 Arc Model

3.1.1 Spatial Discretization

The arc core is modeled based on figure 2.1 and discretized in figure 3.2. The arc is initialized with more points closer to the surface in order to capture the higher velocity gradients near the wall. Equation 3.1 is used to prescribe the spacing of points in the arc, where \vec{x}_i is the position of point i , \vec{x}_0 is the starting point of the arc, \vec{L} is the vector representing the arc length, and N is the total number of arc points.

$$\vec{x}_i = \vec{x}_0 + \vec{L} \left(\frac{i}{N} \right)^{1.5} \quad (3.1)$$

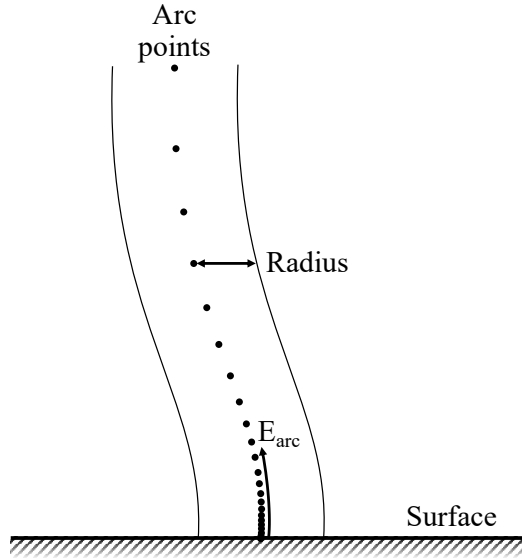


Figure 3.2: Numerical model of the lightning arc.

Perfect advection of the arc in the CFD flowfield is achieved using a Lagrangian formulation of the 1st-order forward Euler method to integrate over discrete time steps. This formulation is given in equation 3.2, for point i at time t . The velocity at a given point, \vec{v}_i is found by linearly interpolating the CFD velocity flowfield using a `VTKProbeFilter`.

$$\vec{x}_i^{(t+\Delta t)} = \vec{x}_i^t + \vec{v}_i \cdot \Delta t \quad (3.2)$$

The lightning arc hangs on to trailing surfaces and is swept backwards from them, leading to significant elongation. In the discretized representation, this can create extremely long gaps between the first two points in the arc. To avoid a loss of resolution in this section, and to capture any reattachment which could occur from this section of the arc, points are added to fill these large gaps. Figure 3.3a illustrates how this is achieved by removing the penultimate point in the farfield and placing it at the midpoint of the large gap. This is triggered when the gap between the first two points exceeds an arbitrary threshold defined based on the arc length L_{arc} and the number of points N_{points} in equation 3.3. This threshold

was found to work well for a range of arc configurations, but could easily be changed without significantly impacting results.

While it would be preferable to dynamically adjust the number of points in the arc based on its length, the computational implementation stores arc data in a `VTKPolyData` object which is difficult to resize, especially when generating output files containing time-dependent arc data.

$$\text{large gap threshold} = 20 \frac{L_{arc}}{N_{points}} \quad (3.3)$$

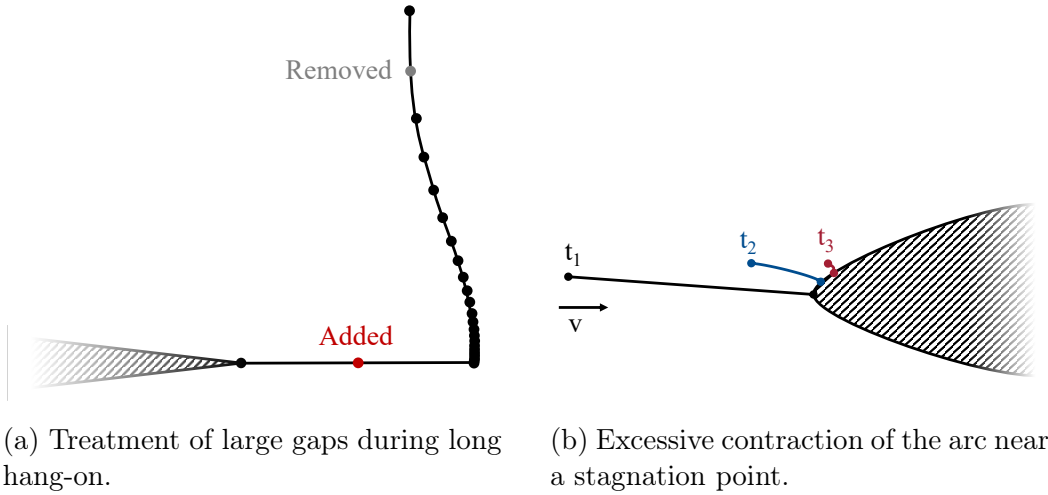


Figure 3.3: Numerical issues caused by arc elongation and contraction.

While the real arc extends much further into space, the numerical arc has a finite length. As well as checking for excessive elongation, the model also monitors arcs for excessive contraction. If the arc is initialized in a similar direction to the flow near a stagnation point, it can become extremely short, as illustrated in figure 3.3b. If an arc is found to be less than 10% of the initial arc length, its simulation is skipped since it will not contribute a meaningful result to the solution. Such arcs, in reality, are likely to repeatedly reattach to the initial attachment point so are not of significance to the zone 2 region.

3.1.2 Reattachment and Reconnection

Reattachment and reconnection are assessed according to the two criteria outlined in section 2.1.1. The discretized implementation is illustrated in figure 3.4. When reattachment or reconnection occurs, the points on the old arc segment are moved to the new arc segment and distributed according to the non-linear spacing discussed in section 3.1.

For reattachment, the potential at each point in the arc is calculated by numerical integration of its internal electric field between the root and the point in question. The distance to the nearest point on the surface is computed and used to find the (uniform) electric field between the arc and the surface at that point. If this exceeds the specified breakdown field strength, reattachment is triggered. Reattachment is assessed starting with the furthest

point from the surface, moving towards the root. If a point reattaches, it can be guaranteed that none of the points between it and the surface will trigger secondary reattachment so they do not need assessing and computing power can be saved.

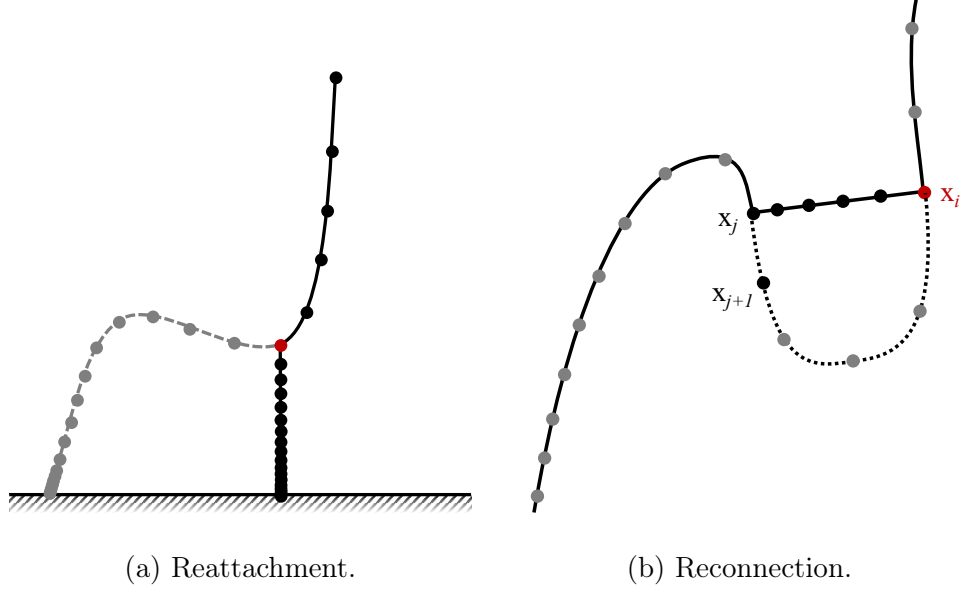


Figure 3.4: Numerical implementation of reattachment and reconnection.

Reconnection is also evaluated using the potential at each point in the arc, relative to every other point. To prevent adjacent points from ‘reconnecting’, an additional condition is required to ensure that a loop is actually present in the arc. This is given in the first section of equation 3.4, which ensures that point x_{j+1} is further away from x_i than x_j as illustrated in figure 3.4b. Within the square brackets in equation 3.4, the first condition tests for breakdown-triggered reconnection, and the second condition tests for radius-triggered reconnection.

$$(\|\mathbf{x}_i - \mathbf{x}_{j+1}\| > \|\mathbf{x}_i - \mathbf{x}_j\|) \cap \left[\left(\frac{|V_i - V_j|}{\|\mathbf{x}_i - \mathbf{x}_j\|} > E_{bd} \right) \cup (\|\mathbf{x}_i - \mathbf{x}_j\| < r_{arc}) \right] \quad (3.4)$$

Because reconnection involves comparing every point to every other point, it experiences a computational complexity of the order $\mathcal{O}(N^2)$, where N is the number of points in the arc. The rest of this model is of complexity $\mathcal{O}(N)$, so including reconnection could impact model performance for large numbers of points. However, the large size of the CFD mesh means that substantially more simulation time is spent executing VTK functions (interpolating velocity and finding the closest points on the surface) than evaluating reconnection. In keeping with goals [†1](#) and [†2](#), reconnection remains in the model.

Many mechanisms take place during each time step, including advection, reattachment, reconnection, and special treatment for long and short arcs. The order these are evaluated in can have some impact on results and, in keeping with goal [†1](#), the most physically relevant order was identified as shown in figure 3.5.

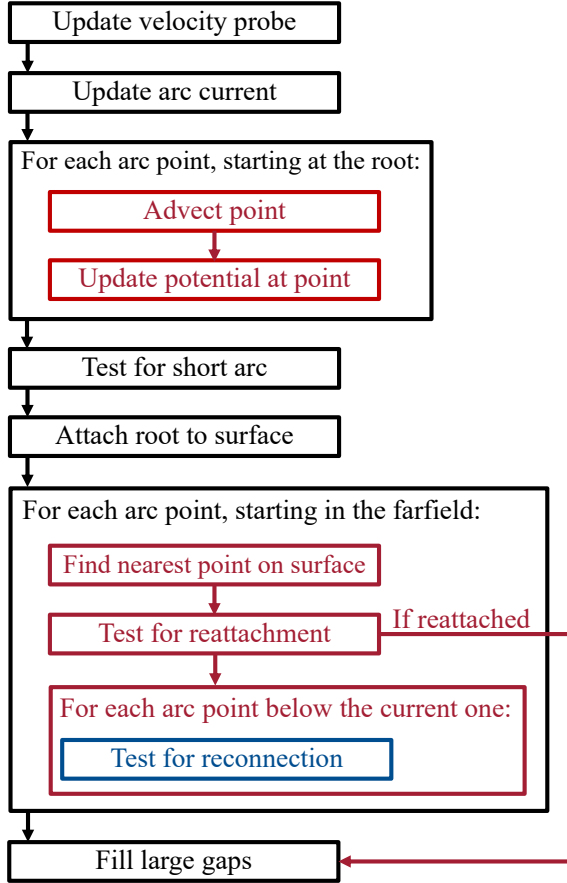


Figure 3.5: Flowchart of tasks during each arc time step.

3.1.3 Electrical Current Waveform

Due to the small (sub-microsecond) timescales in the ARP-defined lightning current waveform outlined in section 2.1.2, a simplified waveform was implemented in this model. This is visualized in figure 3.6.

The first return stroke (component A) is removed, since it occurs at initial attachment in zone 1 and is not relevant to the second lightning zone. Components B and C can be modeled in a very similar manner to the ARP specification, and component D ‘pulses’ are modeled using a current impulse over a single time step. The magnitude of the impulse is scaled to preserve the action integral, defined in ARP 5412 [25] and explained in section 3.3. Between component D pulses, the ARP model sets current to zero, but the proposed implementation instead maintains a small constant current, to the order of 1A. This improves the quality of current-related visualizations since it is otherwise difficult to identify where on the surface the lightning arc has touched. All of the idealized current waveform parameters are summarized in table 3.1, where an asterisk denotes a parameter with some stochastic variation.

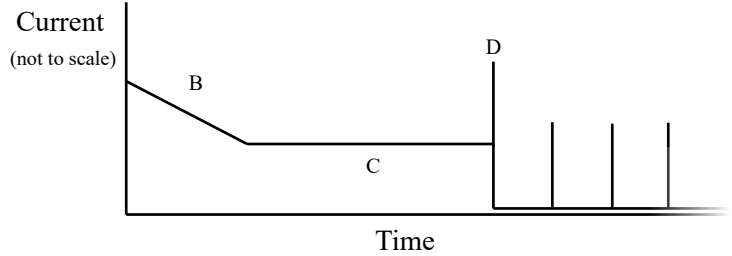


Figure 3.6: Model current profile.

Table 3.1: Idealized current waveform parameters

Component	Parameter	Value
B	Duration	5 ms
	Initial current	4400 A
	Slope, $\frac{\Delta I}{\Delta t}$	$8 \times 10^5 \text{ As}^{-1}$
C	Duration*	0.160 s
	Magnitude	800 A
D	Pulse 1 action integral	$3 \times 10^5 \text{ A}^2\text{s}$
	Pulse 2+ action integral	$1.5 \times 10^5 \text{ A}^2\text{s}$
	Pulse spacing*	47 ms
	Pulses	26
	Background current	1 A

In keeping with goals [†2](#) and [†3](#), stochastic effects are neglected for most current parameters, but the most significant variations are included since they come at almost no computational cost. Phase B current is delivered over a fixed duration of 5 ms, which is relatively small compared to the speed of the arc (so making small adjustments to the duration will have little effect). Phase C current, however, is of much greater significance. For simplicity, a uniform distribution between the 5th and 95th percentiles was used to select a duration for each arc instance, though a skewed gaussian may be more representative of the true distribution.

While ARP 5412 [\[25\]](#) does provide data on the number of phase D pulses (which vary significantly), this model should consider worst-case scenarios with the maximum observed number of pulses, which is 26. The time between pulses does vary substantially, so this was also randomly (uniformly) selected from between the 5th and 95th percentiles. A summary of the stochastic parameters relating to the current waveform is given in table [3.2](#).

Table 3.2: Stochastic current waveform parameters [25]

	Percentile	5%	50%	95%	Max
Phase C duration (ms)		77	160	344	500
Time between phase D pulses (ms)		12	47	180	200

3.2 Initialization

To inform the zoning of an aircraft design, many hundreds or thousands of slightly different lightning arc simulations must be run, each with a different initial attachment point and direction. An example of this is shown for the nose of an aircraft in figure 3.7.

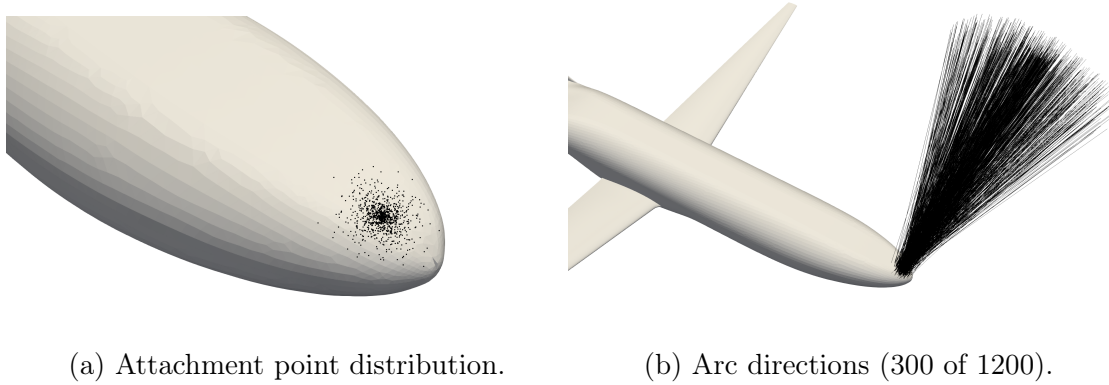


Figure 3.7: Random seed generation of 1200 arcs (D8 aircraft [101], [102]).

3.2.1 Attachment Point Generation

This model builds on work by Austin [40], which uses physics-based methods to compute the most likely initial attachment point. Since only a single attachment point is provided as the input for the swept stroke model, stochastics were introduced to generate many attachment points in the vicinity of the ‘most likely’ initial point.

It is assumed that the distribution of lightning arcs around a computed attachment point will be approximately gaussian, with a user-specified ‘ 3σ ’ distance inside of which 99.7% of all arcs will attach. Specifically, the univariate (1 dimensional) gaussian distribution is mapped to two dimensions by ‘revolving’ about the mean and then mapping to a 3D surface using the method described below, which was chosen because it is representative of a spherical multivariate gaussian [103] and it is feasible for implementation using the VTK package, which does not include a multivariate Gaussian function. More details on the bivariate Gaussian distribution are provided in appendix A.

Starting at the most likely attachment point, a random surface-parallel direction is generated. The program then follows this direction along the surface by a random distance, generated from the absolute value of a gaussian distribution centered on zero. At each cell

edge, the direction vector is rotated about the edge until it lies on the surface of the adjacent cell. This is shown for an arbitrary geometry in figure 3.8.

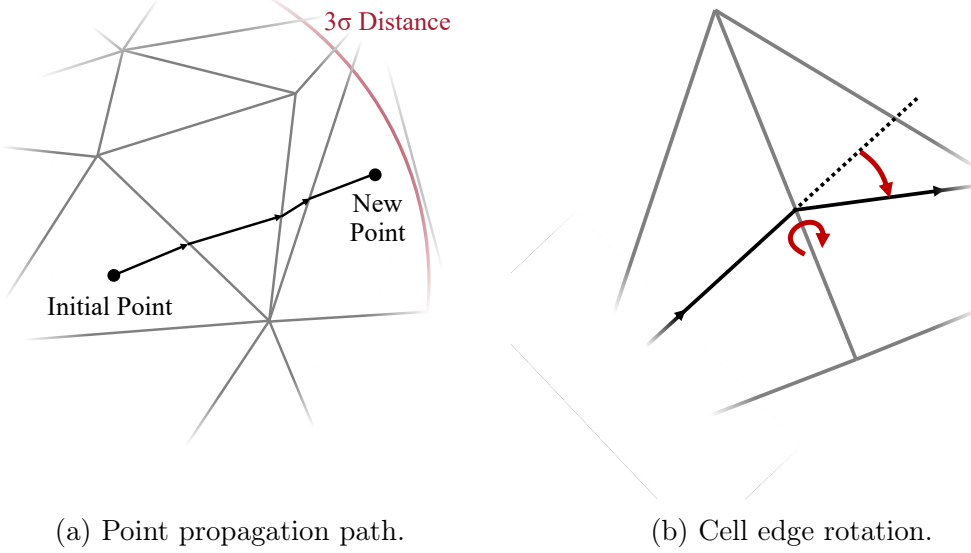


Figure 3.8: Attachment point propagation technique.

3.2.2 Field Direction Generation

A random atmospheric electric field direction is selected from a range within a cone defined by the user. A uniform distribution is used, representative of the output of an initial attachment point model, which provides a range of equally likely field directions for which a given attachment point is expected to activate.

The cone is defined by the initial field direction down its center, and the cone angle. Two random angles are then generated; one in the range from -180° to $+180^\circ$, and another between 0° and the cone half-angle. An arbitrary rotation axis is defined normal to the initial field direction, which is then rotated by the first random angle. The initial field direction is then rotated about this axis by the second random angle, yielding a random field direction. This is illustrated in figure 3.9.

Generating the attachment point and field direction both involve rotating a (unit) direction vector \hat{v} about a (unit) axis vector \hat{a} by angle α . This was performed using, Rodrigues' rotation formula [104], given in equation 3.5.

$$\hat{v}' = \cos(\alpha)\hat{v} + \sin(\alpha)(\hat{a} \times \hat{v}) + (1 - \cos(\alpha))(\hat{a} \cdot \hat{v})\hat{a} \quad (3.5)$$

3.3 Model Outputs

Along with the option to export time-series data for each individual arc, the model returns aggregate data for the interactions of all arcs with the aircraft surface. For every arc simu-

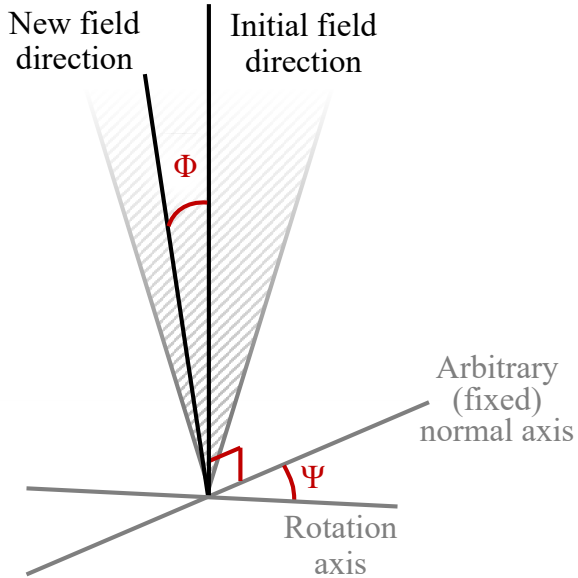


Figure 3.9: Field direction seed generation.

lation, the **attachment probability**, **dwell time**, **charge delivery**, and **action integral** are calculated inside each surface cell. The metrics are updated every time step, inside every surface cell which the arc touches, as illustrated in figure 3.10. The aggregate of these metrics over the aircraft surface can provide engineering insights for zoning and lightning protection.

3.3.1 Attachment Probability

Cells are assigned a value of either 1 or 0 to indicate if they are touched by the arc. In each cell, the average weight is found over all arc simulations and divided by the square root of the cell area. While time-dependent parameters are influenced by cell area (section 3.3.2), the probability of an arc being swept through a cell is a function of the cell width perpendicular to the arc motion, but not the cell length parallel to the arc motion. This is approximated by taking the square root of the area and is explained in appendix B.

3.3.2 Additional Metrics

The time-dependent metrics dwell time, charge delivery, and action integral are defined below. Dwell time describes how long the lightning arc spends in contact with each cell. Charge delivery measures the net electrical charge which passed through the arc while it was in contact with that cell. And action integral is a metric defined in ARP5412 [25] which is a good measure of the energy passing from the arc to the surface. This most closely correlates to damage caused by direct effects.

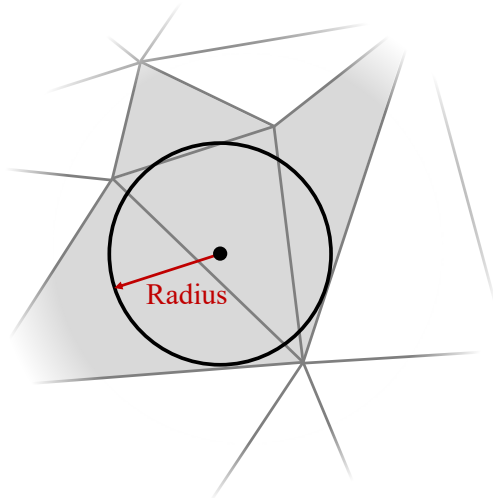


Figure 3.10: Cells touched by the lightning arc.

$$\begin{array}{ccc}
 \int dt & \int Idt & \int I^2 dt \\
 \text{Dwell time} & \text{Charge delivered} & \text{Action integral}
 \end{array}$$

While current-related parameters are calculated by the model (at little computational cost), they have been found to be of little value due to the highly stochastic nature of the current waveform. Almost any part of the swept stroke could feasibly experience a high-current impulse, so the charge delivery and action integral are not analyzed in detail in this work.

Before these metrics are aggregated, they are normalized by the cell area. This gives each metric in terms of an ‘area density’; for example, dwell time in seconds becomes dwell time per unit area in seconds per square meter. This accounts for variations in cell size, which affect the attachment probability as well as the time the arc spends in the cell. Normalization is explained in appendix B.

Aggregate data is computed using both averages and maxima. The average of each quantity is representative of how strikes should be expected to behave and could be useful for understanding where the majority of current flow or direct damage may occur. The maximum dwell time in a given cell is also a useful metric for determining how long the arc may ‘hang on’ to a certain point. This is useful when defining zone 2B (swept stroke with long hang-on, see table 1.1).

3.4 Computational Fluid Dynamics

Conducting accurate fluid simulations is critical to maintaining the accuracy of the swept stroke model. Computational Fluid Dynamics (CFD) programs are a powerful toolkit for fluid simulation, but it can be extremely easy to generate spurious results which only appear to be correct [94]. While CFD is not the primary focus of this work, effort was made to find a robust CFD methodology for this model. CFD parameters and solvers are discussed in more detail in appendix C. As explained in section 2.3, both viscous and inviscid fluid models were tested in this work.

3.4.1 Viscous Simulations

Viscous flow solutions were obtained using Flow360, a powerful ‘all-in-one’ CFD tool which automates mesh generation and solution submission on specialized high-performance hardware [97], [105]. It generated high-fidelity viscous CFD solutions in a matter of minutes, instead of the hours that conventional CFD codes often require.

Flow360’s mesh generation tools have been carefully validated using mesh refinement studies by Fitzgibbon et al. [97]. Aside from taking care to properly resolve the boundary layer by specifying a suitably small first layer thickness, it was very easy to generate a high-quality mesh for any geometry in Flow360, illustrated for the F-106B in figure 3.12a. The first-layer thickness was validated by inspecting the solution to confirm that the y^+ value did not exceed 1.0 anywhere on the aircraft surface [94].

Default solver parameters were mostly used as these have been well-tuned for similar CFD cases. Convergence was monitored with the help of residuals shown in figure 3.11. The output files from Flow360 were much bigger than those from SU2 because the automatically generated domain extended a much greater distance into the freestream. This means that they usually exceeded 5GB in size, so were cropped to a smaller dimension using Paraview [106] for processing in swept stroke simulations. This is appropriate because the farfield beyond two arc lengths from the aircraft is rarely used in these simulations.

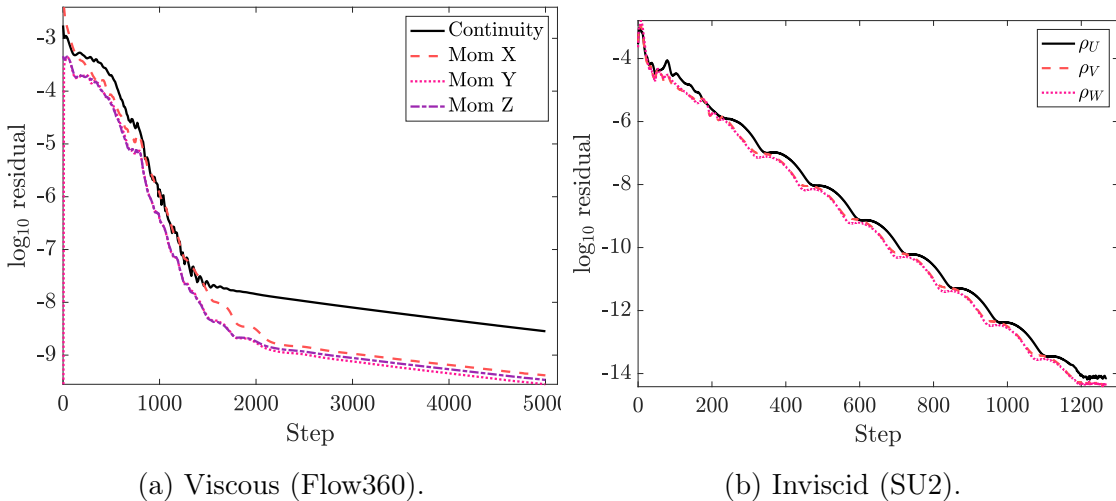


Figure 3.11: CFD residual plots for simulations of the F-106B aircraft.

3.4.2 Inviscid Simulations

SU2

SU2 is an open-source computational analysis package which includes computational aerodynamics tools [107]. It is widely used in the aerospace industry for simulating aircraft and other large vehicles and was utilized in this project to compute inviscid flow solutions over several aircraft. Specifically, the SU2 implementation of the compressible Euler equations were solved using a finite volume method over an unstructured grid, as described in SU2 documentation [108] and appendix C.

Mesh generation was achieved using the open-source Gmsh toolkit [109], which can generate unstructured tetrahedral meshes in a number of CFD-compatible formats, including SU2. A customized refinement field was used to achieve a relatively small surface mesh (necessary to accurately capture lightning behaviour), growing into a larger mesh in the farfield. The fluid domain was modeled as a sphere with a radius 3 times longer than the aircraft. The mesh used to model the F-106B is illustrated in figure 3.12b.

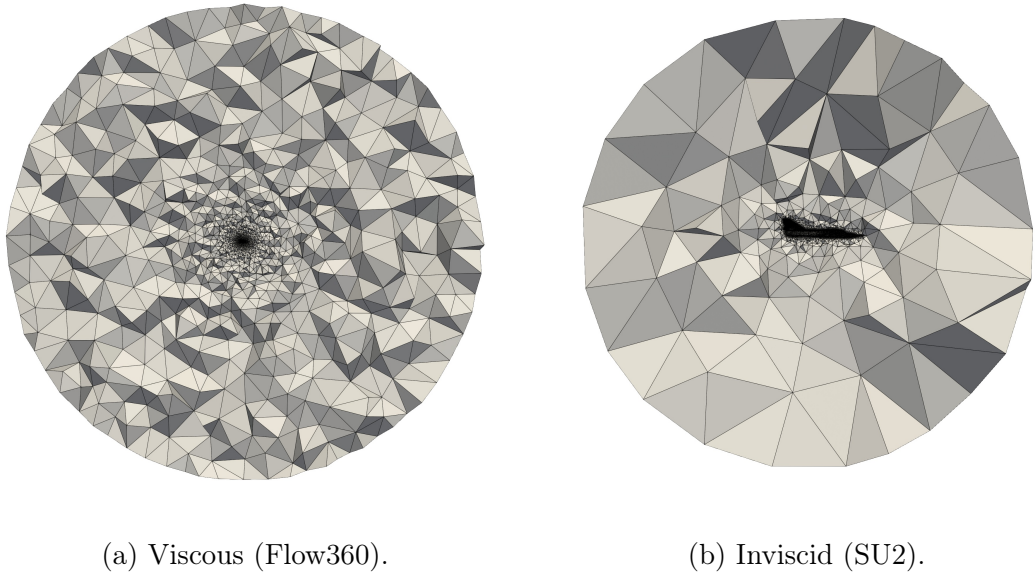


Figure 3.12: CFD mesh configurations for the F-106B aircraft.

Because the compressible Euler equations do not resolve viscous effects, no complex near-wall meshing is necessary and the CFD mesh can be more coarse than for a viscous CFD simulation. Validation of the SU2 solver is provided by Economou et al. [107].

SU2's robust default settings were predominantly used for these simulations. Residual plots shown in figure 3.11b demonstrate convergence. The F-106B was stopped after the change in average surface mach number fell below 10^{-14} , which is a representative stopping criteria for capturing the velocity flowfield.

StarCCM+

To confirm that the swept stroke model is compatible with any CFD code and to leverage the improved robustness of a commercial solver, StarCCM+ was used to simulate the unconventional aircraft tested in section 4.3. StarCCM+ is a widely-used CFD toolkit with a broad range of capabilities, including excellent mesh generation and inviscid fluid simulation.

The parameters used for StarCCM+ are outlined in appendix C.3.1. These were carefully chosen based on standard practices [94], [110], [111] and employ similar approaches to those used by SU2.

3.5 Verification of the Swept Stroke Model

Verification and validation was achieved, in part, by conducting a model ‘refinement’ study, in which different spatial and temporal discretizations of the arc were compared to confirm that simulation results were independent of the discretization.

Three metrics were used to quantitatively compare the results of different simulations. ΔA was defined as the proportion of the aircraft surface for which only one simulation - either the test case or the baseline - experienced attachment, but not both. The other metrics were the L1 and L2 norms of the change in probability per unit length, P , between the test case (P^{tc}) and a baseline case (P^{bl}), normalized by the cell area. ΔA represents changes in the *location* of attachment regions, while the norms quantify the change in *probability distribution* within those regions. The metrics are defined in equations 3.6, 3.7, and 3.8, where \mathbb{I} is the indicator function which dictates that the sum is taken over all cells where the condition is met.

$$\Delta A = \frac{1}{A_{aircraft}} \sum_{cells} A_{cell} \mathbb{I}((P^{tc} = 0 \cap P^{bl} \neq 0) \cup (P^{tc} \neq 0 \cap P^{bl} = 0)) \quad (3.6)$$

$$\|\Delta P\|_1 = \frac{1}{N_{cells}} \sum_{cells} \sqrt{A_{cell}} (P^{tc} - P^{bl}) \quad (3.7)$$

$$\|\Delta P\|_2 = \sqrt{\frac{1}{N_{cells}} \sum_{cells} (\sqrt{A_{cell}} (P^{tc} - P^{bl}))^2} \quad (3.8)$$

3.5.1 Temporal Refinement

Before testing a range of time steps, an estimate could be made for the optimum time step, which minimizes computational cost while achieving convergence to a valid result. This is given by equation 3.9, which is simply the arc diameter divided by freestream velocity. This enforces the condition that, with the exception of abnormally fast regions, the centerline of the arc never moves further than one diameter in one time step. This guarantees a smooth sweeping motion over the surface of aircraft, preventing the arc from skipping over any cells it should have come into contact with. The parameters used in this simulation are given in table 3.3.

$$\Delta t_{max} = \frac{\phi_{arc}}{V_\infty} \quad (3.9)$$

Table 3.3: Simulation parameters: time step refinement

N _{points}	400
Duration	0.175 s
r _{arc}	5 mm
L _{arc}	20 m
Speed (V _∞)	200 ms ⁻¹
Fluid model	Inviscid (Euler)
Δt _{max}	5 × 10 ⁻⁵ s
N _{timesteps} ^{min}	3500 s

Figure 3.13a illustrates the results of the temporal study. The ΔP norms reduce less quickly than ΔA . While the potential attachment region is not sensitive to time step ($\Delta A \rightarrow 0$ as $\Delta t \rightarrow 0$), the actual attachment probability at any point could still experience some change with time step, even for small values. This is not of significant concern, but it is important to recognize the limitations of the ΔA metric. A threshold of $\Delta A \geq 0.75\%$ was found to be an appropriate limit for the relative change in attachment area, corresponding to a minimum of 2500 time steps which validates the calculated minimum of 3500 in table 3.3.

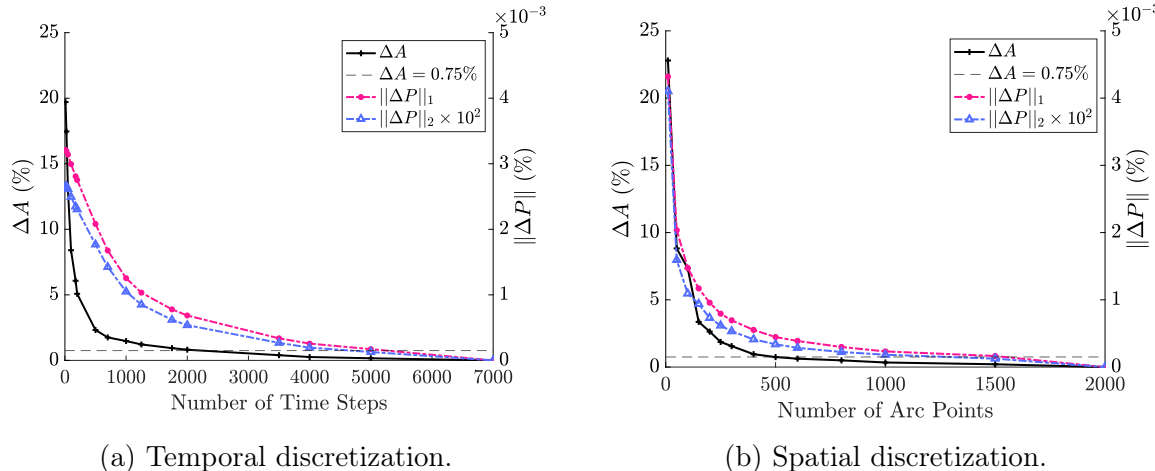


Figure 3.13: Results of the swept stroke model refinement study.

3.5.2 Spatial Refinement

It is difficult to properly define a ‘converged’ solution when changing the number of discrete points in the arc because of its coupling to the spatial discretization of the CFD solution.

Table 3.4 outlines key simulation parameters used in this study, with results shown in figure 3.13b.

Table 3.4: Simulation parameters: spatial refinement

Δt	0.000025 s
Duration	0.175 s
r_{arc}	5 mm
L_{arc}	20 m
Speed (V_∞)	200 ms ⁻¹
Fluid model	Inviscid (Euler)

Figure 3.13b shows how a sufficiently large number of points can be identified beyond which the relative change in error becomes small (below the threshold $\Delta A \geq 0.75\%$); in this case, around 500 points. While the error becomes almost zero above 1000 points, such a fine discretization excessively increases runtime.

Selecting the number of spatial points is a trade-off between accuracy and computational efficiency. As explained in section 3.1.2, the model scales with complexity $\mathcal{O}(N_{points}^2)$ with the spatial discretization, while it only scales with $\mathcal{O}(N_{timesteps})$ temporally. This means it is much less computationally expensive to increase the number of time steps than it is to increase the number of spatial points.

3.5.3 Number of Arcs

When conducting a Monte-Carlo type simulation, it is useful to quantify how many random samples are needed to capture the complete distribution. Because of the random current pulses, the charge delivery and action integral metrics could take many hundreds of thousands of arc simulations before their distributions begin to ‘converge’. However, the more important and relevant metrics for zoning (probability per unit length and dwell time) should converge faster. While many statistical methods for evaluating the number of samples do exist [112], these are difficult to map to a geometric output, so a ‘refinement’-based approach was used instead.

Figure 3.14 illustrates the results of simulations with different numbers of random samples, all using the simulation parameters outlined in table 3.5. It is evident that the result changes very little beyond 2000 arcs, with ΔA falling below the 0.75% threshold defined in the previous studies, and this study experiences much smaller values of $\|\Delta P\|_1$ and $\|\Delta P\|_2$. This means that, beyond approximately 2500 arc simulations, the effect of the number of samples is almost imperceptible from the effect of the spatial and temporal discretizations. For the sake of robustness, most simulations in section 4 use 6000 arcs to minimize the error induced by this sampling.

Table 3.5: Simulation parameters: Monte-Carlo sampling refinement

N_{points}	500
Δt	0.000025 s
Duration	0.175 s
r_{arc}	5 mm
L_{arc}	20 m
Speed (V_∞)	200 ms ⁻¹
Fluid model	Inviscid (Euler)

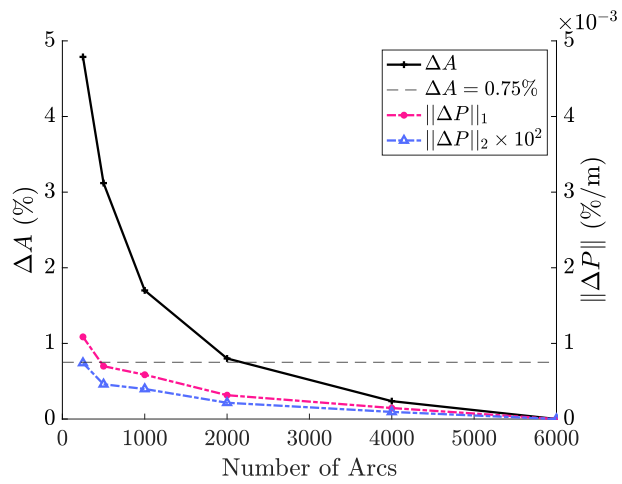


Figure 3.14: Results of arc count refinement study.

Chapter 4

Simulation of Aircraft Test Cases

4.1 Military Aircraft: Comparison to Results from the NASA Storm Hazards Program

4.1.1 The NASA Storm Hazards Program

From 1980-1986, NASA conducted experiments on a modified Convair F-106B in thunderstorms to gather data on aircraft-lightning interactions [1], [41], [42], [113]–[124]; this was called the Storm Hazards Program (SHP). The aircraft was struck by lightning more than 700 times, providing a statistically representative collection of lightning attachment points. To the author’s knowledge, the results of the SHP are the only publicly available data sets which record the individual paths of lightning swept strokes over an aircraft.

The SHP investigated a broad range of phenomena, gathering data on direct and indirect effects, initial attachment, and the swept stroke. Swept stroke attachment patterns were analyzed in test campaigns from 1980-1983 over 17 strikes and are summarized by Fisher et al. [41].

4.1.2 Simulation of the F-106B Aircraft

Since no freely available CAD models of the F-106B are available online, Fusion360 [125] was used to create a simplified model based on diagrams and technical reports [126], [127]. The model geometry is illustrated alongside the real aircraft in figure 4.1.

Swept stroke simulations were initialized using randomly generated sets of strikes populating the hemisphere in front of the nose, illustrated in figure 4.2. The initial attachment point was set to the tip of the probe at the front of the nose, with the 3σ distance equal to the length of that probe. While the mapping of the 2D gaussian behaves poorly for such small geometry (see appendix A), it is clear that the strikes are distributed in an appropriate manner, especially when evaluated against SHP attachment point records [41], [124].

Most F-106B simulations were conducted using the parameters outlined in table 4.1. These were selected based on the experimental flight conditions recorded by Fisher et al. [41], [42], [124]. The freestream density is defined using the International Standard Atmosphere [72] at an altitude of 20,000 ft (6,096 m). The arc radius, unless otherwise stated, refers to



Figure 4.1: F-106B aircraft geometry.

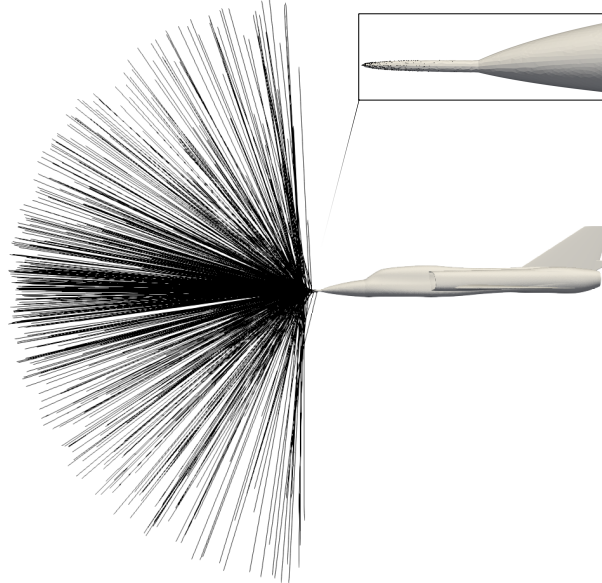


Figure 4.2: Initialization of 1200 strikes on the F-106B aircraft.

the radius after it has been scaled using equation 2.2.

4.1.3 Strike 8 from the 1981 Campaign

The first simulations validated the choice of fluid model by comparing results which attempt to replicate a strike recorded during the SHP [41]. The flight conditions during this strike are summarized in table 4.2, which are notably similar to those used for simulated results in table 4.1

The real strike was recorded attaching to the aircraft at the tip of the nose, sweeping aft over the engine inlet and then attaching to the vertical tailplane. Both viscous and inviscid simulations captured most of this behavior, but failed to model attachment to the vertical tail. Three potential causes of this discrepancy have been identified: (1) the initialization of the arc as a straight line, which does not capture the real shape of a lightning arc; (2) the simulated bank angle is 0° , while the real strike was recorded at -5.9° ; and (3) enhancement of the electric field near sharp leading edge surfaces is not resolved, as discussed

Table 4.1: F-106B simulation parameters

Freestream velocity	200 ms^{-1}
Altitude	6,096 m (20,000 ft)
Freestream temperature	268.15 K
Freestream density	0.521 kgm^{-3}
Pitch angle	2°
Arc length	20 m
Arc radius	9.3 mm
Arc points	500
Time step	0.000025 s
Simulation time	0.15 s

Table 4.2: Flight conditions for strike 8 from the 1981 campaign [41]

Date	August 16, 1981
True airspeed	212.9 ms^{-1}
Altitude	7,614 m
Ambient temperature	253.45 K
Pitch angle	3.2°
Bank angle	-5.9°
Precipitation	‘Negligible’
Turbulence intensity	‘Moderate’

in section 2.2.2.

Figure 4.3 shows snapshots of the simulated swept stroke before and after reattachment to the engine inlet, which occurred near a simulation time of 0.04675 seconds. The track of the simulated arc on the surface is shown in red and the attachment points recorded during the SHP are illustrated in green. Both fluid models captured the reattachment to the engine inlet, although surface tracks before and after reattachment are different. The inviscid simulation models smooth sweeping of the arc over the surface, which is to be expected since the wall ‘no-slip’ condition is not enforced with this model. The viscous model sweeps much slower but jumps less than the real arc would, because of the lack of small-scale fluctuations which are removed by Reynolds-averaging.

The Reynolds-averaged viscous model introduces a strong dependency between the rate of sweeping and the arc radius. This is because the near-wall section of the arc will advect at the flow speed one radius away from the wall surface. Approximating the thickness of the boundary layer using a turbulent flat plate model, $\delta_{99} \approx 0.37xRe_x^{-1/5}$ [128], the conditions in table 4.2 yield a thickness of 0.015 m at 1 m along the aircraft surface. For an arc radius of 0.005 m, this means advection is driven from a point within the boundary layer, where velocity gradients are high, so the rate of sweep could change significantly with radius. Because the viscous model sweeps slowly along the surface, it fails to properly capture all regions the lightning arc may touch. The inviscid model, on the other hand, will ‘fill’ gaps between individual re-attachment points giving a conservative solution for engineering models (meeting goals †2 and †3).

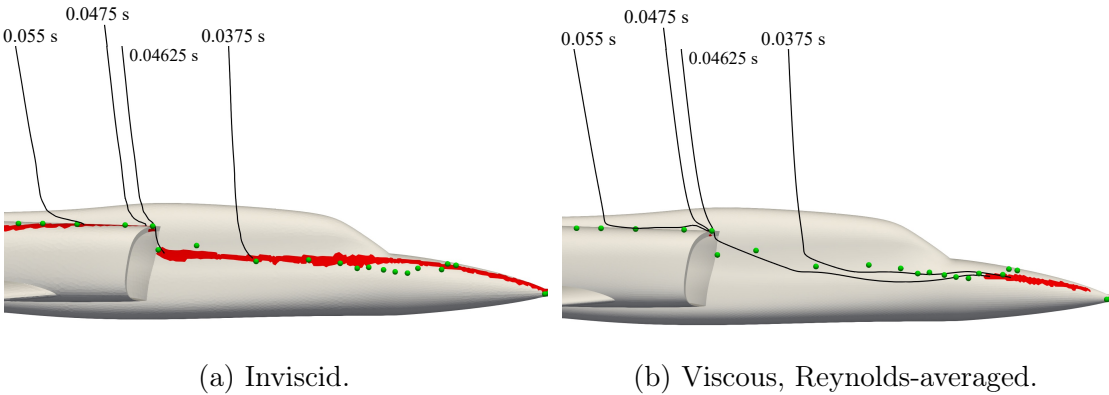


Figure 4.3: Swept stroke simulations for strike 8 of the 1981 campaign using different fluid models.

Figure 4.4 shows how the results of this simulation can be interpreted to understand the effect of different fluid models on the behavior of individual arcs. An inviscid model enables continuous sweeping which, although not necessarily physical, better captures the aggregate behavior of many arcs than the Reynolds-averaged viscous model, in line with goal [†3](#). The Reynolds-averaged viscous model and the inviscid model are both dominated by the geometric criteria for reattachment. The viscous model, however, fails to advect the near-wall segment of the arc sufficiently far before reattachment occurs, meaning part of the surface does not experience attachment in the simulation despite it being possible during a real strike, illustrated in purple in figure 4.4.

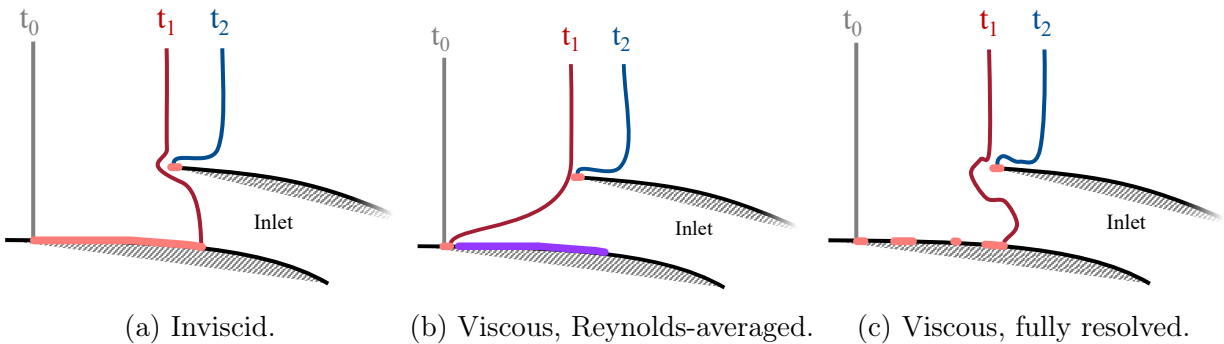


Figure 4.4: Behavior of the simulated lightning arc near the engine inlet using different fluid models.

While the inviscid model does further goal [†3](#), it is vital to consider its relevance to certain flow conditions to ensure that goal [†1](#) is also met. Specifically, use of an inviscid model will prevent simulations from correctly capturing behavior relating to;

1. **Flow separation** and wing stall. An inviscid model will not properly resolve separation of the flow, which could influence how the arc is swept over aerodynamic surfaces

at high angles of attack. This is unlikely to occur during normal stages of flight since stall is considered an ‘upset’ phase of flight [129].

2. **Vortex shedding** and wake turbulence. This includes wingtip vortices and turbulence aft of the fuselage which could significantly change the flow profile in some regions. These regions are predominantly aft of the aircraft so again shouldn’t significantly affect the results of aggregate simulations.
3. **Shock waves.** Transonic commercial aircraft often experience shocks on top of the wing surface, which can influence flow behavior [130]. This isn’t anticipated to significantly impact the swept stroke, although very little effort has been made to study the significance of supersonic effects on the lightning arc.

4.1.4 Strike 4 from the 1980 Campaign

The flight conditions during this strike are not provided in SHP records, although the aircraft altitude is known to have been 5,182 m [124]. Lightning entry is recorded at the tip of the nose, sweeping back over the cockpit canopy and then up the leading edge of the vertical tailplane. The simulated surface track is shown in figure 4.5, where the red track is the simulation and green dots are SHP data.

Having initialized the arc to be perfectly in line with the vertical tailplane, it is understandable that simulation results sweep smoothly over its leading edge. An interesting feature of this sweeping, exhibited in both simulated and real (SHP) data, is the tendency of the arc to temporarily detach from the leading edge, sweep over the top surface of the tailplane for a short distance, and then reattach to the leading edge. While the simulation appears to match this behavior, it is unclear whether the correct mechanism drives it. It is more likely that this is an artifact of the numerical discretization of the aircraft surface which happens to appear similar to the real behavior. The real cause of this artifact may be local electric field enhancement as discussed in section 2.2.2, although further work will be required to prove this theory. Some arc physics are evidently not fully resolved by this model, although this is not expected to have a significant impact on the aggregate distribution, so goal †3 is still met. To ensure goal †1 is met, the discretization of small-radius leading and trailing edges may require special care as these may induce spurious arc behavior.

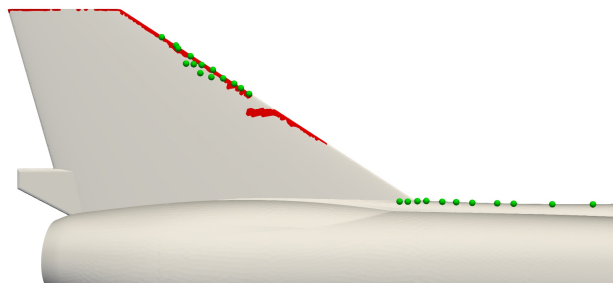


Figure 4.5: Strike 4 from the 1980 campaign over the F-106B tailplane.

4.1.5 Aggregate Strike Distribution

The distributions of thousands of swept stroke simulations are illustrated in figure 4.6, using both viscous (Reynolds-averaged) and inviscid fluid models. As explained in section 4.1.3, the viscous model fails to identify all of the possible swept stroke regions, making Reynolds-averaged fluid models particularly poor when considering goal †3. By contrast, the inviscid model adequately predicts regions of high attachment probability when compared to the aggregate of all swept stroke attachment points recorded during the SHP [41], [124], illustrated as green dots in figures 4.6 and 4.7. The agreement between inviscid simulation results and SHP data is further demonstrated in figure 4.7. Because of the superior performance of the inviscid model, both in terms of accuracy and computational cost, this fluid model shall be used for the rest of the simulations presented in this work.

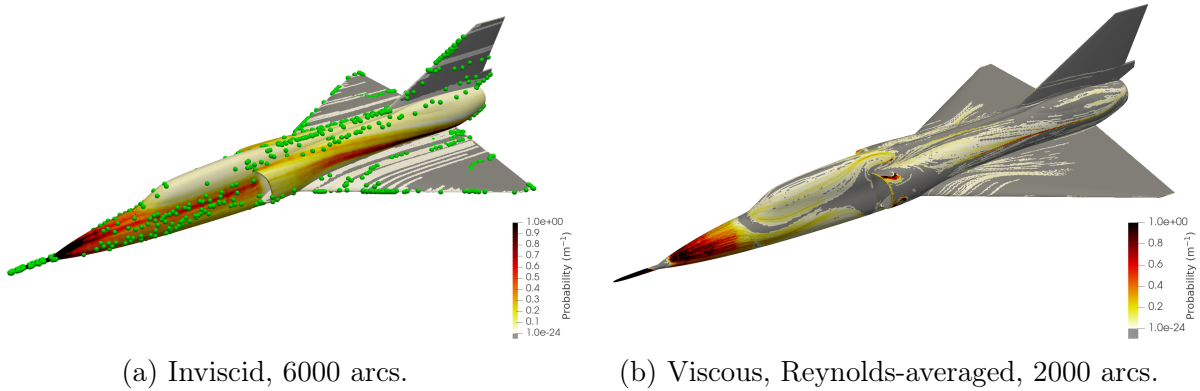


Figure 4.6: Swept stroke distributions on the F-106B aircraft using different fluid models.

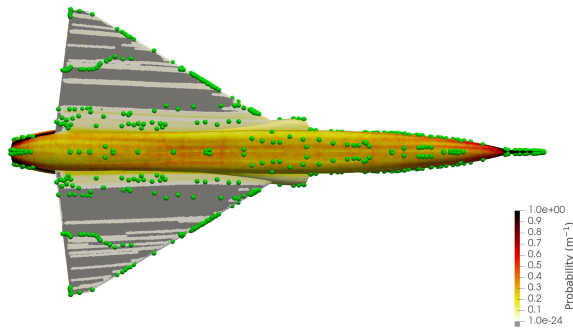


Figure 4.7: Inviscid swept stroke distribution on the F-106B aircraft, bottom view.

Four observations of the aggregated strike distributions can be made which show that simulations using an inviscid fluid model are valid;

1. The simulation successfully identifies possible swept stroke regions. In the case of this aircraft, these include most of the surface, with lower probability of attachment on the wings and tailplane.

2. The simulated probability per unit length mostly maps to the real distribution of attachment points. This is especially evident near the front of the aircraft and below the cockpit canopy, where the highest attachment probabilities occur.
3. The simulation successfully predicts lightning attachment inside the engine inlet, in line with SHP observations. This justifies the use of a duct instead of a more accurate treatment of the engine in the CFD simulation for the purposes of lightning zoning.
4. Simulated lightning arcs are swept along the leading edges of the wings and vertical stabilizer, in line with SHP observations.

Fisher et al. [42] propose a zoning analysis of the F-106B aircraft based on the attachment points identified during the SHP. Their conclusions agree with these simulations, noting that the entire aircraft is at risk of experiencing swept-stroke attachment, so there are no zone 3 regions. Identification of regions of long hang-on (essentially all trailing edge surfaces) agree between the SHP and simulated results. Fisher et al. noted that the inside of the engine inlet should be treated as zone 2A, which the computational model also demonstrated.

4.1.6 Sensitivity Analysis

A sensitivity analysis was conducted to better understand the effect of different simulation parameters on results. The arc radius was varied within the bounds of radii identified in section 2.1.2. Flight conditions, namely altitude, pitch, and yaw, were also varied to explore their effect on results. Changing flight conditions involved first repeating CFD simulations with the new parameters. Table 4.3 outlines the tests conducted during the sensitivity analysis, where the ‘case’ refers to the sub-figures in figure 4.9. The metric ΔA , defined in section 3.5, was used to quantify the difference between each case and the baseline to supplement qualitative comparisons.

Table 4.3: Sensitivity analysis for F-106B simulations

Radius (mm)	Altitude (m)	Yaw (°)	Pitch (°)	Case	ΔA
9.3	6,096	0	2	a	0.0
3.7	6,096	0	2	-	7.2
18.6	6,096	0	2	-	7.4
37.2	6,096	0	2	-	8.8
5.8	1,524	0	2	b	6.7
6.7	3,048	0	2	c	6.6
9.3	6,096	5	2	d	29.6
9.3	6,096	0	5	e	22.1
9.3	6,096	0	15	-	49.0

Model Sensitivity to Arc Radius

Given the range of values which could be used to define the lightning arc radius (outlined in section 2.1.2), it was important to understand how sensitive the model was to this parameter.

Figure 4.8 shows test cases with four different radii (values include the altitude scale factor), all of which are qualitatively and quantitatively similar. Provided the radius is relatively small (<30 mm), it has little effect on results, although ΔA is still larger than the threshold defined in the model refinement study in section 3.5. Therefore, while the radius does not significantly impact results, it cannot be wholly neglected.

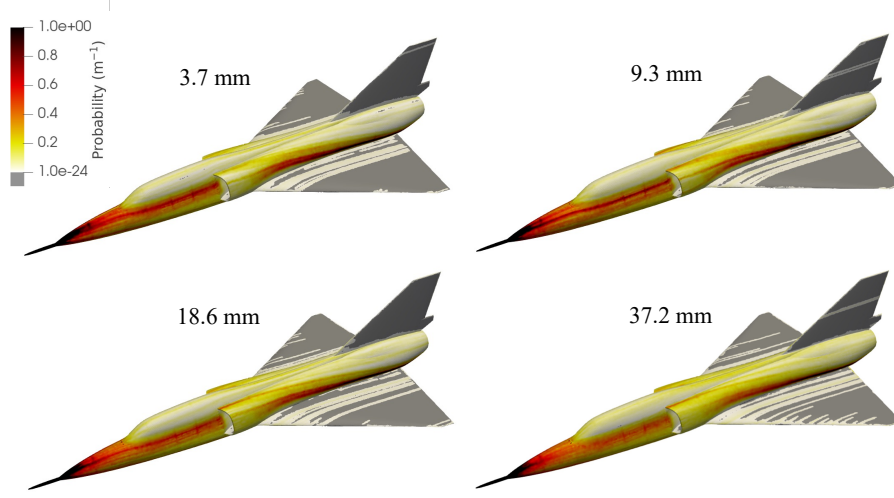


Figure 4.8: Radius parameter exploration; 2000 strikes on the F-106B aircraft.

Model Sensitivity to Aircraft Altitude

Similar to the radius, altitude has only a small impact on simulation results, as illustrated in the top row of figure 4.9. This is expected since, for most reasonable aircraft altitudes, the inviscid velocity flowfield won't significantly change, and any effects of altitude on the breakdown field strength are negligible because attachment is dominated by the radius-based criterion. Simulations at different altitudes do experience some change in radius, since the sea-level radius was kept fixed, although this test was repeated with a fixed absolute radius and found to produce almost identical results.

Model Sensitivity to Aircraft Orientation

Yaw angle has a significant impact on results, illustrated in figures 4.9 and 4.10. The relatively thin region of initial attachment points is projected underneath the starboard wing, which is intuitive given the change in flow direction. This significantly changes the distribution of the lightning strikes, so is of significance when considering a zoning result.

While yaw has a significant impact on the aggregate swept stroke behavior, aircraft spend much less time at large yaw angles than they do at high pitch. Evaluating the swept stroke at 5° and 15° pitch up demonstrates an even more severe effect than 5° yaw. These pitch angles represent a reasonable range for most aircraft during takeoff and climb [131]–[133]. Since many lightning strikes to aircraft occur near 5,000 to 10,000 ft [2], [134]–[137], this is an important stage of flight to consider when zoning.

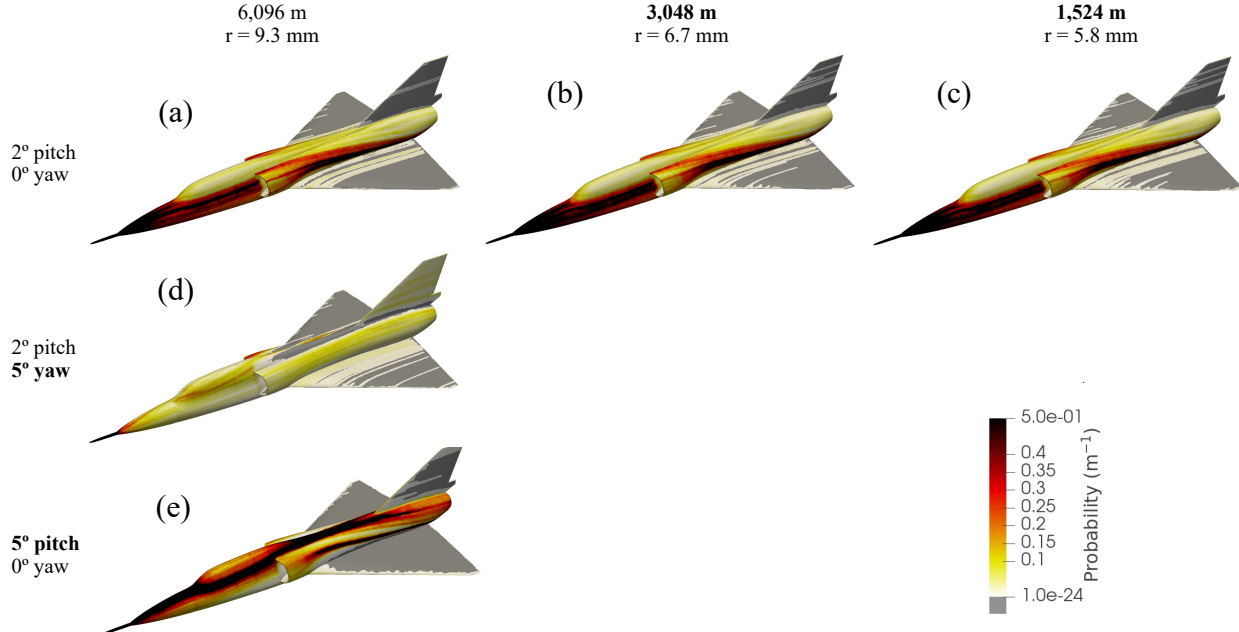


Figure 4.9: Altitude and attitude parameter exploration; 2000 strikes on the F-106B aircraft.

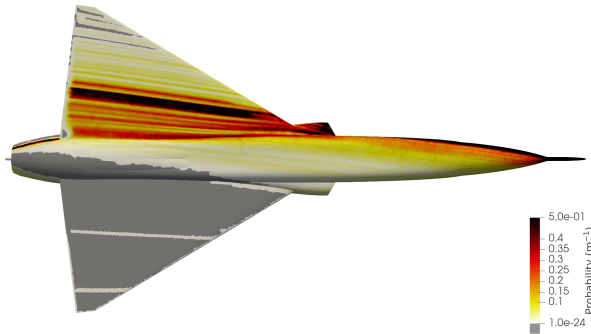


Figure 4.10: Distribution of 2000 strikes at 5° yaw.

Figure 4.11 illustrates the significant effect of pitch angle on the distribution of swept stroke attachment points, concentrating attachment points into a line along the top of the aircraft body. This intuitively makes sense since the top of the fuselage essentially becomes a trailing edge, beyond which airflow will not encounter another component of the aircraft. This result is dependent on the initial range of lightning arc angles.

The asymmetric behavior in figure 4.11b is caused by the breakdown of the inviscid fluid model for complex flows. At such a high pitch angle, the flow may become ‘separated’, but this phenomenon is dependent on the effects of viscosity. Because the inviscid model cannot resolve separation, it does not converge to the true velocity flowfield, leading to non-physical arc simulations.

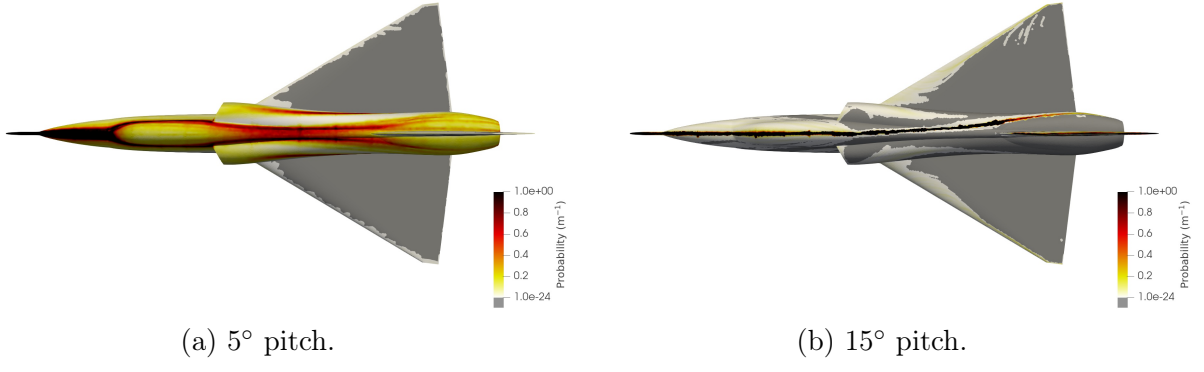


Figure 4.11: Distribution of 2000 strikes at high pitch angles.

4.2 Commercial Aircraft: Mapping Model Results to Lightning Zones

Verification of the numerical implementation in section 3.5 and validation of the model physics in section 4.1, demonstrate that goals [†1](#) and [†2](#) have been met. Goal [†3](#) was evaluated by using the model to generate zoning results for a generic commercial aircraft, as well as unconventional aircraft in section 4.3.

4.2.1 Simulation of a Commercial Aircraft

A generic commercial aircraft was modeled based on a design created by Yildirim [138]. The CAD model was simplified, solidified, and the engines were hollowed out to improve the relevance of CFD results. A computational mesh was generated using Gmsh [109], and SU2 [107] was used to run three CFD simulations at the flight conditions outlined in table 4.4. The simulation altitude was selected based on data presented in Rakov and Uman [2], [134]–[137] which recorded a significant number of aircraft lightning strikes at altitudes around 5,000 ft.

Table 4.4: Commercial aircraft simulation parameters

Freestream velocity	200 ms^{-1}
Altitude	1,524 m (5000 ft)
Freestream temperature	278.98 K
Freestream density	1.056 kgm^{-3}
Pitch angle	$0^\circ, \pm 2^\circ$
Arc length	20 m
Arc radius	5.8 mm
Arc points	500
Time step	0.000025 s
Simulation time	0.205 s

The initial condition for this simulation was extended to encompass the 270° spherical segment around the aircraft nose, with a 3σ distance of 1.0 m, which lies within the range of standard values for small commercial aircraft described in ARP 5414 [26]. The range of angles was specified to ensure that all possible attachment locations were identified, although this is expected to produce a conservative zoning result since arcs extending in some of these directions are more likely to initially attach to the engine cowling or wing tip. Figure 4.12 illustrates this initial condition for the first 500 (of 6000) simulated arcs.

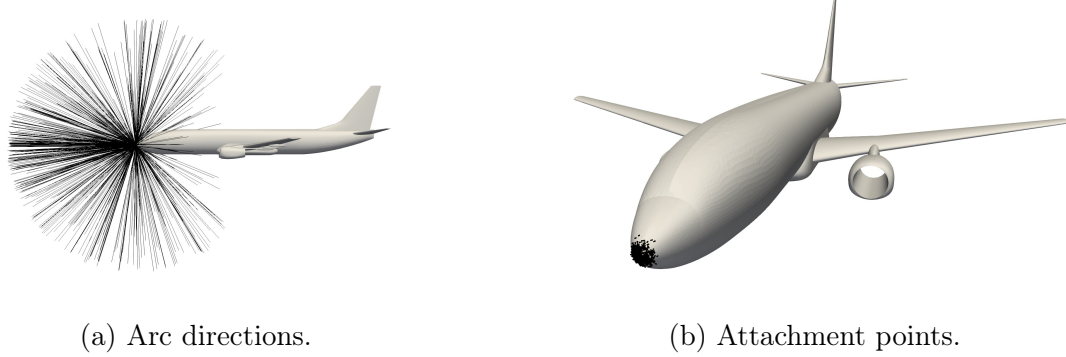


Figure 4.12: Initial conditions of first 500 simulated lightning arcs on a commercial aircraft.

Swept stroke simulation parameters are also outlined in table 4.4. These were selected based on descriptions of common flight conditions for aircraft during lightning strikes, summarized by Rakov and Uman [2], [134]–[137]. Because of the significance of pitch angle identified in section 4.1.6, simulations were repeated at three different angles of attack. The results of the simulation at $+2^\circ$ are shown in figure 4.13.

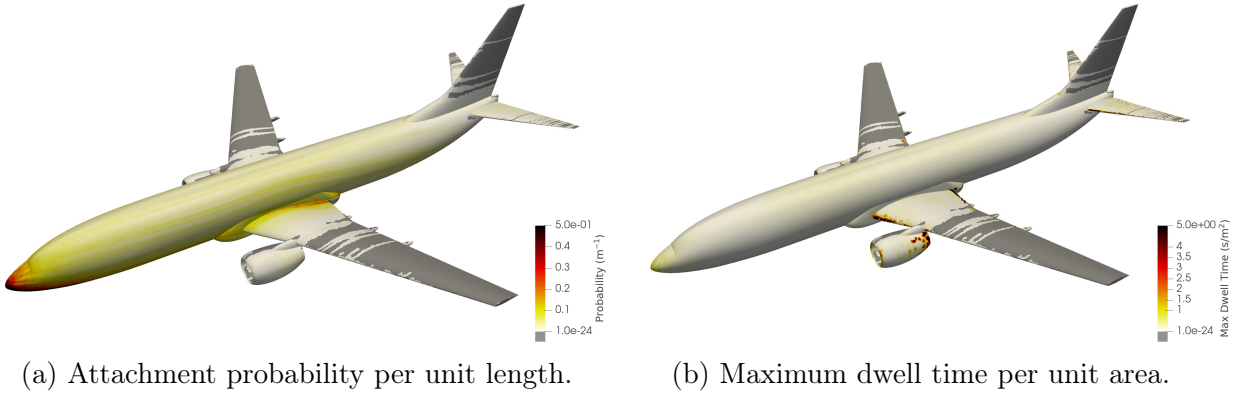


Figure 4.13: Commercial aircraft zoning simulation; 6000 lightning arcs, 0° pitch.

4.2.2 Zoning Mapping

In keeping with goal †3, a mapping tool was developed to convert the ‘raw’ output of the model described in section 3.3 into a zoning map for the second lightning zone. This involves

describing zones 2A and 2B, which correspond to the swept stroke region and the swept stroke with long hang-on respectively [26].

Because of the significance of pitch angle identified in section 4.1.6, simulations were conducted at several angles of incidence. When evaluating zoning, these were each tested individually, and the worst case from all simulations was taken for the final zoning result. Regions which meet the criteria for zones 2A and 2B are defined as 2B, since this zone requires a greater level of protection.

Zone 2A: Swept Stroke Zone

Zone 2A must contain all regions in which the swept stroke is likely to come in to contact with the aircraft. Theoretically, this could be defined using any of the metrics generated by the swept stroke simulations. Naturally, the attachment probability per unit length is the most appropriate for defining this region.

Several thresholds were tested and compared to published zoning results [26], [60], [139]. While it would be possible to define zone 2A as all areas which experience contact with a lightning arc in the simulation, this would be an over-cautious approach to zoning. Instead, a threshold of $P_{\text{attachment}} > 2.5\%/m$ was found to perform optimally. This means that, for a single lightning strike, at any point within zone 2A, there is at least a 0.0125% chance of the swept stroke passing within 5 mm (approximately one arc radius) of that point.

Applying this threshold to the statistics outlined in section 1, if this standard was used on every commercial aircraft worldwide, no more than 4 aircraft per year would experience instantaneous swept stroke attachment outside of zone 2A. This is a lower percentage of strikes outside of zone 2A than those recorded in the appendix of ARP 5414 [26], suggesting that this would be an improvement over current standards. Lalande and Delannoy [31] identified examples of swept stroke attachment in zone 3 on commercial aircraft, proving that some attachment outside of zone 2A can occur using current practices.

Zone 2B: Swept Stroke Zone with Long Hang-On

To identify swept stroke regions which may also experience long hang-on, a threshold can be defined for the lightning dwell time. The model calculates both the average dwell time and the maximum dwell time (across all of the arcs) at every point. The average dwell time is coupled to the probability distribution since the dwell time is averaged over all arcs, not just the arcs which passed through that cell. This means that points with long hang-on and a low attachment probability could measure the same average dwell time as points with no hang-on and a high attachment probability. Therefore, the maximum dwell time was used to define zone 2B, with the added criteria that zone 2B points must first meet the zone 2A threshold (i.e. the long hang-on must lie within a region of high attachment probability). A threshold of $T_{\text{dwell}_{max}} > 25.0 \text{ s/m}^2$ was found to best capture these regions.

Zoning Result

Applying this zoning mapping to the results on the generic commercial aircraft, the zoning diagram in figure 4.14a was generated. This is very similar to a zoning diagram published

by Boeing [60] for a similar aircraft. The planform images in figure 4.14 show a bottom view on the left side and a top view on the right side.

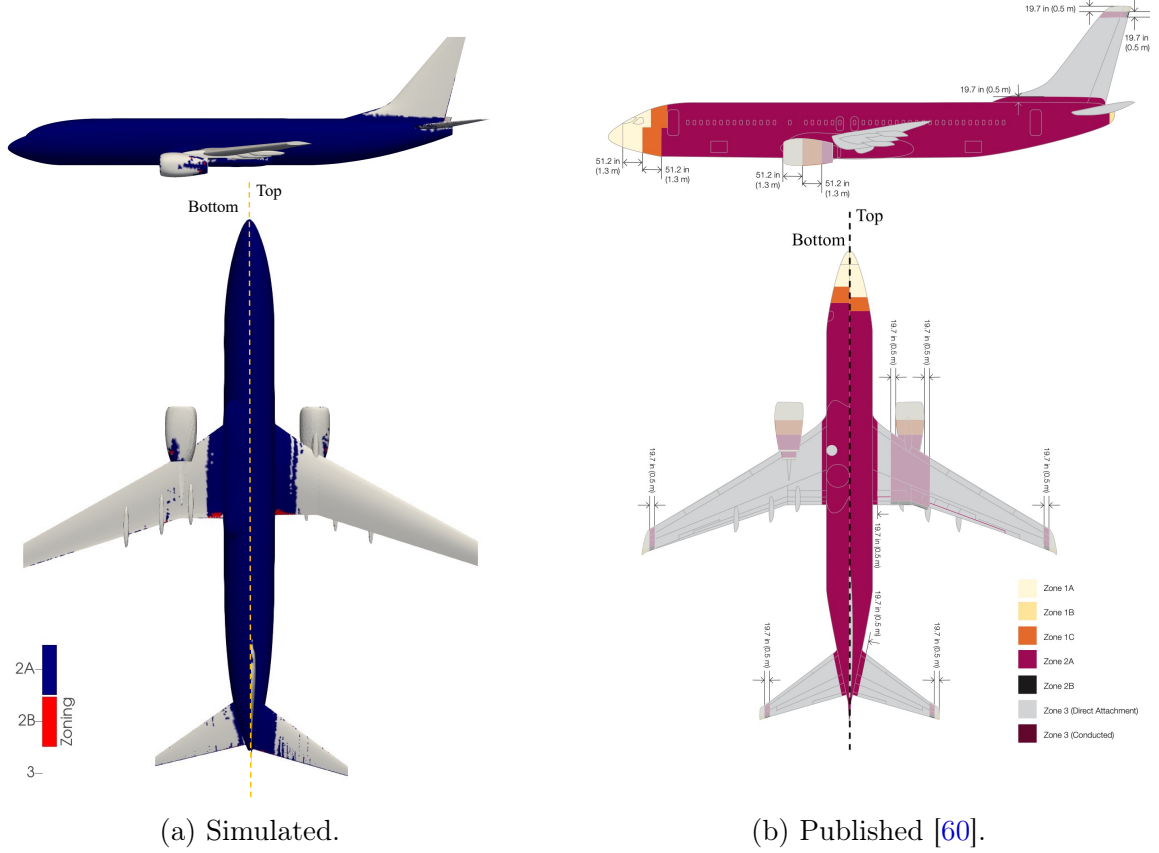


Figure 4.14: Commercial aircraft zoning results (fuselage only, excludes zone 1).

Only the initial attachment point at the tip of the nose was simulated, so the swept stroke from initial attachment to the engine cowlings is not modeled. This explains why the top view is missing the zone 2A region over the section of the wing behind the engine. While engine attachment was not included, the long hang-on region at the aft of the engine cowling is still present, since some arcs attached to the engine during their swept stroke. Other attachment points which were not included in the initial condition for this zoning result include the wing and empennage tips, which are more trivial cases.

A key feature of the recommended zoning approach is the extension of zone 2A by 0.5 m onto wing and empennage surfaces. This can be seen near the wing-fuselage joint on the published zoning diagram in figure 4.14b. This is successfully modeled by the simulated zoning result in figure 4.14a, although with a more significant extension of nearly 1 m. The broader extension onto the wing surface can be partly explained by the range of initial arc directions, some of which are unlikely to attach to the aircraft nose. Arcs which are nearly parallel to the aircraft wing (i.e. parallel to the pitch axis) are more likely to initially attach to the wing tip, so initializing them at the nose may not be physical. It is these arcs which most likely resulted in the broader extension of zone 2A over the wing surface. These effects

may disappear when the model is coupled to a physical model for zone 1, which can identify initial attachment points and the arc direction at those attachment points.

4.3 Unconventional Aircraft: Comparison to State-of-the-Art Zoning Methods

4.3.1 Zoning of a ‘Blended-Wing-Body’

Having demonstrated success zoning a commercial aircraft, the model was applied to its intended use case. As explored in section 1, novel designs including ‘Blended Wing Bodies’ (BWBs) are poorly understood from a zoning standpoint. A generic BWB was simulated and the result compared to a zoning map based on current best practices. Kruger [140] provides a high-quality BWB geometry which was used for these simulations, and which is conceptually similar to BWB concepts developed by major aircraft manufacturers [14]–[18].

An inviscid flow solution for the blended wing body was computed using StarCCM+ [111]. Using StarCCM+ allowed for the generation of a higher-quality CFD mesh and verified that the model is compatible with a range of CFD programs. The BWB CFD mesh is illustrated in figure 4.15. Simulation parameters are outlined in table 4.5. The initial condition for swept stroke simulations encompassed the hemisphere in front of the nose (similar to the F-106B test case in figure 4.2), but with a 3σ distance of 3.0 m, which is larger than the value used for the commercial aircraft (figure 4.12a) because of the larger radius of the BWB’s nose.

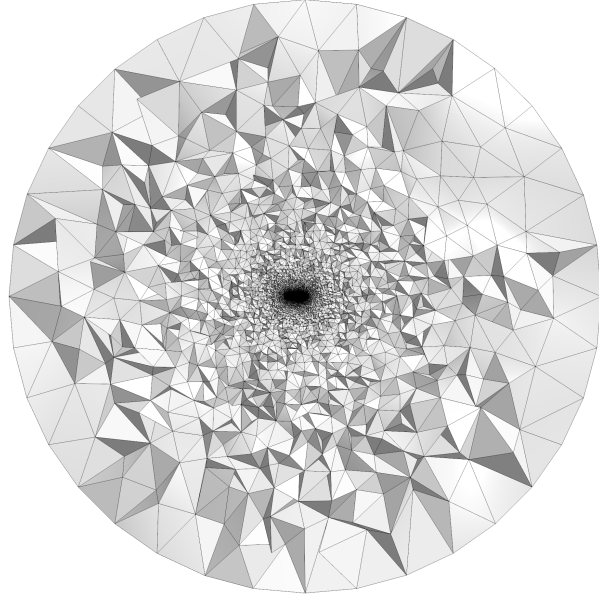


Figure 4.15: Computational mesh used for blended wing body CFD simulations.

The results of a swept stroke simulation at 0° pitch are illustrated in figure 4.16. Simulations (both CFD and the swept stroke) were repeated at $\pm 5^\circ$ and $\pm 10^\circ$ to better capture

Table 4.5: Blended wing body simulation parameters

Freestream velocity	100 ms^{-1}
Altitude	0 m
Freestream temperature	288.15 K
Freestream density	1.225 kgm^{-3}
Pitch angle	$0^\circ, \pm 5^\circ, \pm 10^\circ$
Arc length	30 m
Arc radius	5.0 mm
Arc points	500
Time step	0.00005 s
Simulation time	0.4 s

the effects of pitch on the distribution of strikes. Again, these results only consider initial attachment at the nose of the aircraft.

As demonstrated in section 3.5, just over 2000 arcs are necessary to capture the distribution of strikes over the F-106B surface, which was discretized into 257,000 cells. Most of these cells are larger than the arc radius, so it is appropriate to scale this limit by the number of surface cells for new calculations. The BWB surface mesh contained 461,700 cells. This means that at least 3600 arcs are required to reach a similar level of convergence, and 6000 were used for the results presented below.

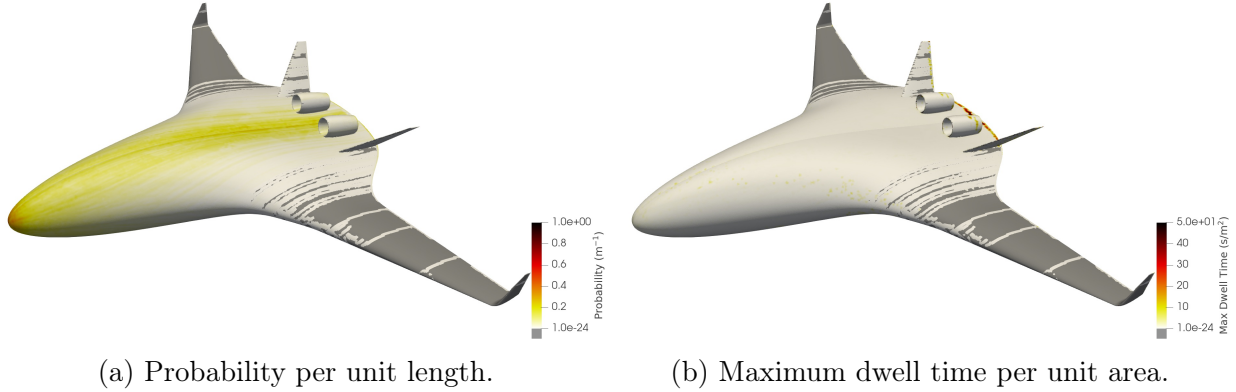


Figure 4.16: Blended wing body zoning simulation; 6000 lightning arcs, 0° pitch.

The simulated zoning result for the BWB is illustrated in figure 4.17. This uses the same thresholds for zoning mapping as the commercial aircraft in section 4.2.2. These results largely behave as expected; the zones in figure 4.17 are based solely on swept stroke arcs originating from the aircraft nose, so the effects of arcs attaching to the engines, empennage, or wing tips are ignored.

Using ARP 5414 [26], an attempt was made to generate a zoning map for the blended wing body which reflects current best practice. To satisfy regulators, this would likely need to be complimented by a significant amount of experimental testing.

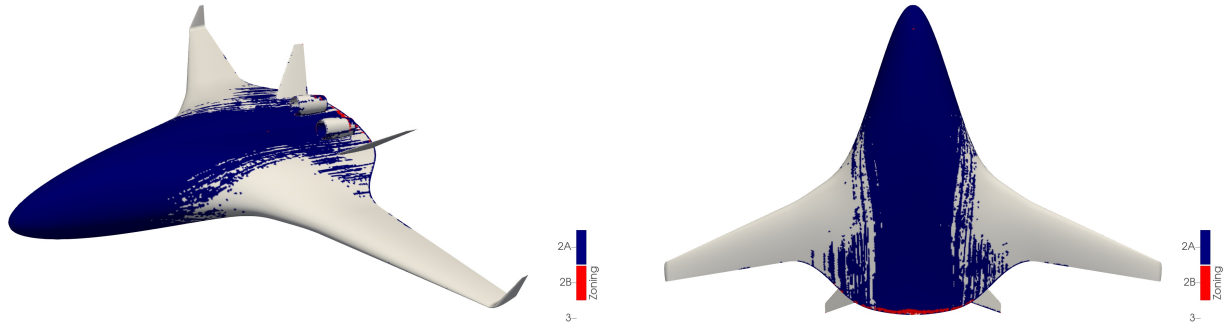


Figure 4.17: Blended wing body simulated zoning result, considering only attachment at the nose.

It is challenging to directly apply zoning standards to a blended wing geometry because of the lack of a clearly defined fuselage and wing. Without a physics-based understanding of where the swept stroke will move, the empirical models designed for ‘tube-and-wing’ aircraft may not be valid.

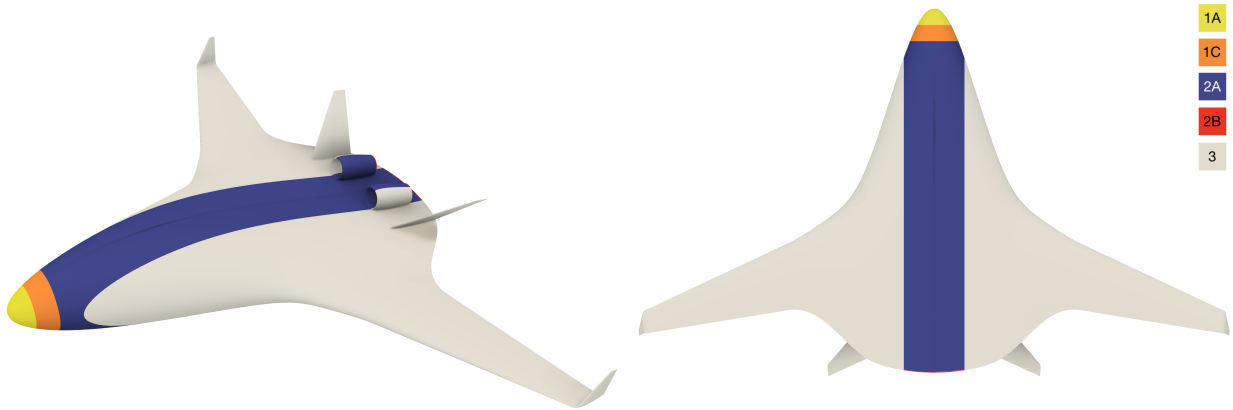


Figure 4.18: Blended wing body zoning result using aerospace recommended practices [26], considering only attachment at the nose.

Figure 4.18 illustrates a zoning diagram considering only attachment at the nose, ignoring the swept stroke aft of the engine cowling, wing tips, and empennage. Zones 1A and 1C were defined to be 1.3 m and 2.6 m from the aft of the initial attachment region respectively, based on the thresholds outlined in ARP 5414 [26] for a commercial aircraft at 130 ms^{-1} . The ‘initial attachment region’ was defined as the first 0.5 m of the nose, which is a conservative estimate based on the ARP. Zone 2A was defined as all regions aft of zone 1C, plus a 0.5 m lateral extension on either side. Regions of long hang-on (zone 2B) are defined as a 5 cm strip along all trailing edge surfaces within zone 2.

The simulated zoning result demonstrates a larger zone 2A region than the conservative zoning based on current recommended practices. An interested simulated phenomena is the swept stroke (2A) region which appears to begin halfway along the fuselage on the outboard sides. Deducing if this is truly physical behavior would likely require experimental testing but, if it is physical, this is a behavior which aerospace recommended practices do not consider. The breadth of the swept stroke region is also much larger for the simulated result; this may be sensitive to the size of the initial attachment region, which is difficult to estimate for this aircraft. Using a physics-based attachment point model (for example, Austin's model [40]) could improve the robustness of this zoning result.

4.3.2 Zoning of a ‘Truss-Braced Wing’

Another unconventional geometry which manufacturers are investigating is a ‘truss-braced wing’ (TBW) configuration, where a truss provides structural support for a high aspect-ratio wing [19]. A representative model of an aircraft using this configuration was created by adapting a model of a regional jet aircraft [141]. CFD simulations were conducted using StarCCM+ using the conditions outlined in table 4.6.

Table 4.6: Truss-braced wing simulation parameters

Freestream velocity	100 ms^{-1}
Altitude	0 m
Freestream temperature	288.15 K
Freestream density	1.225 kgm^{-3}
Pitch angle	$0^\circ, \pm 2.5^\circ, \pm 5^\circ$
Arc length	30 m
Arc radius	5.0 mm
Arc points	500
Time step	0.00005 s
Simulation time	0.4 s

Zoning results for the TBW are shown in figure 4.19 using the same thresholds as the commercial aircraft zoning mapping. An attempt to zone the aircraft using aerospace recommended practices is illustrated in figure 4.20. Unlike the blended wing body, it would be reasonable for an engineer to assume that the ARP can be directly applied to a truss-braced wing, but these plots demonstrate that this is not necessarily the case.

The ARP does appear to produce results which are similar to the simulated zoning. The simulated zoning result experiences a slightly broader region of attachment on the wing and the truss. The simulation also identifies a zone 3 region at the aft of the fuselage on each side, which is likely to be caused by the truss intercepting lightning arcs which would otherwise sweep into that region; this is not accounted for in the ARP. Long hang-on is identified at the leading edges of the wing and the truss, which is not modeled by the ARP. However, it is possible that this long hang-on is a numerical artifact and further simulations with a refined CFD mesh are needed to confirm whether this is the case.

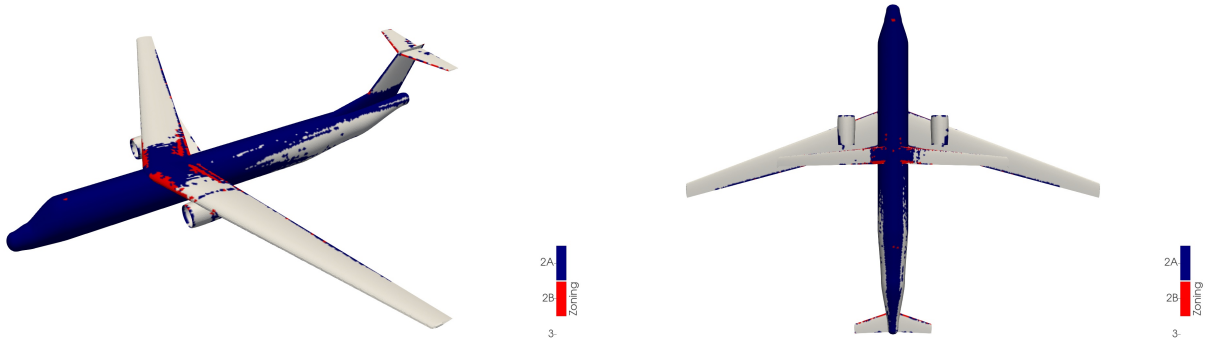


Figure 4.19: Truss-braced wing simulated zoning result, considering only attachment at the nose.

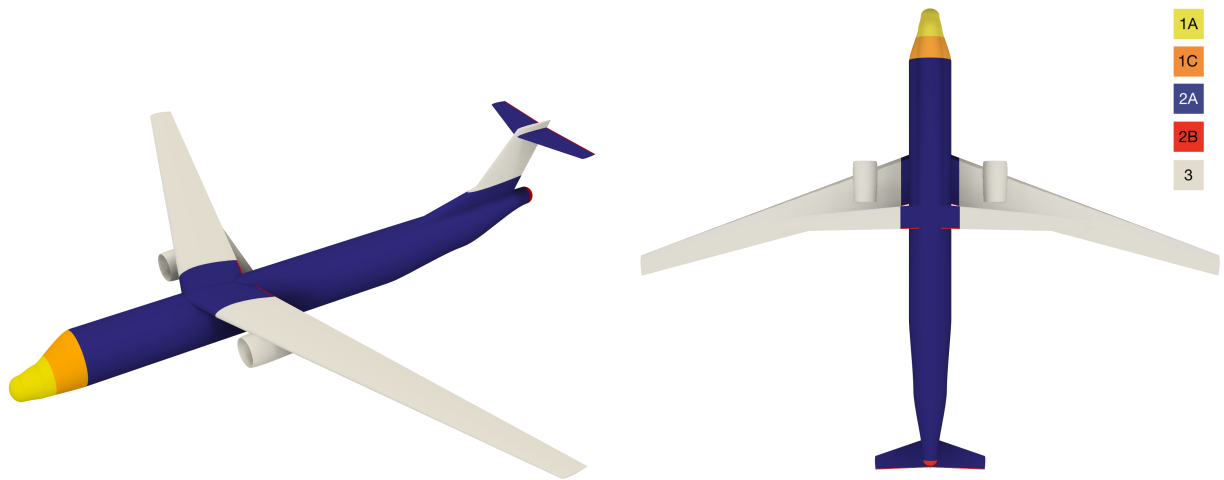


Figure 4.20: Truss-braced wing zoning result using aerospace recommended practices [26], considering only attachment at the nose.

Chapter 5

Conclusions

This thesis has presented a physics-based model for the lightning swept stroke and an engineering mapping to translate results into lightning zones. Verification and validation has been conducted and the model has been applied to conventional and unconventional aircraft. The results of this work demonstrate that the proposed model is a useful engineering tool which can be applied to arbitrary aircraft geometries.

Verification has shown that the numerical implementation successfully resolves the physical model, provided a sufficiently small time step and large number of points are used to resolve the arc. This is evidenced in section 3.5, where the accuracy of the simulation results is also quantified.

Data from the NASA Storm Hazards Program proved pivotal in validating the proposed physics-based model. The validity of an inviscid fluid model for predicting the distribution of many thousands of lightning arcs has been demonstrated. Limitations of the physical and numerical model have been identified, including the failure of the model to resolve geometric enhancement of the electric field.

The sensitivity of the model to several key parameters has been evaluated and, in all cases, found to be more significant than the model accuracy quantified in section 3.5. The aircraft orientation is found to most significantly impact results. Since many lightning strikes occur during climb and descent when pitch angles are greater, the pitch of the aircraft should be considered closely when evaluating a zoning result.

The ability of the proposed model to predict which regions of an aircraft will experience the most swept stroke attachment has been validated using aggregated data from the SHP. This builds confidence for using simulation results to describe lightning zones.

A simple, physically understandable, approach to zoning has been shown to perform very similar to the current state-of-the-art when applied to a conventional commercial aircraft. The simulation-based zoning appears to be slightly more conservative than the aerospace recommended practice, although results are dependent on the initial condition and the choice of mapping thresholds.

The model was applied to two unconventional aircraft, successfully demonstrating zoning results which current recommended practices cannot achieve. Critically, the ARP under-predicts the swept stroke (zone 2A) region over a blended wing body. The ARP does seem to predict a mapping which is nearly correct for the truss-braced wing, although over-predicts the swept stroke (zone 2A) region on the fuselage aft of the truss.

5.1 Future Work

This work has identified several avenues for further exploration;

1. **Development of a complete physics-based zoning tool for engineers.** Combining the initial attachment point model by Austin [40] with this swept stroke model and an automated CFD code could enable automatic zoning of arbitrary aircraft geometries. This would be a valuable tool to the designers of novel aircraft.
2. **Development of a complete physics-based zoning tool for certification.** Collaboration with manufacturers and regulators, along with more verification and validation, could enable this model to be used for aircraft zoning as part of the certification process.
3. **Computational investigation of small-scale swept stroke mechanisms.** Model parameters such as the arc radius and electric field values are selected based on relatively limited data. Confidence in this model's results could be improved by using higher-fidelity simulations of the swept stroke to inform parameter selection.
4. **Experimental investigation of swept stroke mechanisms.** An experimental campaign is currently underway at MIT to explore the behavior of the lightning swept stroke. This is likely to provide valuable insights into the physics and driving mechanisms behind the swept stroke. Data from this campaign could also further validate the proposed model.

Appendix A

2D Gaussian Distribution

A mapping of a uniform Gaussian (normal) distribution to a 2D surface was needed to define the set of initial arc attachment points in section 3.2.

A.1 The Multivariate Gaussian Distribution

The univariate and bivariate Gaussian distribution Probability Density Functions (PDFs) are given in equations A.1 and A.2 respectively. These are plotted next to each other, assuming a mean $\mu = 0.0$ and standard deviation σ in both directions (x and y), in figure A.1. The univariate distribution is scaled by $\frac{1}{\sqrt{2\pi}}$ to account for the reduction in maximum probability when the distribution is extended into two dimensions. It is clear that the 2D distribution can be created by revolving the 1D distribution about the mean, if and only if the standard deviation of the 2D distribution is the same in both directions. The assumption is also made that the correlation, ρ , between x and y is zero, which holds true for this particular application of the Gaussian distribution. By defining $r = \sqrt{(x - \mu_x)^2 + (y - \mu_y)^2}$, which is the distance from the initial attachment point, it can be shown that the 2D distribution depends only on r.

$$P(x) = \frac{1}{\sqrt{2\pi}\sigma^2} e^{-\frac{(x-\mu)^2}{2\sigma^2}} \quad (\text{A.1})$$

$$\begin{aligned} P(x, y) &= \frac{1}{2\pi\sigma_1\sigma_2\sqrt{1-\rho^2}} \exp\left(-\frac{1}{2(1-\rho^2)} \left[\frac{(x-\mu_x)^2}{\sigma_x^2} - 2\rho \frac{(x-\mu_x)(y-\mu_y)}{\sigma_x\sigma_y} + \frac{(y-\mu_y)^2}{\sigma_y^2} \right] \right) \\ &= \frac{1}{2\pi\sigma^2} \exp\left(-\frac{(x-\mu_x)^2 + (y-\mu_y)^2}{2\sigma^2}\right) \text{ for } \sigma = \sigma_x = \sigma_y \text{ and } \rho = 0 \\ &= \frac{1}{2\pi\sigma^2} e^{-\frac{r^2}{2\sigma^2}} \text{ for } r = \sqrt{(x - \mu_x)^2 + (y - \mu_y)^2} \\ &= \frac{1}{\sqrt{2\pi}\sigma^2} P(r) \text{ where } \mu_r = 0 \end{aligned} \quad (\text{A.2})$$

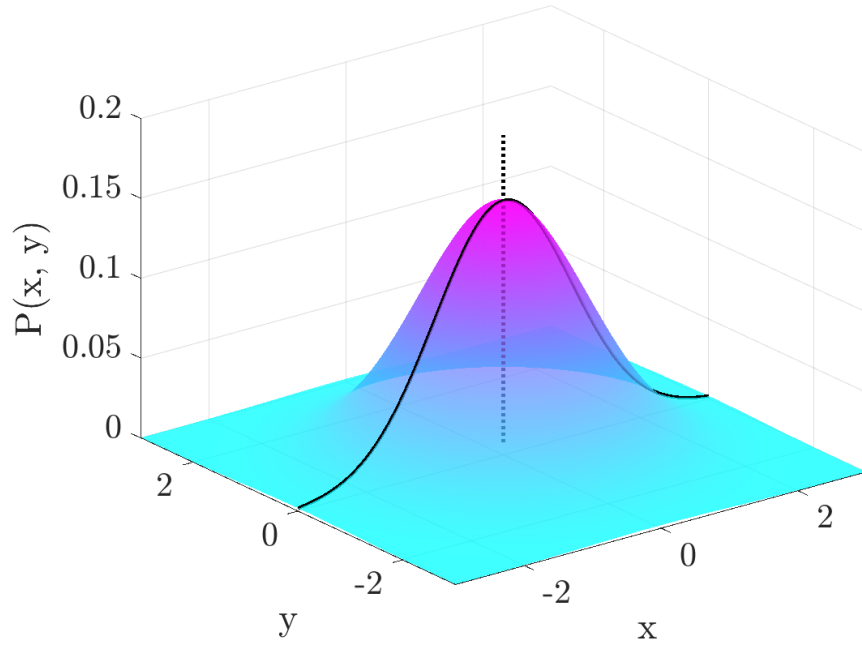


Figure A.1: Uniform bivariate Gaussian distribution and univariate distribution scaled by $\frac{1}{\sqrt{2\pi}}$.

A.2 Mapping to an Arbitrary Surface

Mapping this distribution to a sample of points on an arbitrary surface is not particularly complex, given a defined ‘mean’ point and distance σ . The ‘mean’ μ_x and μ_y correspond to the coordinates of the initial attachment point in the parameterized 2D coordinate system of the surface. A nuance to this mapping is that the distribution will ‘wrap’ around surfaces with a circumference smaller than the 3σ distance. This impacts the definition of the initial condition for the F-106B case (although not in a particularly significant manner), as visualized in section 4.1.

Appendix B

Normalization of Swept Stroke Surface Data

Section 3.3 explains how metrics relating to the aggregate of many arcs require normalization to filter out the effects of mesh size on results. The cell size can vary significantly over the surface of a CFD mesh, so it is important that this is conducted correctly. By inspecting three different approaches to normalization for each metric, the preferred implementation has been selected and verified.

B.1 Probability Distribution

The probability distribution is calculated based on the fraction of all simulated arcs which pass through each cell. Within each cell, the time the arc spends within the cell has no impact on the probability, only the presence of the arc at some point during the simulation. This metric must be normalized by the **cell width**, which is estimated using the square root of the cell area because the model can process unstructured grids with cells of many shapes.

Normalizing the probability distribution per unit length can be justified by considering the probability of an arc passing through a fluid equipotential (equipotentials are normal to streamlines). Assuming arcs are swept smoothly (ignoring jumping), the sum of the attachment probability along any equipotential must equal 1 (i.e. all arcs will cross the equipotential once, assuming the flowfield is somewhat uniform). When the probability is expressed *per unit length*, this can be shown using the line integral in equation B.1, where $p(s)$ is the probability per unit length of the arc passing that equipotential at point s .

$$\oint_{\text{equipotential A}} p(s)ds = \oint_{\text{equipotential B}} p(s)ds = 1.0 \quad (\text{B.1})$$

Normalization by cell length can be further verified by considering the swept stroke in a simple example of a structured CFD grid, shown in figure B.2. For each normalization approach, the diagram on the left illustrates a mesh with cells twice as large as the mesh on the right. This makes it clear that the probability distribution is only independent of cell size when normalized by cell length. The values in figure B.2 show the number of arcs passing through each cell, divided by the specified normalization quantity.

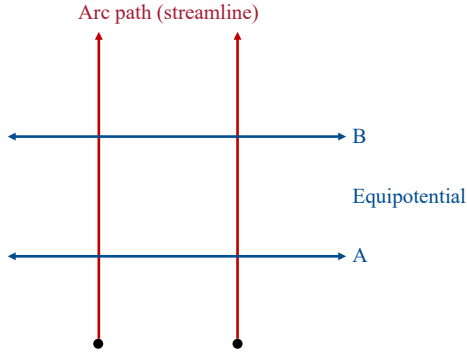


Figure B.1: Sweeping of arcs past lines of equipotential.

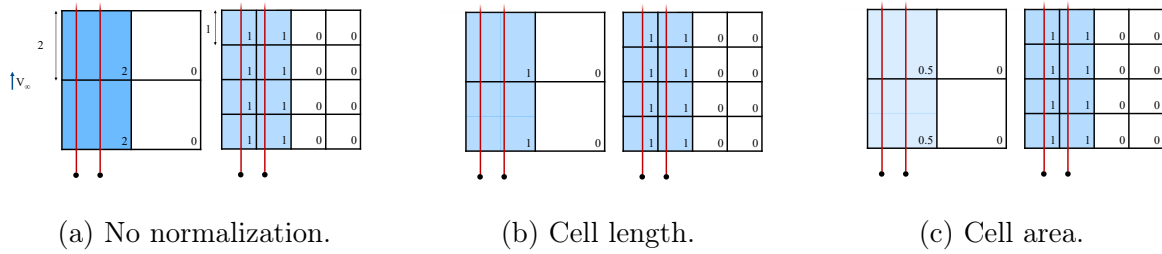


Figure B.2: Probability distribution normalization methods.

B.2 Time Integrals

Time-dependent quantities include dwell time, charge delivery, and action integral, as described in section 3.3.2. These must be normalized by **cell area** and not cell width, because the time the arc spends within the cell does impact the metric. This is illustrated in figure B.3, where the swept stroke moves at a constant rate of 1 unit per second, and the values in each cell represent the dwell time within that cell divided by the normalization metric.

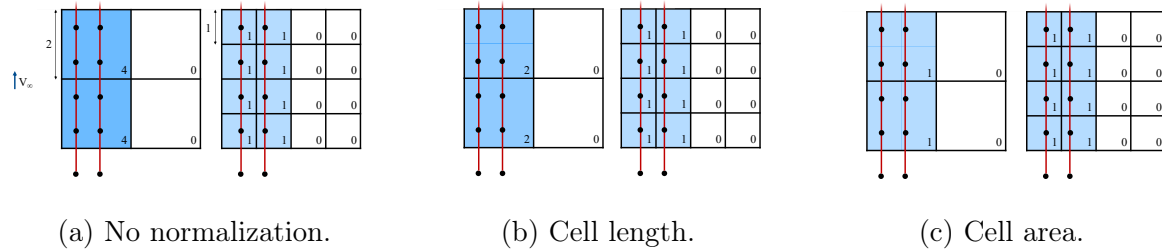


Figure B.3: Normalization methods for time-integrated metrics.

Appendix C

Computational Fluid Dynamics Parameters

Since this work does not primarily focus on Computational Fluid Dynamics (CFD), the decisions and parameters relating to fluid simulations are not explained in detail in the main body of the report. Care was taken to ensure results were as accurate and robust as possible, following industry best practices [94], [110].

C.1 Viscous Simulations: Flow360

The Flow360 solver is well-validated for aircraft test cases [97], [105], [142]. The parameters used for the F-106B simulation are listed in table C.1. Flow360 uses a node-centered, unstructured, 2nd-order, finite-volume solver. A MUSCL extrapolation allows discretization schemes to achieve higher spatial orders of accuracy and the Spalart-Allmaras turbulence model was used for the simulations in this work. Information on the meaning of all of the parameters in table C.1 is available in Flow360 Documentation [142]. Solver parameters were based on the advice of Qiqi Wang, who co-leads the Flow360 team alongside Phillippe Spalart (of the Spalart-Allmaras model).

Table C.1: Flow360 CFD parameters

Mesh	
Refinement Factor	1
First Layer Thickness	0.00001 m
Growth Rate	1.2
Gap Treatment Strength	0
Solvers	
Transience	Steady-state
Turbulence	Spalart-Allmaras (SA)
SA Rotation Correction	Off
Convective Flux Scheme	Roe Reimann
Viscous Flux Scheme	Central Differencing
MUSCL Scheme	2 nd Order Upwind ($\kappa=-1$)
Spatial Discretization	2 nd Order
Conjugate Heat Solver	Off
Aeroacoustics	Off
Output Format	Paraview
Solver Parameters	
Maximum iterations	5000
Initial CFL	1.0
Maximum CFL	100.0
CFL Ramp Steps	1000
NS Solver Tolerance	1e-9
NS Solver Linear Iterations	35
SA Solver Tolerance	1e-8
SA Solver Linear Iterations	25

C.2 Inviscid Simulations: SU2

The SU2 solver is also well-validated for flows over aircraft [107] and was used in this work to compute inviscid flowfields. Documentation was used to understand and select appropriate models and parameters [143], which are outlined in table C.2. Mesh generation was conducted using Gmsh [109].

C.2.1 Mesh Generation: Gmsh

The computational domain for the inviscid simulations of the F-106B aircraft is illustrated in figure C.1, which also shows the rectangular mesh refinement region. Table C.3 shows the Gmsh parameters used to generate the CFD mesh for this test case, where field F1 corresponds to the box region in figure C.1. By default, Gmsh uses the Delaunay triangulation algorithm to generate a 3D tetrahedral mesh [109].

Table C.2: SU2 CFD parameters

Solvers	
Solver	Euler
Math Problem	Direct
Fluid Model	Standard Air
Spatial Gradients	Weighted Least Squares
Linear Solver	FGMRES
Linear Solver Preconditioner	Incomplete LU
Convective Flux Scheme	Jameson-Schmidt-Turkel
Time Discretization	Euler Implicit
Convergence Parameter	Surface Mach (Cauchy Series)
Solver Parameters	
Maximum Iterations	9999
CFL (Finest Grid)	25.0
Adaptive CFL	(0.1, 2.0, 25.0, 1e10)
Runge-Kutta Coefficients	(0.66667, 0.66667, 1.000000)
Linear Solver Error	1e-6
Linear Solver Iterations	10
JST Coefficients	(0.5, 0.02)
Convergence Cauchy Elements	50
Convergence Cauchy Epsilon	1e-10

Table C.3: Gmsh mesh generation parameters

Mesh Size Field	F1*(F2+15)
Box (F1) VIn	2
Box (F1) VOut	10
Box (F1) Thickness	200 mm
Distance (F2) Sampling	20

C.3 Inviscid Simulations: StarCCM+

StarCCM+ is an industrial CFD code built on an unstructured finite volume solver. The parameters used for inviscid simulations in this code are outlined in table C.4

C.3.1 Mesh Generation: StarCCM+

The mesh generation parameters are outlined in table C.5 and the resulting mesh is illustrated in figure 4.15 in section 4.3. When simulating the truss-braced wing using StarCCM+, additional refinement factors were applied to ensure the truss structure was properly resolved; a base size of 200 m was used for the TBW.

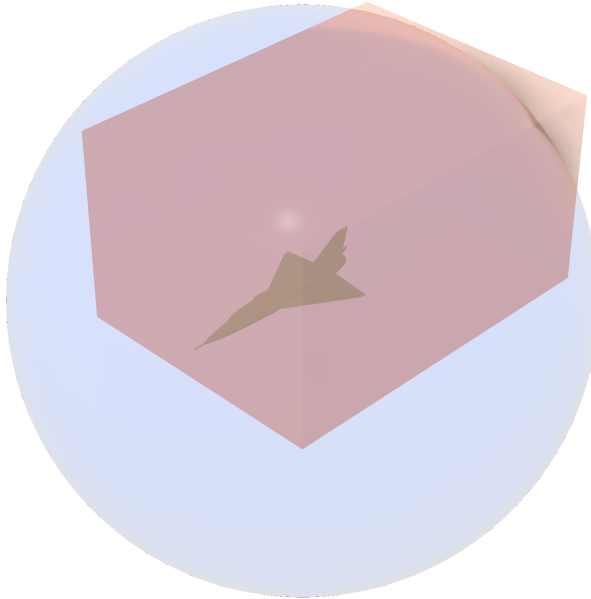


Figure C.1: Gmsh mesh generation domain and refinement region.

Table C.4: StarCCM+ CFD parameters

Solvers	
Fluid	Gas
Transience	Steady
Flow Solver	Coupled (density-based)
Coupled Integration	Implicit
Coupled Discretization	2 nd Order
Coupled Scheme	Weiss-Smith Preconditioned Roe
Density	Constant
Gradient Limiter	Venkatakrishnan
Linear Solver	AMG
Solver Parameters	
CFL Control	Automatic
Initial CFL	1.0
Minimum CFL	0.1
Maximum CFL	100000.0
Coupled Solver Relaxation	0.3

Table C.5: StarCCM+ mesh generation parameters (blended wing body)

Meshers		
Core Volume	Tetrahedral	
Surface	Surface Remesher	
Surface Remesher		
Mesher Method	Triangle	
Curvature Refinement	On	
Curvature Pts/Circle	36	
Proximity Refinement	On	
Proximity Pts in Gap	2.0	
Surface Growth Rate	1.2	
Compatibility Refinement	Off	
Aligned Meshing	On	
Tetrahedral Mesh		
Base Size	150.0 m	
CAD Projection	On	
Target Surface Size	100% Base	
Minimum Surface Size	0.1% Base	
Volume Growth Rate	1.1	
Maximum Tet Size	10000% Base	
Core Mesh Optimization Cycles	1	
Quality Threshold	0.4	
Aircraft Surface Refinement		
Target Surface Size	0.15 m	

References

- [1] B. Fisher, R. Taeuber, and K. Crouch, “Implications of a recent lightning strike to a NASA jet trainer,” en, in *26th Aerospace Sciences Meeting*, Reno,NV,U.S.A.: American Institute of Aeronautics and Astronautics, Jan. 1988. DOI: [10.2514/6.1988-394](https://arc.aiaa.org/doi/10.2514/6.1988-394). [Online]. Available: <https://arc.aiaa.org/doi/10.2514/6.1988-394> (visited on 04/05/2024).
- [2] V. A. Rakov and M. A. Uman, *Lightning: physics and effects*. Cambridge, U.K. ; New York: Cambridge University Press, 2003, ISBN: 978-0-521-58327-5.
- [3] B. Prentice, A. DiNota, N. Dulac, L. Hayes, I. Ferguson, D. Holden, U. Mishra, and R. Huang, “Global Fleet and MRO Market Forecast,” Oliver Wyman, Tech. Rep., 2023. [Online]. Available: <https://www.oliverwyman.com/content/dam/oliver-wyman/v2/publications/2024/feb/OliverWyman-Global-Fleet-and-MRO-Market-Forecast-2024-2034.pdf>.
- [4] C. T. R. Wilson, “III. Investigations on lighting discharges and on the electric field of thunderstorms,” en, *Philosophical Transactions of the Royal Society of London. Series A, Containing Papers of a Mathematical or Physical Character*, vol. 221, no. 582-593, pp. 73–115, Jan. 1921, ISSN: 0264-3952, 2053-9258. DOI: [10.1098/rsta.1921.0003](https://royalsocietypublishing.org/doi/10.1098/rsta.1921.0003). [Online]. Available: <https://royalsocietypublishing.org/doi/10.1098/rsta.1921.0003> (visited on 04/05/2024).
- [5] V. Karlos, G. Solomos, and B. Viaccoz, *Calculation of blast loads for application to structural components*, eng. Luxembourg: Publications Office, 2013, OCLC: 903492886, ISBN: 978-92-79-35158-7.
- [6] A. Barnett, “Aviation Safety: A Whole New World?” en, *Transportation Science*, vol. 54, no. 1, pp. 84–96, Jan. 2020, ISSN: 0041-1655, 1526-5447. DOI: [10.1287/trsc.2019.0937](https://pubsonline.informs.org/doi/10.1287/trsc.2019.0937). [Online]. Available: <https://pubsonline.informs.org/doi/10.1287/trsc.2019.0937> (visited on 04/05/2024).
- [7] M. Cherington and K. Mathys, “Deaths and injuries as a result of lightning strikes to aircraft,” eng, *Aviation, Space, and Environmental Medicine*, vol. 66, no. 7, pp. 687–689, Jul. 1995, ISSN: 0095-6562.
- [8] C. Guerra-Garcia, “The Role of Low Temperature Plasma Research in Designing the Lightning and Precipitation Static Protection of Novel Aircraft,” en, *IEEE Transactions on Plasma Science*, vol. 51, no. 4, pp. 965–979, Apr. 2023, ISSN:

- 0093-3813, 1939-9375. DOI: [10.1109/TPS.2022.3209933](https://doi.org/10.1109/TPS.2022.3209933). [Online]. Available: <https://ieeexplore.ieee.org/document/9916641/> (visited on 04/05/2024).
- [9] R. Rothfeld, A. Straubinger, M. Fu, C. Al Haddad, and C. Antoniou, “Urban air mobility,” en, in *Demand for Emerging Transportation Systems*, Elsevier, 2020, pp. 267–284, ISBN: 978-0-12-815018-4. DOI: [10.1016/B978-0-12-815018-4.00013-9](https://doi.org/10.1016/B978-0-12-815018-4.00013-9). [Online]. Available: <https://linkinghub.elsevier.com/retrieve/pii/B9780128150184000139> (visited on 04/06/2024).
- [10] G. V. Kursell, “Airbus Lays the Foundations for Future Urban Air Mobility with the Air Mobility Initiative,” May 2024. [Online]. Available: https://www.google.com/url?sa=t&source=web&rct=j&opi=89978449&url=https://www.airbus.com/en/newsroom/press-releases/2022-05-airbus-lays-the-foundations-for-future-urban-air-mobility-in&ved=2ahUKEwjnpt-24q2FAxW1LFkFHcxtCGcQFnoECBUQAQ&usg=AOvVaw1tCJ9DqveuGKs_XDsg5meY.
- [11] P. Wilson, “Bringing the Urban Air Mobility Market to Life,” en,
- [12] The Boeing Company and Wisk, “Concept of Operations for Uncrewed Urban Air Mobility,” Tech. Rep., 2023. [Online]. Available: <https://www.google.com/url?sa=t&source=web&rct=j&opi=89978449&url=https://www.boeing.com/content/dam/boeing/boeingdotcom/innovation/con-ops/docs/Concept-of-Operations-for-Uncrewed-Urban-Air-Mobility.pdf&ved=2ahUKEwjVtYSA4q2FAxX6C3kGHZnqC1cQFnoECBEQAQ&usg=AOvVaw3exvVbh-8SaA90jJKf6171>.
- [13] J. Pons-Prats, T. Živojinović, and J. Kuljanin, “On the understanding of the current status of urban air mobility development and its future prospects: Commuting in a flying vehicle as a new paradigm,” en, *Transportation Research Part E: Logistics and Transportation Review*, vol. 166, p. 102 868, Oct. 2022, ISSN: 13665545. DOI: [10.1016/j.tre.2022.102868](https://doi.org/10.1016/j.tre.2022.102868). [Online]. Available: <https://linkinghub.elsevier.com/retrieve/pii/S1366554522002496> (visited on 04/06/2024).
- [14] E. Ordoukhalian and A. M. Madni, “Blended Wing Body Architecting and Design: Current Status and Future Prospects,” en, *Procedia Computer Science*, vol. 28, pp. 619–625, 2014, ISSN: 18770509. DOI: [10.1016/j.procs.2014.03.075](https://doi.org/10.1016/j.procs.2014.03.075). [Online]. Available: <https://linkinghub.elsevier.com/retrieve/pii/S1877050914001380> (visited on 04/06/2024).
- [15] P. Okonkwo and H. Smith, “Review of evolving trends in blended wing body aircraft design,” en, *Progress in Aerospace Sciences*, vol. 82, pp. 1–23, Apr. 2016, ISSN: 03760421. DOI: [10.1016/j.paerosci.2015.12.002](https://doi.org/10.1016/j.paerosci.2015.12.002). [Online]. Available: <https://linkinghub.elsevier.com/retrieve/pii/S0376042115300336> (visited on 04/06/2024).

- [16] B. I. Larrimer, *Beyond tube-and-wing: the X-48 blended wing-body and NASA's quest to reshape future transport aircraft* (NASA aeronautics book series). Washington, DC: NASA, 2020, ISBN: 978-1-62683-059-2.
- [17] J. Loughban, "News - Briefing. Airbus blends body and wing in unique aircraft design," en, *Engineering & Technology*, vol. 15, no. 2, pp. 11–11, Mar. 2020, ISSN: 1750-9637, 1750-9645. DOI: [10.1049/et.2020.0200](https://doi.org/10.1049/et.2020.0200). [Online]. Available: <https://digital-library.theiet.org/content/journals/10.1049/et.2020.0200> (visited on 04/06/2024).
- [18] JetZero, "JetZero Unveils Ultra-Efficient Blended Wing Body Aircraft for the Airline Middle Market," Apr. 2023. [Online]. Available: <https://20607413.fs1.hubspotusercontent-na1.net/hubfs/20607413/JetZero%20Unveils%20BWB%20Aircraft-1.pdf>.
- [19] M. Goldenshteyn, "X-66A Bracing for the Next Big Wing," *Boeing Innovation Quarterly*, vol. 7, no. 26, pp. 10–22, 2023. [Online]. Available: https://www.boeing.com/content/dam/boeing/boeingdotcom/features/innovation-quarterly/2023/11/X-66A_Q4_2023.pdf.
- [20] C. A. O'Shea, *Next Generation Experimental Aircraft Becomes NASA's Newest X-Plane*, Jun. 2023. [Online]. Available: <https://www.nasa.gov/news-release/next-generation-experimental-aircraft-becomes-nasas-newest-x-plane/>.
- [21] Airbus, *Hybrid and electric flight*, 2024. [Online]. Available: <https://www.airbus.com/en/innovation/low-carbon-aviation/hybrid-and-electric-flight>.
- [22] K. V. Papathakis, K. J. Kloesel, Y. Lin, S. C. Clarke, J. J. Ediger, and S. R. Ginn, "NASA Turbo-electric Distributed Propulsion Bench," en, in *52nd AIAA/SAE/ASEE Joint Propulsion Conference*, Salt Lake City, UT: American Institute of Aeronautics and Astronautics, Jul. 2016, ISBN: 978-1-62410-406-0. DOI: [10.2514/6.2016-4611](https://arc.aiaa.org/doi/10.2514/6.2016-4611). [Online]. Available: <http://arc.aiaa.org/doi/10.2514/6.2016-4611> (visited on 04/06/2024).
- [23] NASA, "NASA Aeronautics Strategic Implementation Plan 2023," en, 2023. [Online]. Available: <https://www.nasa.gov/directorates/armd/armd-strategic-implementation-plan/>.
- [24] Rolls Royce, *Pioneering Electrification*, 2024. [Online]. Available: <https://www.rolls-royce.com/products-and-services/electrical.aspx>.
- [25] *Aircraft Lightning Environment and Related Test Waveforms*, Aerospace Recommended Practise, Jan. 2013. [Online]. Available: <https://www.sae.org/standards/content/arp5412b/>.
- [26] *Aircraft Lightning Zone*, Aerospace Recommended Practise, Dec. 2018. [Online]. Available: <https://www.sae.org/standards/content/arp5414b/>.
- [27] *Aircraft Lightning Test Methods*, Aerospace Recommended Practise, Mar. 2005. [Online]. Available: <https://www.sae.org/standards/content/arp5416/>.

- [28] I. Gallimberti, G. Bacchiega, A. Bondiou-Clergerie, and P. Lalande, “Fundamental processes in long air gap discharges,” en, *Comptes Rendus. Physique*, vol. 3, no. 10, pp. 1335–1359, Nov. 2002, ISSN: 1878-1535. DOI: [10.1016/S1631-0705\(02\)01414-7](https://doi.org/10.1016/S1631-0705(02)01414-7). [Online]. Available: [https://comptes-rendus.academie-sciences.fr/physique/articles/10.1016/S1631-0705\(02\)01414-7/](https://comptes-rendus.academie-sciences.fr/physique/articles/10.1016/S1631-0705(02)01414-7/) (visited on 04/06/2024).
- [29] H. Zaglauer and W. Wulbrand, “A simplified model for the determination of initial attachment zones via electric field modeling - Parameter studies and comparisons,” in *Proceedings from the International Conference on Lightning and Static Electricity (ICOLSE)*, Jan. 1999, p. 6.
- [30] P. Lalande, A. Bondiou-Clergerie, and P. Laroche, “Analysis of available in-flight measurements of lightning strikes to aircraft,” in *Proceedings from the International Conference on Lightning and Static Electricity (ICOLSE)*, Jan. 1999, p. 8.
- [31] P. Lalande and A. Delannoy, “Numerical Methods for Zoning Computation,” en, *AerospaceLab Journal*, no. 5, Dec. 2012.
- [32] I. Gallimberti, “The mechanism of the long spark formation,” *Le Journal de Physique Colloques*, vol. 40, no. C7, pp. C7–193–C7–250, Jul. 1979, ISSN: 0449-1947. DOI: [10.1051/jphyscol:19797440](https://doi.org/10.1051/jphyscol:19797440). [Online]. Available: <http://www.edpsciences.org/10.1051/jphyscol:19797440> (visited on 04/06/2024).
- [33] Les Renardières, “Positive discharges in long air gaps at Les Renardières - 1975 results and conclusions,” *Electra*, vol. 53, 1977.
- [34] Les Renardières, “Research on long air gap discharges at Les Renardières,” *Electra*, vol. 23, pp. 53–157, 1972.
- [35] Les Renardières, “Research on long air gap discharges at Les Renardières,” *Electra*, vol. 35, 1973.
- [36] A. Larsson, P. Lalande, A. Bondiou-Clergerie, and P. Lalande, “The lightning swept stroke along an aircraft in flight. Part II: Numerical simulations of the complete process,” en, *Journal of Physics D: Applied Physics*, vol. 33, no. 15, pp. 1876–1883, Aug. 2000, ISSN: 0022-3727, 1361-6463. DOI: [10.1088/0022-3727/33/15/318](https://doi.org/10.1088/0022-3727/33/15/318). [Online]. Available: <https://iopscience.iop.org/article/10.1088/0022-3727/33/15/318> (visited on 04/05/2024).
- [37] A. Larsson, P. Lalande, A. Bondiou-Clergerie, P. Lalande, and A. Delannoy, “The lightning swept stroke along an aircraft in flight. Part I: Thermodynamic and electric properties of lightning arc channels,” en, *Journal of Physics D: Applied Physics*, vol. 33, no. 15, pp. 1866–1875, Aug. 2000, ISSN: 0022-3727, 1361-6463. DOI: [10.1088/0022-3727/33/15/317](https://doi.org/10.1088/0022-3727/33/15/317). [Online]. Available: <https://iopscience.iop.org/article/10.1088/0022-3727/33/15/317> (visited on 04/05/2024).

- [38] S. P. Austin, C. Guerra-Garcia, and J. Peraire, “Computational Zoning of Unconventional Aircraft,” en, in *International Conference On Lightning and Static Electricity (ICOLSE)*, Madrid, Spain, Oct. 2022. DOI: [10.5281/zenodo.7155576](https://doi.org/10.5281/zenodo.7155576). [Online]. Available: <https://zenodo.org/doi/10.5281/zenodo.7155575>.
- [39] C. Guerra-Garcia, N. C. Nguyen, J. Peraire, and M. Martinez-Sanchez, “Arc reattachment driven by a turbulent boundary layer: Implications for the sweeping of lightning arcs along aircraft,” en, *Journal of Physics D: Applied Physics*, vol. 49, no. 37, p. 375204, Sep. 2016, ISSN: 0022-3727, 1361-6463. DOI: [10.1088/0022-3727/49/37/375204](https://doi.org/10.1088/0022-3727/49/37/375204). [Online]. Available: <https://iopscience.iop.org/article/10.1088/0022-3727/49/37/375204> (visited on 04/05/2024).
- [40] S. P. Austin, “Computational Zoning Assessment of Unconventional Aircraft,” en, SM Thesis, Massachusetts Institute of Technology, Boston, USA, May 2022.
- [41] B. D. Fisher and J. A. Plumer, “Lightning attachment patterns and flight conditions experienced by the NASA F-106B airplane from 1980 to 1983,” en, in *22nd Aerospace Sciences Meeting*, Reno,NV,U.S.A.: American Institute of Aeronautics and Astronautics, Jan. 1984. DOI: [10.2514/6.1984-466](https://doi.org/10.2514/6.1984-466). [Online]. Available: <https://arc.aiaa.org/doi/10.2514/6.1984-466> (visited on 04/05/2024).
- [42] B. D. Fisher, P. W. Brown, J. A. Plumer, and L. C. A. J. Wunschel Jr, “Final Results of the NASA Storm Hazards Program,” en, in *International Conference On Lightning and Static Electricity (ICOLSE)*, Oklahoma City, Oklahoma, Apr. 1988.
- [43] H. W. Kazemir, “Current budget of the atmospheric electric global circuit,” en, *Journal of Geophysical Research: Atmospheres*, vol. 99, no. D5, pp. 10 701–10 708, May 1994, ISSN: 0148-0227. DOI: [10.1029/93JD02616](https://doi.org/10.1029/93JD02616). [Online]. Available: <https://agupubs.onlinelibrary.wiley.com/doi/10.1029/93JD02616> (visited on 04/06/2024).
- [44] NOAA, *Thunderstorms*, Apr. 2023. [Online]. Available: <https://www.noaa.gov/jetstream/thunderstorms#:~:text=It%20is%20estimated%20that%20there,astounding%2014.6%20million%20occurrences%20annually!>
- [45] V. Cooray, Ed., *The lightning flash* (IET power and energy series 69), Second edition. London: Institution of Engineering and Technology, 2014, OCLC: ocn868083545, ISBN: 978-1-84919-691-8.
- [46] R. Jayaratne, “Thunderstorm Electrification Mechanisms,” in *The Lightning Flash*, ser. IET Power and Energy Series 69, 2nd ed., London: Institution of Engineering and Technology, 2014, pp. 15–39, ISBN: 978-1-84919-691-8.
- [47] S. A. Prentice and D. Mackerras, “The Ratio of Cloud to Cloud-Ground Lightning Flashes in Thunderstorms,” en, *Journal of Applied Meteorology*, vol. 16, no. 5, pp. 545–550, May 1977, ISSN: 0021-8952. DOI: [10.1175/1520-0450\(1977\)016<0545:TROCTC>2.0.CO;2](https://doi.org/10.1175/1520-0450(1977)016<0545:TROCTC>2.0.CO;2). [Online]. Available: [http://journals.ametsoc.org/doi/10.1175/1520-0450\(1977\)016%3C0545:TROCTC%3E2.0.CO;2](http://journals.ametsoc.org/doi/10.1175/1520-0450(1977)016%3C0545:TROCTC%3E2.0.CO;2) (visited on 04/06/2024).

- [48] J.-P. Moreau, J.-C. Alliot, and V. Mazur, “Aircraft lightning initiation and interception from in situ electric measurements and fast video observations,” en, *Journal of Geophysical Research: Atmospheres*, vol. 97, no. D14, pp. 15 903–15 912, Oct. 1992, ISSN: 0148-0227. DOI: [10.1029/92JD01077](https://doi.org/10.1029/92JD01077). [Online]. Available: <https://agupubs.onlinelibrary.wiley.com/doi/10.1029/92JD01077> (visited on 04/06/2024).
- [49] V. Mazur, “A physical model of lightning initiation on aircraft in thunderstorms,” en, *Journal of Geophysical Research: Atmospheres*, vol. 94, no. D3, pp. 3326–3340, Mar. 1989, ISSN: 0148-0227. DOI: [10.1029/JD094iD03p03326](https://doi.org/10.1029/JD094iD03p03326). [Online]. Available: <https://agupubs.onlinelibrary.wiley.com/doi/10.1029/JD094iD03p03326> (visited on 04/06/2024).
- [50] C. Guerra-Garcia, N. C. Nguyen, J. Peraire, and M. Martinez-Sanchez, “Charge Control Strategy for Aircraft-Triggered Lightning Strike Risk Reduction,” en, *AIAA Journal*, vol. 56, no. 5, pp. 1988–2002, May 2018, ISSN: 0001-1452, 1533-385X. DOI: [10.2514/1.J056406](https://doi.org/10.2514/1.J056406). [Online]. Available: <https://arc.aiaa.org/doi/10.2514/1.J056406> (visited on 05/09/2024).
- [51] K. Berger, “Novel observations on lightning discharges: Results of research on Mount San Salvatore,” en, *Journal of the Franklin Institute*, vol. 283, no. 6, pp. 478–525, Jun. 1967, ISSN: 00160032. DOI: [10.1016/0016-0032\(67\)90598-4](https://doi.org/10.1016/0016-0032(67)90598-4). [Online]. Available: <https://linkinghub.elsevier.com/retrieve/pii/0016003267905984> (visited on 04/06/2024).
- [52] R. Thottappillil, V. A. Rakov, M. A. Uman, W. H. Beasley, M. J. Master, and D. V. Shelukhin, “Lightning subsequent-stroke electric field peak greater than the first stroke peak and multiple ground terminations,” en, *Journal of Geophysical Research: Atmospheres*, vol. 97, no. D7, pp. 7503–7509, May 1992, ISSN: 0148-0227. DOI: [10.1029/92JD00557](https://doi.org/10.1029/92JD00557). [Online]. Available: <https://agupubs.onlinelibrary.wiley.com/doi/10.1029/92JD00557> (visited on 04/06/2024).
- [53] The Boeing Company, *Boeing 787 Dreamliner*, 2024. [Online]. Available: <https://www.boeing.com/commercial/787family>.
- [54] O. Memon, *Could The Boeing 787 Dreamliner Fly At Supersonic Speeds?* Dec. 2022. [Online]. Available: <https://simpleflying.com/could-the-boeing-787-dreamliner-fly-at-supersonic-speeds/>.
- [55] L. Tholin, P. Chemartin, and F. Lalande, “Numerical investigation of the surface effects on the dwell time during the sweeping of lightning arcs,” en, in *International Conference On Lightning and Static Electricity (ICOLSE)*, Seattle, USA, Sep. 2013. [Online]. Available: <https://onera.hal.science/hal-01068639>.
- [56] Civil Aeronautics Board, “Pan American World Airways, Inc. Boeing 707-121 N709PA Near Elkton, Maryland December 8, 1963.,” Civil Aeronautics Board, Aircraft Accident Report SA-376 1-0015, Feb. 1965. [Online]. Available: https://reports.aviation-safety.net/1963/19631208-0_B701_N709PA.pdf.

- [57] “Special Investigation Report Wing Failure of Boeing 747-131 Near Madrid, Spain, May 9, 1976,” National Transportation Safety Board, Washington, DC, Aircraft Accident Report NTSB-AAR-78-12, Oct. 1978. [Online]. Available: <https://www.ntsb.gov/investigations/AccidentReports/Reports/AAR7812.pdf>.
- [58] “Die Untersuchung des Flugunfalles mit dem Flugzeug SA 227-AC, Metro 111, D-CABB, am 8. Februar 1988 bei Kettwig,” Aircraft Accident Investigation Unit at the Federal Aviation Office, Germany, Germany, Aircraft Accident Report AZ.: 1 X 0001/88. [Online]. Available: https://www.bfu-web.de/DE/Publikationen/Untersuchungsberichte/BerichteFUS-vor-BFU-Zeiten/Bericht_88_1X001-0.pdf?__blob=publicationFile&v=1.
- [59] T. L. Clark and L. E. Primm, “Lightning Protection Guidelines for Aerospace Vehicles,” NASA Marshall Space Flight Center, Alabama, USA, Tech. Rep. NASA/TM-1999-209734, May 1999. [Online]. Available: <https://ntrs.nasa.gov/api/citations/20000004589/downloads/20000004589.pdf>.
- [60] G. Sweers, B. Birch, and J. Gokcen, “Lightning Strikes: Protection, Inspection, and Repair,” *AERO*, no. 48, 2012. [Online]. Available: https://www.boeing.com/commercial/aeromagazine/articles/2012_q4/pdfs/AERO_2012q4.pdf.
- [61] D. Clark, “Terrifying aftermath of lightning strike on easyJet planes wing that forced landing,” *The Mirror*, Sep. 2022. [Online]. Available: <https://www.mirror.co.uk/news/world-news/terrifying-aftermath-lightning-strike-easyjet-28108882>.
- [62] J. A. Plumer, W. A. Malloy, and J. B. Craft, “The Effects of Lightning on Digital Flight Control Systems,” NASA Technical Paper N76-31176, Aug. 1976, pp. 989–1008. [Online]. Available: <https://ntrs.nasa.gov/api/citations/19760024088/downloads/19760024088.pdf>.
- [63] D. Morgan, C. J. Hardwick, S. J. Haigh, and A. J. Meakins, “Lightning Hazards to Aircraft and Launchers,” en, *AerospaceLab Journal*, no. 5, Dec. 2012. [Online]. Available: https://aerospacelab.onera.fr/sites/default/files/2024-01/AL05-11_0.pdf.
- [64] D. Garretson, H. Mair, C. Martin, K. Sullivan, and J. Teichman, “Review of CFD Capabilities,” Science & Technology Policy Institute, Washington, DC, Tech. Rep. D-3145, Nov. 2005. [Online]. Available: <https://apps.dtic.mil/sti/tr/pdf/ADA537587.pdf>.
- [65] American Society of Mechanical Engineers, Ed., *Standard for verification and validation in computational fluid dynamics and heat transfer: an American national standard* (ASME V&V 20-2009), eng, Reaffirmed 2016. New York, NY: The American Society of Mechanical Engineers, 2009, ISBN: 978-0-7918-3209-7.
- [66] “Guide: Guide for the Verification and Validation of Computational Fluid Dynamics Simulations (AIAA G-077-1998(2002)),” en, in *Guide: Guide for the Verification and Validation of Computational Fluid Dynamics Simulations (AIAA G-077-1998(2002))*, Computational Fluid Dynamics Committee, Ed., Washington, DC: American Institute of Aeronautics and Astronautics, Inc., Jan. 1998, ISBN:

- 978-1-56347-285-5. DOI: [10.2514/4.472855.001](https://doi.org/10.2514/4.472855.001). [Online]. Available: <https://arc.aiaa.org/doi/10.2514/4.472855.001> (visited on 04/13/2024).
- [67] R. L. Harrison, C. Granja, and C. Leroy, “Introduction to Monte Carlo Simulation,” Bratislava (Slovakia), 2010, pp. 17–21. DOI: [10.1063/1.3295638](https://doi.org/10.1063/1.3295638). [Online]. Available: <https://pubs.aip.org/aip/acp/article/1204/1/17-21/866186> (visited on 04/17/2024).
- [68] A. Cunha, R. Nasser, R. Sampaio, H. Lopes, and K. Breitman, “Uncertainty quantification through the Monte Carlo method in a cloud computing setting,” en, *Computer Physics Communications*, vol. 185, no. 5, pp. 1355–1363, May 2014, ISSN: 00104655. DOI: [10.1016/j.cpc.2014.01.006](https://doi.org/10.1016/j.cpc.2014.01.006). [Online]. Available: <https://linkinghub.elsevier.com/retrieve/pii/S0010465514000198> (visited on 04/17/2024).
- [69] M. A. Uman, “Determination of lightning temperature,” en, *Journal of Geophysical Research*, vol. 74, no. 4, pp. 949–957, Feb. 1969, ISSN: 01480227. DOI: [10.1029/JB074i004p00949](https://doi.org/10.1029/JB074i004p00949). [Online]. Available: <http://doi.wiley.com/10.1029/JB074i004p00949> (visited on 04/06/2024).
- [70] A. Bourlet, F. Tholin, J. Labaune, F. Pechereau, A. Vincent-Randonnier, and C. O. Laux, “Numerical model of restrikes in gliding arc discharges,” en, *Plasma Sources Science and Technology*, vol. 33, no. 1, p. 015 010, Jan. 2024, ISSN: 0963-0252, 1361-6595. DOI: [10.1088/1361-6595/ad1b6d](https://doi.org/10.1088/1361-6595/ad1b6d). [Online]. Available: <https://iopscience.iop.org/article/10.1088/1361-6595/ad1b6d> (visited on 04/05/2024).
- [71] A. F. Bublievskii, “An approximate model of an electric arc in transverse mutually perpendicular aerodynamic and magnetic fields,” en, *Journal of Engineering Physics*, vol. 35, no. 6, pp. 1424–1429, Dec. 1978, ISSN: 0022-0841, 1573-871X. DOI: [10.1007/BF01104846](https://doi.org/10.1007/BF01104846). [Online]. Available: <http://link.springer.com/10.1007/BF01104846> (visited on 04/06/2024).
- [72] *Standard Atmosphere*, May 1975. [Online]. Available: <https://www.iso.org/standard/7472.html>.
- [73] V. A. Rakov and M. A. Uman, “Maximum Electric Fields: Implications for Lightning Initiation,” in *Lightning: Physics and Effects*, Cambridge, UK: Cambridge University Press, 2003, p. 82, ISBN: 0 521 58327 6.
- [74] T. An, P. Yuan, G. Liu, J. Cen, X. Wang, M. Zhang, and Y. An, “The radius and temperature distribution along radial direction of lightning plasma channel,” *Physics of Plasmas*, vol. 26, no. 1, p. 013 506, Jan. 2019, ISSN: 1070-664X. DOI: [10.1063/1.5059363](https://doi.org/10.1063/1.5059363).
- [75] R. C. Jones, “Return stroke core diameter,” *Journal of Geophysical Research (1896-1977)*, vol. 73, no. 2, pp. 809–814, 1968. DOI: [10.1029/JB073i002p00809](https://doi.org/10.1029/JB073i002p00809).
- [76] V. A. Rakov and M. A. Uman, “Properties of the return-stroke channel,” in *Lightning: Physics and Effects*, Cambridge, UK: Cambridge University Press, 2003, p. 163, ISBN: 0 521 58327 6.

- [77] В. Л. Грановский, *Электрический ток в газе установившийся ток* (*Electric Current in Gas: Steady Current*), Russian. Moscow: Издательство «наука», 1971.
- [78] Y. P. Raizer, *Gas Discharge Physics*. Germany: Springer-Verlag Heidelberg, 1991, ISBN: 3-540-19462-2.
- [79] L. A. King, “The voltage gradient of the free burning arc in air or nitrogen,” in *Ionization phenomena in gases*, vol. 1, Munich: North-Holland Publishing Company, Sep. 1961, pp. 871–877.
- [80] J. Dobbing and A. Hanson, “A Swept Stroke Experiment With a Rocket Sled,” en, in *1978 IEEE International Symposium on Electromagnetic Compatibility*, Atlanta, GA, USA: IEEE, Jun. 1978, pp. 1–6, ISBN: 978-1-5090-3164-1. DOI: [10.1109/ISEMC.1978.7566889](https://doi.org/10.1109/ISEMC.1978.7566889). [Online]. Available: <https://ieeexplore.ieee.org/document/7566889/> (visited on 04/05/2024).
- [81] A. von Engel, *Ionized Gases*, 2nd ed. London: Oxford University Press, 1965, ISBN: 978-0-19-851914-0.
- [82] P. Lalande, “Etudes des conditions de foudroiement d'une structure au sol,” These de doctorat, Universite d'Orsay, Paris, 1996.
- [83] N. Cianos and E. T. Pierce, “A Ground-Lightning Environment for Engineering Usage,” Stanford Research Institute, California, USA, Tech. Rep. AD907891, Aug. 1972. [Online]. Available: <https://apps.dtic.mil/sti/pdfs/AD0907891.pdf>.
- [84] K. Berger, “Blitzstrom-Parameter von Aufwärtsblitzen,” *Bull. Schweiz. Elektrotech.*, vol. 69, pp. 353–360, 1978.
- [85] F. Fuchs, E. Landers, R. Schmid, and J. Wiesinger, “Lightning current and magnetic field parameters caused by lightning strikes to tall structures relating to interference of electronic systems,” *IEEE Transactions on Electromagnetic Compatibility*, vol. 40, no. 4, pp. 444–451, Nov. 1998, ISSN: 00189375. DOI: [10.1109/15.736205](https://doi.org/10.1109/15.736205). [Online]. Available: <https://ieeexplore.ieee.org/document/736205/> (visited on 04/12/2024).
- [86] Conseil international des grands réseaux électriques, Ed., *Lightning parameters for engineering applications*, eng. Paris: CIGRÉ, 2013, ISBN: 978-2-85873-244-9.
- [87] J. H. Hagenguth and J. G. Anderson, “Lightning to the Empire State Building,” *AIEE Transactions*, vol. 71, no. Part 3, pp. 641–649, 1952.
- [88] B. N. Gorin and A. V. Shkilev, “Measurement of Lightning Currents at the Ostankino Tower,” *Elektrichestvo*, vol. 8, pp. 64–65, 1984.
- [89] K. Berger, R. B. Anderson, and H. Kroninger, “Parameters of Lightning Flashes,” *Electra*, vol. 80, pp. 23–37, 1975.
- [90] R. J. Fisher, G. H. Schnetzer, R. Thottappillil, V. A. Rakov, M. A. Uman, and J. D. Goldberg, “Parameters of triggered-lightning flashes in Florida and Alabama,” en, *Journal of Geophysical Research: Atmospheres*, vol. 98, no. D12, pp. 22 887–22 902, Dec. 1993, ISSN: 0148-0227. DOI: [10.1029/93JD02293](https://doi.org/10.1029/93JD02293). [Online]. Available: <https://agupubs.onlinelibrary.wiley.com/doi/10.1029/93JD02293> (visited on 04/12/2024).

- [91] P. Depasse, “Statistics on artificially triggered lightning,” en, *Journal of Geophysical Research: Atmospheres*, vol. 99, no. D9, pp. 18 515–18 522, Sep. 1994, ISSN: 0148-0227. DOI: [10.1029/94JD00912](https://doi.org/10.1029/94JD00912). [Online]. Available: <https://agupubs.onlinelibrary.wiley.com/doi/10.1029/94JD00912> (visited on 04/12/2024).
- [92] R. O. Brick, L. L. Oh, and S. D. Schneider, “Effects of Lightning Attachment Phenomena on Aircraft Design,” en, Feb. 1970, p. 700 925. DOI: [10.4271/700925](https://doi.org/10.4271/700925). [Online]. Available: <https://www.sae.org/content/700925/> (visited on 04/05/2024).
- [93] A. Bouwers and P. Cath, “The maximum electrical field strength for several simple electrode configurations,” *Philips Technical Review*, vol. 6, no. 9, pp. 270–278, 1941.
- [94] J. H. Ferziger, M. Peric, and R. L. Street, *Computational Methods for Fluid Dynamics*, 4th ed. Cham, Swizerland: Springer Nature Swizerland, 2020, ISBN: 978-3-319-99691-2.
- [95] X. Gu, P. D. Ciampa, and B. Nagel, “An automated CFD analysis workflow in overall aircraft design applications,” *CEAS Aeronautical Journal*, vol. 9, no. 1, pp. 3–13, 2018. [Online]. Available: <https://link.springer.com/article/10.1007/s13272-017-0264-1>.
- [96] A. Matiz-Chicacausa, J. Escobar, D. Velasco, N. Rojas, and C. Sedano, “RANS Simulations of the High Lift Common Research Model with Open-Source Code SU2,” en, in *Numerical Simulation of the Aerodynamics of High-Lift Configurations*, O. D. López Mejia and J. A. Escobar Gomez, Eds., Cham: Springer International Publishing, 2018, pp. 93–111, ISBN: 978-3-319-62135-7. DOI: [10.1007/978-3-319-62136-4_6](https://doi.org/10.1007/978-3-319-62136-4_6). [Online]. Available: http://link.springer.com/10.1007/978-3-319-62136-4_6 (visited on 04/12/2024).
- [97] T. Fitzgibbon, C. Doolittle, P. Spalart, and Q. Wang, “The Application of Flow360 to the 7th Drag Prediction Workshop Cases,” Massachusetts, USA, Tech. Rep., Jun. 2023. [Online]. Available: <https://simcloud-public-1.s3.amazonaws.com/publications/DPW7/The+Application+of+Flow360+to+the+7th+Drag+Prediction+Workshop+Cases.pdf>.
- [98] E. N. Tinoco, “CFD Uncertainty and Validation for Commercial Aircraft Applications,” in *Computational Uncertainty in Military Vehicle Design*, Athens, Greece: NATO Research and Technology Organization, Dec. 2007, (20)1–(20)36.
- [99] W. J. Schroeder, K. Martin, W. E. Lorensen, L. S. Avila, K. W. Martin, and B. Lorensen, *The visualization toolkit: an object-oriented approach to 3D graphics ; /visualize data in 3D - medical, engineering or scientific ; build your own applications with C++, Tcl, Java or Python ; includes source code for VTK (supports UNIX, Windows and Mac)*, eng, 4. ed. Clifton Park, NY: Kitware, Inc, 2006, ISBN: 978-1-930934-19-1.
- [100] Message Passing Interface Forum, *MPI: A Message-Passing Interface Standard Version 4.0*. Jun. 2021. [Online]. Available: <https://www.mpi-forum.org/docs/mpi-4.0/mpi40-report.pdf>.

- [101] S. P. Austin, *D8 Geometry and Inviscid Flow Solution*, 2023.
- [102] M. Drela, “Development of the D8 Transport Configuration,” en, in *29th AIAA Applied Aerodynamics Conference*, Honolulu, Hawaii: American Institute of Aeronautics and Astronautics, Jun. 2011, ISBN: 978-1-62410-145-8. DOI: [10.2514/6.2011-3970](https://arc.aiaa.org/doi/10.2514/6.2011-3970). [Online]. Available: <https://arc.aiaa.org/doi/10.2514/6.2011-3970> (visited on 04/18/2024).
- [103] Y. Polyanskiy, “Multivariate Normal Distributions,” vol. Lecture 14, MIT OpenCourseWare, 2018. [Online]. Available: https://ocw.mit.edu/courses/6-436j-fundamentals-of-probability-fall-2018/resources/mit6_436jf18_lec14/.
- [104] H. Cheng and K. C. Gupta, “An Historical Note on Finite Rotations,” en, *Journal of Applied Mechanics*, vol. 56, no. 1, pp. 139–145, Mar. 1989, ISSN: 0021-8936, 1528-9036. DOI: [10.1115/1.3176034](https://asmedigitalcollection.asme.org/appliedmechanics/article/56/1/139/389565/An-Historical-Note-on-Finite-Rotations). [Online]. Available: <https://asmedigitalcollection.asme.org/appliedmechanics/article/56/1/139/389565/An-Historical-Note-on-Finite-Rotations> (visited on 04/13/2024).
- [105] T. A. Fitzgibbon, P. Spalart, Q. Wang, and J. Bungener, “An Analysis of Modeling Sensitivity Effects for High Lift Predictions using the Flow 360 CFD Solver,” en, in *AIAA AVIATION 2022 Forum*, Chicago, IL & Virtual: American Institute of Aeronautics and Astronautics, Jun. 2022, ISBN: 978-1-62410-635-4. DOI: [10.2514/6.2022-3745](https://arc.aiaa.org/doi/10.2514/6.2022-3745). [Online]. Available: <https://arc.aiaa.org/doi/10.2514/6.2022-3745> (visited on 04/13/2024).
- [106] C. D. Hansen and C. R. Johnson, *The visualization handbook*, eng. Amsterdam Boston: Elsevier-Butterworth Heinemann, 2005, ISBN: 978-0-12-387582-2.
- [107] T. D. Economon, F. Palacios, S. R. Copeland, T. W. Lukaczyk, and J. J. Alonso, “SU2: An Open-Source Suite for Multiphysics Simulation and Design,” en, *AIAA Journal*, vol. 54, no. 3, pp. 828–846, Mar. 2016, ISSN: 0001-1452, 1533-385X. DOI: [10.2514/1.J053813](https://arc.aiaa.org/doi/10.2514/1.J053813). [Online]. Available: <https://arc.aiaa.org/doi/10.2514/1.J053813> (visited on 04/13/2024).
- [108] S. Foundation, *Governing equations in SU2. Compressible Euler*, 2023. [Online]. Available: https://su2code.github.io/docs_v7/Theory/.
- [109] C. Geuzaine and J.-F. Remacle, “Gmsh: A three-dimensional finite element mesh generator with built-in pre- and post-processing facilities,” *International Journal for Numerical Methods in Engineering*, vol. 79, no. 11, 2009. DOI: [10.1002/nme.2579](https://doi.org/10.1002/nme.2579).
- [110] S. B. Pope, *Turbulent flows*. Cambridge ; New York: Cambridge University Press, 2000, ISBN: 978-0-521-59886-6.
- [111] *Simcenter StarCCM+*, 2022.
- [112] W. Oberle, “Monte Carlo Simulations: Number of Iterations and Accuracy,” US Army Research Laboratory, Aberdeen Proving Ground, MD, USA, Technical Note ARL-TN-0684, Jul. 2015. [Online]. Available: <https://apps.dtic.mil/sti/tr/pdf/ADA621501.pdf>.
- [113] F. L. Pitts and M. E. Thomas, “1981 direct strike lightning data,” NASA, Langley Research Center, Hampton, Virginia, Tech. Rep. 83273, 1982.

- [114] V. Mazur, B. D. Fisher, and J. C. Gerlach, “Lightning strikes to a NASA airplane penetrating thunderstorms at low altitudes,” in *24th aerospace sciences meeting*, Reno, Nevada, Jan. 1986.
- [115] V. Mazur, B. D. Fisher, and J. C. Gerlach, “Lightning strikes to an airplane in a thunderstorm,” *Journal of Aircraft*, vol. 21, no. 8, p. 611, Aug. 1984, ISSN: 0021-8669.
- [116] B. D. Fisher, “Lightning Swept-Stroke Attachment Patterns and Flight Conditions for Storm Hazards ’81,” en, NASA Langley Research Center, Hampton, Virginia, NASA Technical Memorandum NASA TM 86279, Sep. 1984.
- [117] L. D. Lee, G. B. Finelli, M. E. Thomas, and F. L. Pitts, “Statistical analysis of direct-strike lightning data (1980 to 1982),” NASA, Langley Research Center, Hampton, Virginia, Tech. Rep. TP-2252, 1984.
- [118] B. D. Fisher, G. L. Keyser, P. L. Deal, M. E. Thomas, and F. L. Pitts, “Storm Hazards ’79 F-106B Operations Summary,” en, NASA Langley Research Center, Hampton, Virginia, NASA Technical Memorandum NASA TM 81779, Mar. 1980.
- [119] T. F. Frost and K. P. Zaepfel, “Broadband electromagnetic sensors for aircraft lightning research,” in *Lightning technology: Proceedings of a technical symposium*, Apr. 1980.
- [120] V. Mazur and B. D. Fisher, “Cloud-to-ground strikes to the NASA F-106 airplane,” *Journal of Aircraft*, vol. 27, no. 5, pp. 466–468, May 1990.
- [121] J. L. Haseborg and H. Trinks, “Detection of projectiles by electric field measurements,” *IEEE Transactions on Aerospace and Electronic Systems*, vol. AES-16, no. 6, pp. 750–754, Nov. 1980. DOI: [10.1109/TAES.1980.308998](https://doi.org/10.1109/TAES.1980.308998).
- [122] M. E. Thomas, “Direct strike lightning measurement system,” in *Proceedings of the 1st flight test conference*, tex.venue: Las Vegas, Nevada, USA, AIAA, 1981, p. 2513.
- [123] K. P. Zaepfel, B. D. Fisher, and M. S. Ott, “Direct-strike lightning photographs, swept-flash attachment patterns, and flight conditions for storm hazards 1982,” NASA, Washington, DC, Tech. Rep. 86347, 1985.
- [124] B. D. Fisher, G. L. Keyser, and P. L. Deal, “Lightning attachment patterns and flight conditions for storm hazards ’80,” en, NASA Langley Research Center, Hampton, Virginia, NASA Technical Paper NASA TP 2087, Dec. 1982.
- [125] Autodesk, *Fusion360*, 2024. [Online]. Available: <https://www.autodesk.com/products/fusion-360/overview>.
- [126] N. A. Jenkins, *CAD Models*, 2024. [Online]. Available: <https://nathanaelj.github.io/Projects/Modelling#F-106B>.
- [127] General Dynamics/ Convair, “Technical manual: Structural repairs. USAF Series F-106A and F-106B aircraft,” US Air Force, Kelly Air Force Base, Texas, Tech. Rep. T.O. 1F-106A-3, 1961.
- [128] H. Schlichting, *Boundary-layer theory*, 7th ed. New York, USA: McGraw Hill, 1979.

- [129] *Manual on aeroplane upset prevention and recovery training*, eng, First edition. Montréal, Quebec, Canada: International Civil Aviation Organization, 2014, OCLC: 898128422, ISBN: 978-92-9249-563-3.
- [130] P. C. Steimle, D.-C. Karhoff, and W. Schröder, “Unsteady Transonic Flow over a Transport-Type Swept Wing,” en, *AIAA Journal*, vol. 50, no. 2, pp. 399–415, Feb. 2012, ISSN: 0001-1452, 1533-385X. DOI: [10.2514/1.J051187](https://doi.org/10.2514/1.J051187). [Online]. Available: <https://arc.aiaa.org/doi/10.2514/1.J051187> (visited on 04/18/2024).
- [131] S. Balzer, P. Castaigns, S. Delannoy, T. Lepagnot, X. Lesceu, D. Lopez-Fernandez, P. Sallier, and G. Savary, “A Focus on the Takeoff Rotation,” Airbus S.A.S., Tech. Rep., Jan. 2021. [Online]. Available: <https://safetyfirst.airbus.com/a-focus-on-the-takeoff-rotation/>.
- [132] S. N. V. Neigapula, S. P. Maddula, and V. B. Nukala, “A STUDY OF HIGH LIFT AERODYNAMIC DEVICES ON COMMERCIAL AIRCRAFTS,” *Aviation*, vol. 24, no. 3, pp. 123–136, Sep. 2020, ISSN: 1648-7788, 1822-4180. DOI: [10.3846/aviation.2020.12815](https://doi.org/10.3846/aviation.2020.12815). [Online]. Available: <https://journals.vilniustech.lt/index.php/Aviation/article/view/12815> (visited on 04/16/2024).
- [133] M. Ivanković, M. Vrdoljak, M. Andrić, and H. Kozmar, “Angle-of-Attack Estimation for General Aviation Aircraft,” en, *Aerospace*, vol. 10, no. 3, p. 315, Mar. 2023, ISSN: 2226-4310. DOI: [10.3390/aerospace10030315](https://doi.org/10.3390/aerospace10030315). [Online]. Available: <https://www.mdpi.com/2226-4310/10/3/315> (visited on 04/16/2024).
- [134] R. B. Anderson, “Lightning phenomena in the aerospace environment,” *Transactions of the South African Institute of Electrical Engineers*, vol. 66, no. 8, pp. 166–171, 1975.
- [135] F. A. Fisher and J. A. Plumer, *Lightning Protection of Aircraft*, 2nd ed. Massachusetts, USA: Lightning Technologies Inc, 1999.
- [136] Y. Goto and K. Narita, “LIGHTNING INTERACTION WITH AIRCRAFT AND WINTER LIGHTNING OF JAPAN,” en, *Journal of Atmospheric Electricity*, vol. 6, no. 1, pp. 27–34, 1986, ISSN: 0919-2050. DOI: [10.1541/jae.6.27](https://doi.org/10.1541/jae.6.27). [Online]. Available: https://www.jstage.jst.go.jp/article/jae/6/1/6_27/_article (visited on 04/15/2024).
- [137] J. A. Plumer, N. O. Rasch, and M. S. Glynn, “Recent data from the airlines lightning strike reporting project,” en, *Journal of Aircraft*, vol. 22, no. 5, pp. 429–433, May 1985, ISSN: 0021-8669, 1533-3868. DOI: [10.2514/3.45142](https://doi.org/10.2514/3.45142). [Online]. Available: <https://arc.aiaa.org/doi/10.2514/3.45142> (visited on 04/15/2024).
- [138] B. Yildirim, *Boeing 737-800*, CAD Model, Online, Oct. 2016. [Online]. Available: <https://grabcad.com/library/boeing-737-800-1>.
- [139] Boegger Industech Limited, *Micro Expanded Copper Mesh Aircraft Lightning Defence Application*, 2024. [Online]. Available: <https://www.copper-mesh.com/technology/micro-expanded-copper-mesh-lightning-defence-application.html>.

- [140] M. Kruger, *Blended Wing Body*, vsp3, GitHub, Feb. 2024. [Online]. Available: <https://github.com/danielenriquez59/vsp-gmr/tree/59b5eaee1947f67ffdae11f87637fa07d0d6a850/models/BWB>.
- [141] D. Scholtz, *ATR 72*, May 2020. [Online]. Available: <https://www.fzt.haw-hamburg.de/pers/Scholz/OpenVSP/ATR72.html>.
- [142] Flexcompute Inc., *Flow360 Documentation*, 2023. [Online]. Available: <https://docs.flexcompute.com/projects/flow360/en/latest/index.html>.
- [143] *SU2 Documentation*, 2024. [Online]. Available: https://su2code.github.io/docs_v7/Solver-Setup/.